TUM School of Computation, Information and Technology
Technische Universität München

Development of a Metal-Based Microfluidic MEMS Platform for Medical Applications

Claudia Patricia Durasiewicz, M. Sc.

Vollständiger Abdruck der von der TUM School of Computation, Information and Technology der Technischen Universität München zur Erlangung einer

Doktorin der Ingenieurwissenschaften (Dr.-Ing.)

genehmigten Dissertation.

Vorsitz:	Priv.-Doz. Dr.-Ing. habil. Markus Becherer
Prüfer*innen der Dissertation:	1. Prof. Dr. rer. nat. habil. Gabriele Schrag
	2. Prof. Dr. rer. nat. Christoph Kutter

Die Dissertation wurde am 09.06.2022 bei der Technischen Universität München eingereicht und durch die TUM School of Computation, Information and Technology am 16.11.2022 angenommen.

Abstract

Micropumps and microvalves are essential components of modern medical microfluidic systems for novel treatments of diseases, restoration of lost body functions, and increased patient comfort. To date, microfluidic device technology lacks safe, reliable, and efficient pumps and valves that readily fulfill biocompatibility, system hermeticity, and economic requirements. To address this demand, this work develops a versatile metal-based microfluidic platform of pumps and valves for medical applications.

The developments followed in this thesis include piezoelectric micropumps, passive safety valves, as well as normally closed (NC) and normally open (NO) piezoelectric microvalves. Firstly, microfluidic and technological challenges are identified to derive requirements for structural design, material properties, and characteristics of the metal microelectromechanical systems (MEMS) of this work. Furthermore, several technologies are investigated regarding their suitability for the developed platform, such as microstructuring of the rigid and foil-based metal components, their microjoining process, the MEMS driving mechanism, as well as sealing structures and elements. Design methods for metal microfluidic MEMS are established using experimental approaches as well as analytical and numerical modeling.

The evaluations of fabricated metal microfluidic MEMS confirm the achievement of desired functionalities. Moreover, successful advancement of micropump and microvalve key attributes through dedicated design, failure analysis, and manufacturing adaption is shown. The metal micropumps generate high water flow rates up to $(18 \pm 0.8)\,{}^{\mathrm{ml}}/_{\mathrm{min}}$ and pressures up to 130 kPa. Microvalve water leakage rates at a pressure of 20 kPa amount to $(0.03 \pm 0.02)\,{}^{\mu\mathrm{l}}/_{\mathrm{min}}$ for NC valves, $(7.5 \pm 1.4)\,{}^{\mu\mathrm{l}}/_{\mathrm{min}}$ for NO valves, and $(31.8 \pm 5)\,{}^{\mu\mathrm{l}}/_{\mathrm{min}}$ for passive safety valves. Material and performance stability are advanced in several development steps as well as miniaturization of the microfluidic MEMS. The established adaptable metal microfluidic platform enables vast opportunities to create numerous wearable and implantable medical devices.

Zusammenfassung

Mikropumpen und Mikroventile sind zentrale Elemente von modernen medizinischen Mikrofluidiksystemen, welche neuartige Therapien von Krankheiten, Wiederherstellung von Körperfunktionen oder Verbesserung des Patientenkomforts ermöglichen. Jedoch fehlt es an sicheren, zuverlässigen und effizienten Pumpen und Ventilen, die die Anforderungen an Biokompatibilität, Hermetizität und Kosteneffizienz erfüllen. Diese Arbeit widmet sich daher der Entwicklung einer anpassungsfähigen, metallbasierten Plattform von Pumpen und Ventilen für medizinische Anwendungen.

Die Entwicklungen, die in dieser Dissertation verfolgt werden, umfassen piezoelektische Mikropumpen, passive Sicherheitsventile, sowie stromlos geschlossene (NC) und stromlos offene (NO) piezoelektrische Mikroventile. Anfänglich werden mikrofluidische und technologische Herausforderungen identifiziert, um Anforderungen an das strukturelle Design, Materialeigenschaften und Charakteristiken der metallbasierten MEMS dieser Arbeit abzuleiten. Des Weiteren werden verschiedene Technologien bezüglich ihrer Eignung für die entwickelte Platform untersucht, wie die Mikrostrukturierung von Vollkörper-Bauteilen und dünnen Metallfolien, das Mikrofügen, der MEMS Antriebsmechanismus sowie die Dichtungsstrukturen und -elemente. Mittels experimenteller Untersuchungen sowie analytischer und numerischer Modellierung werden Designmethoden für metallbasierte mikrofluidische MEMS etabliert.

Mit den Untersuchungen der hergestellten metallbasierten mikrofluidischen MEMS Bauteile können die gewünschten Funktionalitäten nachgewiesen werden. Weiterhin wird die erfolgreiche Verbesserung der zentralen Leistungsparameter der Mikropumpen und Mikroventile durch gezieltes Design, Fehleranalyse sowie Anpassungen der Herstellung gezeigt. Die Metallmikropumpen erzielen hohe Flussraten bis zu $(18 \pm 0.8)\,{}^{\mathrm{ml}}/_{\mathrm{min}}$ und Drücke bis zu 130 kPa mit Wasser. Die erzielten Wasser-Leckraten der Mikroventile bei einem Druck von 20 kPa betragen $(0.03 \pm 0.02)\,{}^{\mu\mathrm{l}}/_{\mathrm{min}}$ für NC-Ventile, $(7.5 \pm 1.4)\,{}^{\mu\mathrm{l}}/_{\mathrm{min}}$ für NO-Ventile und $(31.8 \pm 5)\,{}^{\mu\mathrm{l}}/_{\mathrm{min}}$ für passive Sicherheitsventile. In mehreren Entwicklungsschritten werden Material- und Leistungsstabilität verbessert und Miniaturisierung von mikrofluidischen MEMS erzielt. Die etablierte, anpassbare, metallbasierte Mikrofluidik-Plattform ermöglicht mannigfaltige Gestaltungsmöglichkeiten von einer Vielzahl von tragbaren und implantierbaren Medizinprodukten.

Acknowledgments

I would like to express my gratitude to the people who have supported me in my doctoral thesis endeavor over several years of research, development, and scientific collaboration, without whom I could not have undertaken this journey.

First and foremost, I would like to thank Professor Dr. Gabriele Schrag for the supervision of my doctoral thesis project. I am thankful for her guidance throughout my doctoral project, during which she has supported my work and was an exceptional research advisor and partner. But her support extended far beyond the academic endeavor, and for her advice during demanding times and uncertainty, I am deeply grateful.

I also express my thanks to Professor Dr. Christoph Kutter, the second assessor of my doctoral thesis. Whenever I consulted him regarding my thesis work and questions, he was always able to give valuable advice. He was also a great source of motivation, which he could provide in an instant with kind words of support.

It has been a rewarding and fulfilling experience to have worked within the microdosing systems department of Fraunhofer EMFT, and I am very thankful for the research opportunity given by Dr. Martin Richter.

My deepest gratitude goes to Christian Wald, who has given me his unconditional support and advice. I thank him for all the technical discussions as well as the many hours of scientific and philosophical dialog. With his support, I was able to gain the strength, personal growth, and endurance for this thesis work.

I would also like to thank my mentor and research partner Dr. Sebastian Kibler. I have always valued his advice regarding my thesis work and our good collaboration, and am thankful for him being a sparring partner to me for microvalve developments.

Throughout my years at Fraunhofer EMFT, I was lucky to be part of an incredibly supportive group of doctoral candidates - I am thankful for the unforgettable times with Dr. Agnes Bußmann, Dr. Thomas Thalhofer, and Dr. Lorenz Grünerbel. We have learned so much together and from each other, and this exciting time within this group will always be a cherished memory to me.

It is not possible to thank everyone from Fraunhofer EMFT's microdosing systems group for all their individual support and contributions, but I am grateful for all the

help, shared ideas, and all experience I have gained in the microfluidic laboratory and in technical discussions. It was a pleasure working within this group.

Many thanks go to Sophia Güntner, Kiran Ravada, Nivedha Surendran, Philipp Maier, Johannes Schwarz, and Akshay Wankhade, for supporting my work with their Bachelor and Master theses. Furthermore, I would like to thank Sophie Hoffmann, Thalia Hoffmann, and Jan Lützelberger for their support during their internships. Working with them was an invaluable source of motivation for me, as I have found that being a mentor to young, bright people like them and the mutual appreciation during our collaborative work were the most rewarding part of my day. It was fantastic to see their experience and confidence grow immensely over the course of only several months, and exciting to discover their individual, unique talents. It was a pleasure to having worked with them, I am proud of having been a part of the professional journey of each of them, and thank them for all the knowledge gained together.

A special thanks goes to my industrial research partners who gave me the chance to dedicate my scientific efforts towards the development of microfluidic devices for an implantable hydraulic system. I am thankful for the technical tasks that I was given, and as demanding as the project work was, it was always an enjoyable, appreciative collaboration with a valuable exchange of ideas and expertise. I am thankful for all the knowledge I have gained throughout the years from the many experienced, creative people involved in this development project. I wish them great success for their future developments - I'm sure it'll be grand.

Lastly, I would like to thank the many people who supported me during the writing period of this dissertation. I am deeply grateful for the encouragement, support, and hours of proofreading efforts from Erik Rittmüller. I am also thankful for the help of Doris Zhou, Patrick Durasiewicz, Christian Wald, Dr. Sebastian Kibler, Dr. Agnes Bußmann, and Sven Lilge for proofreading of this work.

Contents

Core Publications

This publication-based thesis presents the comprehensive research results and the methodology of the conducted development of a metal microfluidic MEMS platform. The detailed results are published in the following scientific journal and conference articles:

1. A. B. Bußmann* and C. P. Durasiewicz*, S. H. A. Kibler, and C. K. Wald, "Piezoelectric titanium based microfluidic pump and valves for implantable medical applications", Sensors and Actuators A: Physical, p. 112649, 2021. [1]
   *A. B. Bußmann and C. P. Durasiewicz contributed equally.

2. C. P. Durasiewicz, S. T. Güntner, and S. H. A. Kibler, "Piezoceramic mounting process and adapted pretension for improved microvalve functionality and reliability", *Proceedings of MikroSystemTechnik Kongress 2021, Stuttgart-Ludwigsburg, 08.-10. November 2021,* ISBN 978-3-8007-5656-8, VDE e.V. (Hrsg.) [2]

3. C. P. Durasiewicz, W. Hölzl, and G. Schrag, "'Safety Valve': A metal-based, self-securing switchable microvalve for medical applications", *Proceedings of MikroSystemTechnik Kongress 2021, Stuttgart-Ludwigsburg, 08.-10. November 2021,* ISBN 978-3-8007-5656-8, VDE e.V. (Hrsg.) [3]

4. C. P. Durasiewicz, S. T. Güntner, P. K. Maier, W. Hölzl, and G. Schrag, "Piezoelectric Normally Open Microvalve with Multiple Valve Seat Trenches for Medical Applications", Applied Sciences, vol. 2021, no. 11, p. 9252. [4]

In the following, these articles are referred to as **Core Publications [1], [2], [3],** and **[4]**, respectively.

List of Symbols

E	Young's modulus
h_{IG}	Initial gap height
h_{VS}	Valve seat height
R_z	Surface roughness as the average distance between the highest peak and lowest valley in each sampling length, as per ASME Y14.36M - 1996 standard

List of Acronyms

AISI	American Iron and Steel Institute, here: prefix to standardized steel alloy numbering
AM	Additive Manufacturing
ASME	The American Society of Mechanical Engineers
CAD	Computer-Aided Design
CVD	Chemical Vapor Deposition
DoE	Design of Experiments
EPDM	Ethylene Propylene Diene Monomer
HAZ	Heat Affected Zone
ISO	International Organization for Standardization
FEM	Finite-Element-Method
FKM	Fluorocarbon
FSI	Fluid-Structure-Interaction
MEMS	Microelectromechanical Systems
MRI	Magnetic Resonance Imaging
NC	Normally Closed
NO	Normally Open
PBF	Powder Bed Fusion
PCM	Photochemical Machining
PZT	Lead Zirconate Titanate

Glossary

Backflow	Fluid flow against flow direction of the device/system, induced by external disturbances
Backpressure	Fluid pressure present at the micropump outlet
Biocompatibility	"ability of the device to perform its intended function, with the desired degree of incorporation in the host, without eliciting any undesirable local or systemic effects in that host." [5]
Blocking Pressure	Pressure equivalent of the maximum generated force of the piezoelectric bending actuator
Bubble Tolerance	Pressure capability of a micropump to reliably displace an air bubble out of the pump chamber
Compression Ratio	Ratio of displaced volume of a pump to dead volume in the pump chamber
Dissimilar Metal Weld	Joining of two or more different metals via welding
Fiber Laser	Laser with an optical fiber as the active gain medium
Flow Logic	The use of a fluid to perform logic operations based on pneumatics or hydraulics, here: opening and closing of a fluid path under certain pressure conditions in the system

Freeflow	Fluid flow in flow direction of the device/system, induced by external disturbances
Hermetic Sealing	Characteristic of a joining seam that prevents fluids or gases of passage out or into a cavity of an object
Initial Gap	Default gap between the valve plate and the valve seat in an assembled metal micropump, as a result of deformations induced by manufacturing processes
Keyhole Welding	Deep penetration welding technique, gaining its name from the keyhole shaped cavity formed by the vaporized metal
Lap Joint	Weld configuration where joining partners are stacked, e.g. foils on top of a rigid substrate
Medical Imaging	Imaging techniques for clinical use, such as magnetic resonance imaging and radiography
Nd:YAG Laser	Solid state laser with a neodymium-doped yttrium aluminum garnet crystal as the active gain medium
Pretension	Initial deflection of the piezoelectric bending actuator as a result of piezoceramic bonding under voltage load
Squeeze Film Damping	Viscous effects of thin fluid layers between moving (micro-)structures causing damping of the movement
Stroke	Transversal movement performed by an active or a passive actuator diaphragm
Welding Joint Type	Configuration of joining partners and their position to each other, e.g. stacked for lap joint, side by side for butt joint, etc.

1 Introduction

The demand for medical technology innovation increases constantly as modern medicine progresses towards personalized treatment, novel therapies of so far untreatable or chronic diseases, and improved quality of life for aging societies. Using microfluidic structures and micromachines, modern medical devices perform drug delivery, restore lost body functions, or aid healing processes of the human body to promote patient well-being. Current developments of microfluidic systems for medical applications, like wearables or implants, call for the design of effective and reliable devices.

Microelectromechanical systems (MEMS) originate from silicon technology [6], which is known for precise manufacturing of microstructures and cost-efficient mass production [7]. However, cost-efficiency is difficult to attain in small and medium lot size production. Moreover, specific requirements arise to medical use [8]. For implants, the devices must be biocompatible and suited for medical imaging, such as magnetic resonance imaging (MRI). Most importantly, system hermeticity is an indispensable prerequisite to eliminate any risk to the patient's life arising from electrical contact or fluidic leakage. Additional application-specific considerations can include dosing precision, resilience against challenging environmental conditions, energy consumption, lifetime, and ability to system integration.

Metal-based MEMS readily address many of these requirements, with one of their major advantages being the potential of hermetically sealed system integration by welding. To this day, there are examples of studies and developments of microfluidic MEMS partially comprising metal [9–17], without the possibility to join their components with hermetic seals. To fully exploit the advantage of hermetic system integration into medical devices, there is a need for a versatile, high performance metal microfluidic MEMS platform comprising a multitude of devices like micropumps and microvalves with distinct functionalities. While the use of metal poses additional technological challenges to the device design, a universally applicable metal MEMS platform for medical microfluidic systems holds the potential for creating effective innovations for patient care.

This thesis addresses the need for reliable, safe, and potent medical microfluidic MEMS, capable of opposing the challenges unique to fluidic applications on a microscale. The envisaged use cases are hydraulic implants, requiring high flow and pressure build-up of a micropump and leak-tight microvalves, as well as a wearable drug delivery system, demanding specific safety functionalities. This work describes the development, feasibility, optimization, and potentials of creating a metal microfluidic MEMS platform, while - at the same time - considering system and application requirements for medical devices.

1.1 Challenges in Medical Microfluidic Applications

Over the last decades, many researchers devoted their development work on micropumps and microvalves, covered by a large number of reviews [18–25]. Some works discuss the suitability of those microfluidic devices in biomedical applications [26, 27] and, more specifically, for drug delivery [28–31]. Most of these reviews categorize the micropumps and microvalves by their working principles. While several representations of each operating principle exist, this work focuses on specific types of pumps and valves described in the following.

A well known type of micropump is the mechanical piezoelectric diaphragm pump with passive check valves that rectify the volumetric flow generated by a transversal reciprocating movement of the actuated diaphragm. In contrast, an active microvalve is used to open and close a fluid path when desired. There are two main types of microvalves, defined by their default state of the non-actuated valve: a normally closed (NC) valve prevents any flow in non-actuated state, whereas a normally open (NO) microvalve allows fluid flow when a pressure gradient is present, and only closes when actuated. Many microvalves are diaphragm valves, actively closing a microfluidic path underneath their actuator. Another type is the plunger microvalve, resembling the macroscopic working principle of a suspended plunger on a circular opening, and the valve allows flow once an actuator displaces the plunger transversally.

These three types of active microfluidic devices are likewise present in studies and developments of microfluidic MEMS comprising metal parts [9–17]. Though, in the context of medical applications, these devices do not satisfy certain obligatory requirements for effective wearable or implantable systems. The devices either fail to exhibit hermetic sealing [10, 11, 13–15], are dependent on external actuation sources [9, 17], or show

insufficient performance in terms of pump flow rate [16] or valve switching time [12]. To efficiently and effectively develop microfluidic MEMS suitable for miniaturized medical systems, it is essential to define a set of requirements, identify the challenges intrinsic to microfluidics, and find solutions that are manufacturable in metal.

In a review of microdosing systems and micropumps for drug delivery, *Bußmann, Grünerbel, Durasiewicz et al.* discuss challenges in microfluidics with a view to medical applications alongside respective micropump design solutions [32]. Figure 1 depicts those challenges which are also applicable to the implantable and wearable applications envisaged in this thesis. The first challenges refer to system size and power restrictions, as these may impede microfluidic key attributes. A key attribute restricted by size limitations is the generated flow rate of a micropump, which is difficult to simultaneously obtain with a high pressure build-up to properly pump against a backpressure of the delivery target. For drug delivery, the required microfluidic key attributes also include the dosing stability, which is crucial for the patient's welfare. Another set of challenges involve safety requirements of medical devices. The risk of uncontrolled drug flow may arise from pressure gradients in the microfluidic system. These may be induced gravimetrically, by tissue pressure, or external forces. These pressure gradients can cause freeflow through the passive check valves of a micropump, possibly leading to uncontrolled drug release; can induce backflow of hydraulic or tissue fluids, if the check valves are insufficiently closed; or can lead to any kind of unwanted leakage through an active valve. The small dimensions of a microfluidic device pose additional challenges, as surface-scaled disturbances like bubbles or capillary forces lead to inefficiency of a micropump due to fluidic damping. If the transported medium is a fluid containing proteins or other large molecules, like drugs, the interaction of the microfluidic device with the medium can cause damage to both, the device as well as the transported drug. Other safety requirements relate to failure detection or electrical safety, indispensable for devices in direct human contact. Finally, system-specific requirements cover biocompatibility, hermetic sealing, size and weight, as well as cost, and, for implantable applications, suitability for medical imaging. It is important to overcome all these challenges to develop a safe and effective medical device. This thesis focuses on developments and solutions to the challenges directly related to the structural design of the metal MEMS devices. Therefore, the developments of my work address pressure and flow generation of micropumps, tightness against freeflow and backflow, and provides solutions to medical imaging, biocompatibility, hermetic sealing, and size requirements (see Figure 1).

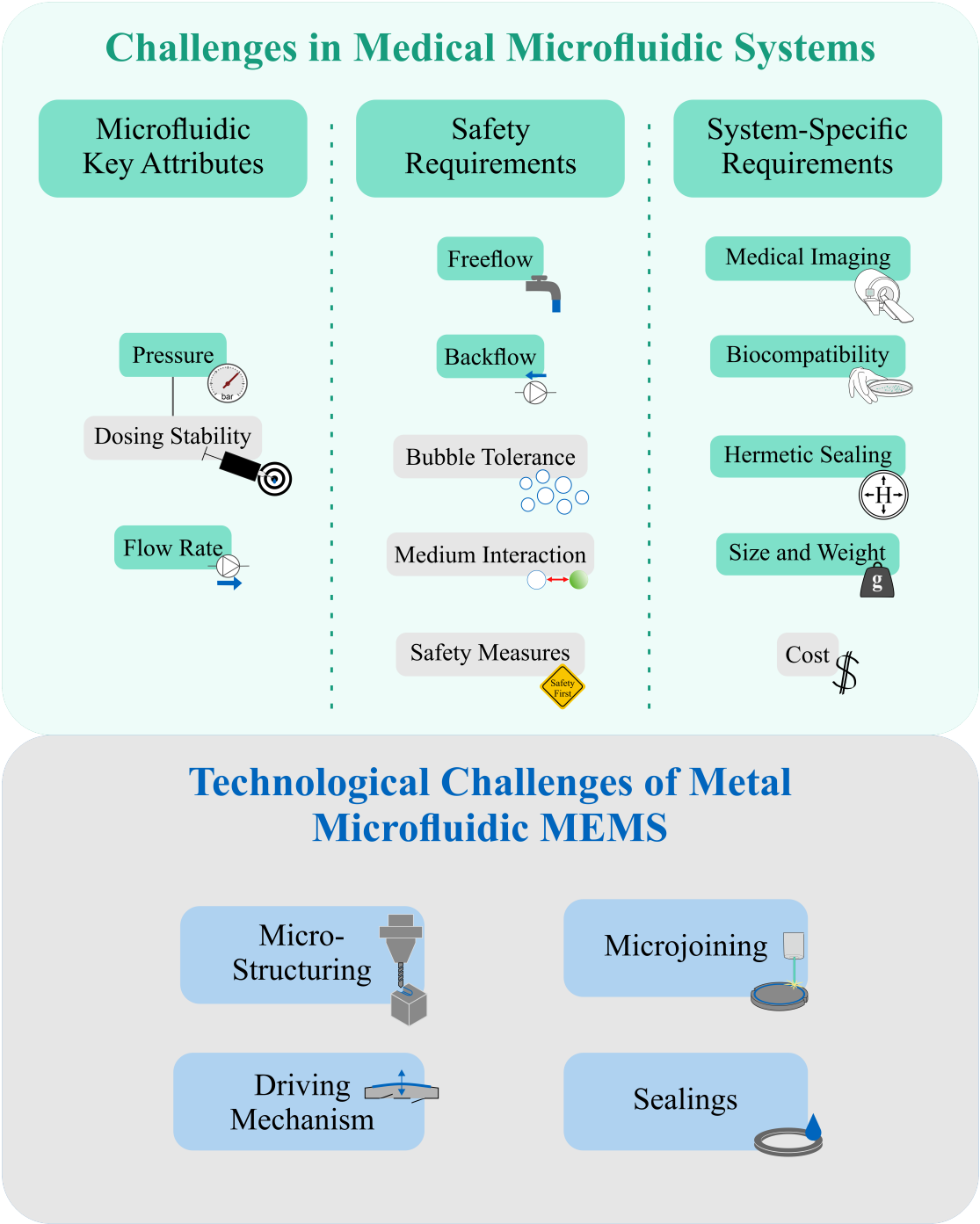

Figure 1: Overview of challenges in microfluidic systems for medical applications, adapted from *Bußmann, Grünerbel, Durasiewicz et al.* [32], as well as technological challenges of metal-based microfluidic MEMS. Challenges addressed with the developments within this thesis are highlighted in green and blue.

There are several research efforts preceding this work, which propose solutions to these microfluidic challenges. *Richter et al.* [33] formulate a patented working principle of a passive microvalve, the so-called 'safety valve', that provides flow logic to a microfluidic system and prevents obstructive freeflow. In another patent, the pretension technique for manufacturing a piezoelectric bending actuator from *Herz et al.* [34] allows to establish a large compression ratio [35] of a micropump, ensuring robustness against a disturbance in form of an air bubble inside the pump chamber. *Wald et al.* [36] present such a pretensed piezoelectric micro diaphragm pump based on stainless steel. Furthermore, a patent from *Wald et al.* [37] describes the structure and working principle of a piezoelectric NC microvalve. Based on the works of *Richter et al.* [33], *Herz et al.* [34], and *Wald et al.* [37] as well as the metal-based pump [36], this thesis develops a metal microfluidic MEMS platform.

The manufacturing process of the stainless steel micropump [36] lays the technological basis for fabrication of metal microfluidic MEMS within this proposed platform. Figure 2 depicts the components of the metal micropump as well as the process steps employed for assembly.

The metal-based micropump comprises a rigid metal base (I), thin metal foils as passive check valves (II, III) and the actuator foil (IV), as well as a lead zirconate titanate (PZT) piezoceramic (V). The manufacturing process involves various techniques to assemble the micropump with a final size of 20 mm in diameter and 1.5 mm in height. To form and structure the metal components, they are micromachined from bulk or sheet rolled with subsequent photochemical machining. A laser welding process joins the metal foil stack to the base with hermetically tight weld seams. Finally, a sophisticated gluing process of the PZT to the metal actuator foil establishes a pretensed actuator, resulting in a pump chamber with a high compression ratio. These processes are provably adequate to create a steel micropump with high performance [36]. However, for the adaptive design of specialized microfluidic MEMS within a versatile platform, the technologies must be deeply understood to purposefully achieve the desired properties and performance capabilities.

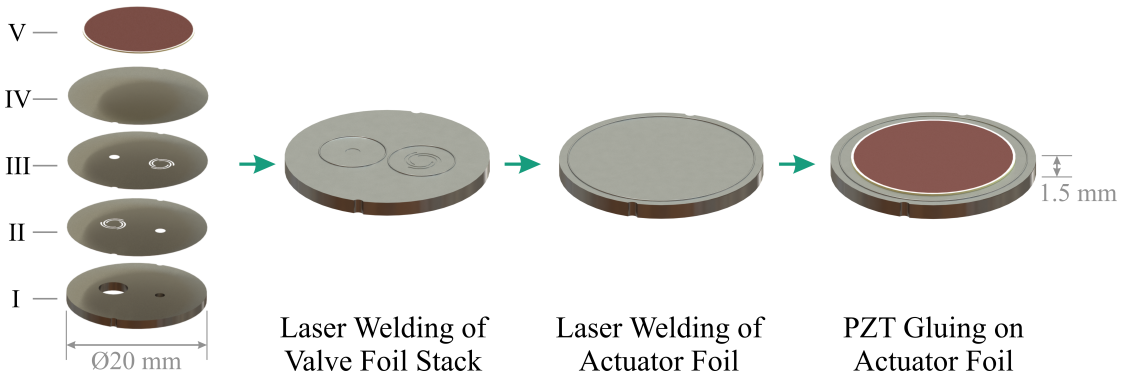

Figure 2: Metal micropump manufacturing process employed in this thesis, based on *Wald et al.* [36]. The pump consists of a microstructured metal base (I) and photochemically machined foils serving as the outlet valve (II), the inlet valve (III), and the actuator foil (IV). A laser welding process joins the foils to the base with hermetically tight weld seams. The piezoceramic (V) is glued to the actuator foil using the pretension technique from *Herz et al.* [34], creating a pump chamber with a high compression ratio.

Alongside the above mentioned microfluidic challenges, Figure 1 includes an overview of the technological challenges of metal microfluidic MEMS for medical devices.

Appropriate procedures for microstructuring of metal components from bulk and foil are necessary to accomplish high precision, crucial for device miniaturization, and can be exploited to create practical features with favorable microfluidic effects. Due to thermal stresses induced in the thin metal foils, the laser welding process adds high complexity to the design and fabrication of the metal MEMS: material warpage impedes tightness of passive valve structures and induces additional stress to actuator foils. A piezoelectric driving mechanism of an active metal MEMS or a pressure-induced driving mechanism of a passive metal MEMS needs diligent (electro-)mechanical design to accomplish the desired actuator characteristics. Moreover, apt valve sealings are indispensable for designing leak tight microvalves, as the cold-rolled metal foils exhibit higher surface roughness compared to standard MEMS materials such as silicon. Additionally, thorough understanding of leakage flows and the impact of surface roughness on leakage paths is essential for microvalve development.

In addition to the microfluidic challenges in medical applications, the developments of this thesis focus on these technological challenges arising in the design of metal microfluidic MEMS.

1.2 Research Goal and Thesis Structure

The research goal of this thesis is to develop a versatile technology platform of metal microfluidic MEMS for medical applications. The work aims towards providing a broad repertoire of active and passive devices for either flow generation or fluid path control. To ensure high functionality when combined to form a microfluidic system, their respective design shall be balanced with a view to interdependent characteristics such as minimized fluidic resistance and low leakage rates. The use of the same manufacturing processes shall simplify production and facilitate system integration. To this end, each device of the developed platform shall be of similar form factor and structural design.

Figure 3 visualizes the adaptive metal MEMS platform envisaged in this thesis. It emphasizes the similarity of the devices, which all include a metal base (I), a metal diaphragm serving as the actuator (II) joined to the base with an hermetic weld seam (III), and a driving mechanism (IV), which is either actively controlled with a piezoceramic or passively induced by a pressure gradient. Each of these adaptive MEMS devices attains its distinct functionality by purposeful design of its function area (V) beneath the actuator, thereby becoming either a micropump, a passive or an active microvalve of either NC or NO type.

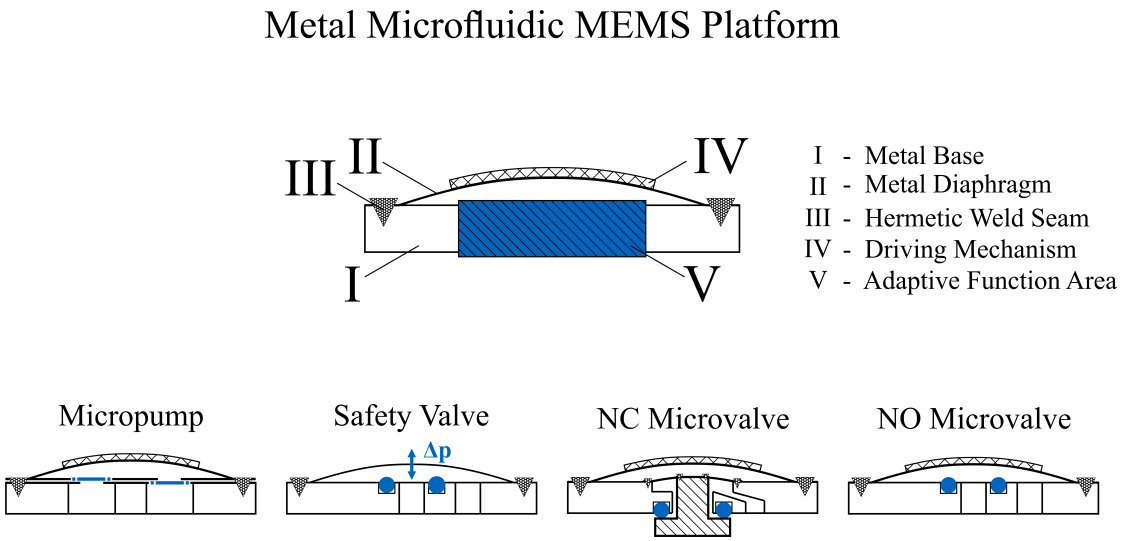

Figure 3: Visualisation of the adaptable metal microfluidic MEMS platform for medical applications including the four developed devices of this work. Each device possesses distinct functionalities, while using the advantage of similarity in structural design.

The developments of this metal microfluidic MEMS platform advance specific properties of the devices, essential for their functionality in the envisioned medical applications. Manufacturability, safety, and reliability throughout device lifetime are obligatory for all of the developed microfluidic MEMS, as these are fundamental requirements for medical devices [38]. The development of novel titanium-based MEMS fulfills the need for devices suitable for implants, while stainless steel MEMS offer less cost-intensive solutions for applications outside the body. In both use cases, fluidic key attributes like generated pump flow rate or valve tightness ensure correct functionality of the medical device, and are ultimately responsible for improving the patient's well-being. In contrast, characteristics like micropump leakage or the maximum flow rate through a microvalve in open state may be considered as secondary attributes: Depending on the application, these may only affect the efficiency of the medical system. Hence, these secondary attributes may be ranked lower in priority, provided that careful evaluations of potential impacts on the medical device functionality exclude any risks for the patient. Lastly, developments may aim for miniaturization or lowering cost of the device, given that these do not impair aforementioned properties. Figure 4 presents these development goals in an order of priority, from obligatory to desirable.

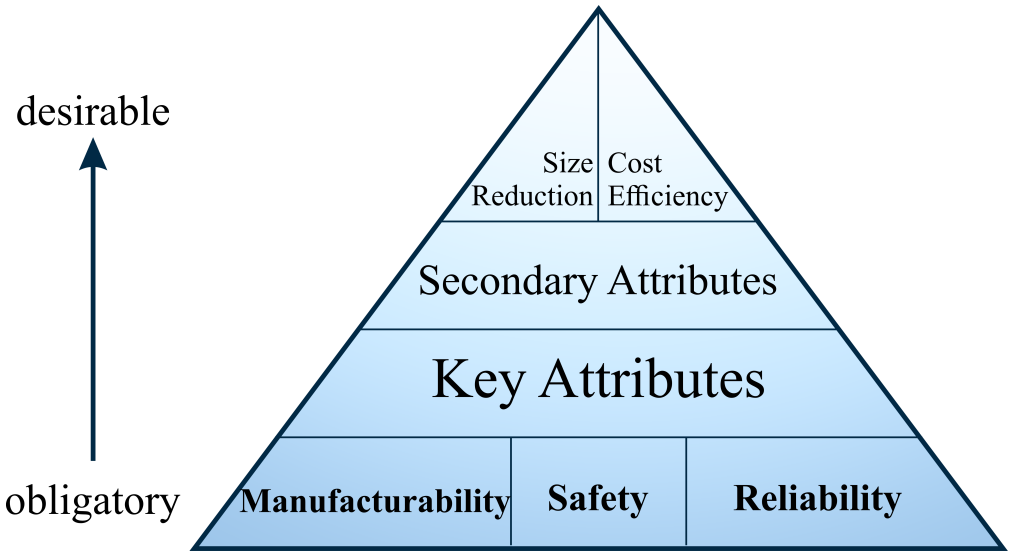

Figure 4: Fundamental properties of devices for medical applications. My thesis optimizes these properties, while prioritizing obligatory attributes over desirable ones.

This thesis addresses the obligatory development goals of manufacturability, safety, and reliability in Chapter 2. Section 2.1 covers the work on the technological challenges of metal microfluidic MEMS in detail: It presents the efforts towards adaptable design knowledge for the versatile platform gained by literature research, numerical simulations, analytical analyses, and experimental investigations. The developments of the micropump, the passive safety valve, as well as the active NC and NO microvalves are subject of Chapter 3. Moreover, this chapter provides insights into the definitions of respective key attributes and individual development steps of each microfluidic MEMS of this thesis. Chapter 4 contains summaries of the Core Publications [1–4] that present the developments and detailed results in international, peer-reviewed journals or conference proceedings. The thesis is concluded with a summary of the acquired research findings as well as an outlook on further developments of the metal microfluidic MEMS platform in Chapter 5.

2 Methods

Manufacturability, reliability, and safety are fundamental for dependable medical devices. In the following, the manufacturability section focuses on the challenges in metal MEMS technology in detail. Microstructuring, microjoining, the driving mechanism, and sealings are essential parts of this thesis to develop the metal microfluidic MEMS platform, but encompass several technological challenges. The safety and reliability sections describe these requirements in medical devices in general and how they relate to the research objectives of this advance development. My work addresses these challenges with literature research, dedicated numerical simulations, targeted design of experiments (DoE) as well as analytical analyses.

2.1 Manufacturability and Technological Challenges

When designing a microfluidic device, it is crucial to consider manufacturing constraints from the beginning. Careful selection of the steel or titanium alloy is necessary, as the metals differ in machinability [39–42], weldability [43, 44], as well as biocompatibility and medical imaging suitability [45–49]. This thesis builds broad knowledge of the processes for creating active and passive metal microfluidic MEMS. These shall ideally be based on standard procedures, have low manufacturing cost, and be suited for both small and medium development lots as well as future mass production.

2.1.1 Microstructuring

The structural design of a metal MEMS device begins with shaping its metal base and other structured components like metal foils. The microstructures of rigid or foil components fulfill distinct purposes, therefore, they define its function as a pump or valve, and fundamentally determine its performance. For purposeful design of microfluidic devices, utilized processes must guarantee high manufacturing precision to comply with structural design complexity on a micrometer scale. Additionally, high surface quality is necessary as surface-scaled disturbances immensely affect microfluidic systems due to their high surface-to-volume aspect ratio. Moreover, the manufacturing processes must

be compatible with subsequent manufacturing steps like microjoining (see Section 2.1.2), which is indispensable for hermetic sealing. Furthermore, it must avoid manufacturing defects like residual stresses in the materials. The structures in the developed metal microfluidic MEMS have dimensions of $100 - 500\,\mu$m in rigid components, or are implemented in foils of $25 - 150\,\mu$m thickness, and must be readily manufacturable in short development cycles.

To achieve microstructures in rigid components, there are many processes to form materials from bulk or by additive procedures. Micromilling is a common process to realize 3D sculptured surfaces and fine shapes with high aspect ratios in bulk material [50, 51]. It holds major advantages compared to electro discharge machining, laser beam machining, or electrochemical machining: While all of these processes are capable of creating structures with micrometer precision, they have slow processing times, require custom-made tools that resemble the desired shape, or are destructive to the tools used [52]. High cost of tools is a major disadvantage for fabrication of small research lots in short development cycles. Hence, micromilling is the method of choice for structuring of rigid metal parts in this thesis.

Various research works report on the suitability of this mechanical machining technique to create precise microstructures in metals [53–56]. It combines many advantages, as it is capable of high precision, high surface quality, low tool wear compared to tool-destructive methods, and fast processing times [54]. The designs of the fabricated structures are more restricted with micromilling compared to additive manufacturing (AM) techniques. For more basic geometries like holes and rectangular channels, micromilling benefits from the simplicity and versatility of milling tools. Hence, this fabrication method is especially advantageous to fabricate small to medium lot sizes. In this thesis, metal MEMS bases as well as the valve plunger of the NC valve (see Core Publication [1]) are micromilled. The material choice predominantly depends on economical and compatibility considerations (see Section 2.2). For the research samples in the scope of Core Publication [4], the steel alloy AISI 303 is used, as it offers high machinability [39, 40]. Figure 5 shows micromilled concentric trenches, creating a valve seat structure (see Section 2.1.4). The evaluated surface roughness amounts to a value of $R_z = 0.4\,\mu$m, advantageous for both, the microjoining process (see Section 2.1.2) as well as the sealing abilities of the microvalve (see Section 2.1.4).

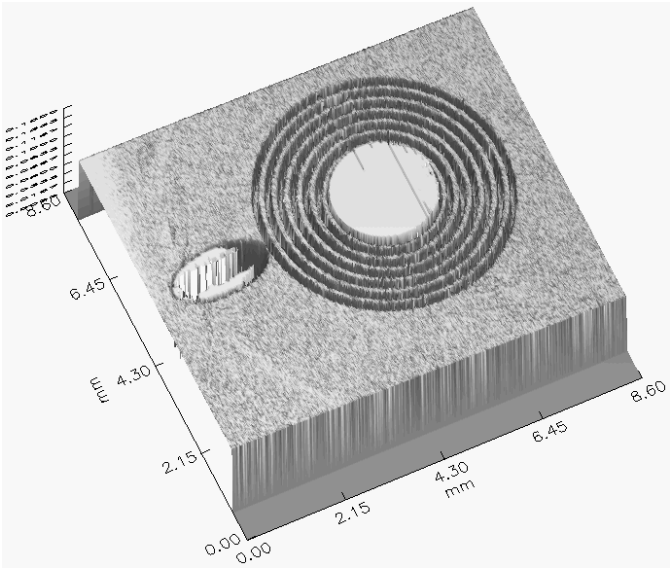

Figure 5: White light interferometry data showing the topology of a steel base of an NO valve with micromilled trenches, serving as a valve seat (see Core Publication [4]). The trenches are both $100\,\mu$m in width and in depth, with a precision of $\pm 3\,\mu$m. Surface roughness amounts to a value of $R_z = 0.4\,\mu$m.

Despite the suitability of micromilling for creating precise microstructures, the following reflects on an alternative manufacturing method: Laser-based additive manufacturing does not require custom-made tools and offers broad design freedom for creating metal parts. In the past years, many studies reported on advances in the field of AM processes for metals as a versatile and innovative tool [57–63]. Of those, powder bed fusion (PBF) is the most commonly used process that allows rapid prototyping and fabrication of intricate geometries. This selective laser melting technique transforms metal powders to complex rigid parts, including undercuts and interlacing structures. However, the process itself is still relatively expensive [61], and surface quality of PBF products depends on the powder particle size [62]. Powder particle sizes of $15 - 45\,\mu$m are common due to their advantages in processability. However, without additional costly post-processing, PBF methods result in coarse surfaces [64], with roughness in the same order of magnitude as the respective powder particle size. High surface roughness is problematic in the final microfluidic application, as it leads to frictional losses and bubbles may adhere easily. Furthermore, poor surface quality is detrimental to the subsequent welding process. The surface roughness causes insufficient contact of the mating surfaces, ultimately leading to weld seam failures (see Section 2.1.2). Some of the research work in the field of AM of metals revolves around improving product qualities for subsequent processing [65] or

investigate residual deformations in the product [66]. Research advances in this field could open new possibilities for microfluidic metal structures in the future. In this work, AM methods such as PBF are not pursued for fabrication of the metal microfluidic MEMS.

Within the metal microfluidic MEMS platform, thin metal foils execute different functions as either part of the driving mechanism (see Section 2.1.3) or, in case of the passive check valves in a micropump, as part of the function area. For adaptive and flexible design in the envisaged application range, foil structuring processes shall be capable of creating tension-free structures within foils of $25 - 150\,\mu$m thickness.

Cold-rolled metal foils are commercially available in a broad selection of thicknesses down to $5\,\mu$m. Strain-hardened sheet materials exhibit slightly altered, anisotropic material properties such as Young's modulus and texture strength compared to bulk material: The material deformation affects the grain structure of the metal [67–69], as well as the surface topology, as furrows result from the sheet forming process. Material defects after cold-rolling may occur in the material, if the sheets are coiled for transport, resulting in stresses and curvature in the final products (see Figure 6). As these defects and residual stresses may appear in the metal foils prior to structuring, it is crucial to choose subsequent processes with little to no additional stress impacts on the materials. Subsequent post-processing like annealing can help to prevent these effects, but require high effort to achieve favorable recrystallization [70, 71], and the advantageous material properties of the strain-hardened metal foils are lost. Hence, foil components of this work are not annealed.

Commonly used processes for surface structuring of bulk materials as well as cuts through thin metal foils are photochemical machining, laser cutting, or laser micromachining [72–78]. While laser cutting and laser micromachining methods are capable of forming precise structures on a micrometer scale, significant heat impact induces thermal stresses within the thin sheet materials. To avoid such material defects, femtosecond pulse laser processes must use low pulse energy [76], adversely resulting in low processing speeds. Therefore, laser micromachining methods are relatively expensive or affect the material with heat-induced stresses, and are consequently not pursued further.

Photochemical machining (PCM), also referred to as photochemical etching, is a precise fabrication method for surface structuring and cuts of thin metal foils below 2 mm of thickness. PCM combines photolithography and wet chemical etching, and is a well

established technique in industry and research [79–83]. It allows broad design freedom of the etched cross-sectional profiles and the finished products are burr- and tension-free. *Allen* provides a comprehensive overview of this structuring technique for metals [84]. In this work, *Allen* describes the effect of unwanted machining of the substrate material under the photoresist: due to the isotropic nature of the etching process, the etchant creates undercuts in the metal underneath the photo resist. This effect must be avoided as it poses limitations to the minimum feature size manufacturable by PCM. *Agrawal and Kamble* report on the optimization of PCM parameters like etchant temperature, concentration, and etching time to successfully avoid undercut effects, and present PCM microfluidic channels in stainless steel [85]. PCM structured metal foils are commonly available from manufacturers, who claim aperture and feature accuracies of less than $\pm 10\,\%$ of metal sheet thickness, with minimal sheet thickness of $5\,\mu$m [86]. This fabrication method allows short development cycles and is suitable for small lots as well as mass production. Hence, metal foil components of this work are produced via PCM. Topology measurements show surface roughness values of $R_{z,steel} = (7.5 \pm 1.3)\,\mu$m for AISI 304 steel foils and $R_{z,titanium} = (5.5 \pm 1.0)\,\mu$m for titanium grade 5 foils ($n = 10$, respectively). Section 2.1.2 discusses the suitability of these surface qualities for the microjoining process, and Section 2.1.4 describes the effect of surface roughness on leakage flows. Figure 6 depicts the $50\,\mu$m thick titanium micropump check valve foils of Core Publication [1]. The ortho-planar spring valve structure comprises a valve plate suspended by three spring arms that are formed by photochemically machined slits. Both, spring arm width and slit width, amount to $200\,\mu$m.

The titanium micropump valve foils show discernible curvature due to metal sheet coiling prior to structuring. Coiling or other negligent handling must be avoided, as non-planarity of the foils cause insufficient contact of the valve plates to their valve seat, ultimately leading to increased leakage. The gap between the valve plate and its seat remaining after micropump assembly, the so-called 'initial gap', is additionally influenced by the microjoining process. Hence, Section 2.1.2 discusses the initial gap further.

Figure 6: Photograph of cold-rolled, photochemically machined titanium foils with passive check valve structures. As a result of residual stresses caused by coiling of the sheet material prior to PCM, the $50\,\mu$m thick foils exhibit a noticeable curvature.

For the manufacturing of micropumps and microvalves, this work chooses micromilling of metal bulk material and PCM of foils, as these processes are capable of high precision and do not induce additional material stresses. They are readily available for prototyping of new research samples and compatible with subsequent manufacturing steps, such as microjoining.

2.1.2 Microjoining

Microjoining refers to precise joining of parts, defined by a weld seam width and penetration depth of less than 1 mm [87]. Examples of microjoining processes appear in fields such as electric component assembly [88–90], watch industry [91], and medical device fabrication [92, 93]. The most common method for microjoining is laser welding [87], which is advantageous for joining of small components: it has low heat impact on the material compared to plasma arc welding, and unlike friction welding, it does not introduce plastic deformation [94]. Additionally, it is capable of creating hermetically tight weld seams with foils of as little as 5 μm thickness [95]. This fusion welding method is appealing for the fabrication of the metal MEMS devices of this work to achieve reliable, hermetic weld seams. However, this process may induce material defects that have major implications on device functionality. Hence, this section presents the joining process and its technological challenges, as well as diffusion bonding as an alternative joining method in detail.

Laser welding of metals is a fusion process that is based on material melting of two or more joining partners by introduced heat from a laser beam [96]. The molten material subsequently solidifies to form a joint fusion zone of the joining partners, which creates a metallurgically-bonded connection. It is used to join steel alloys [92, 97–99], titanium and titanium alloys [100], and dissimilar metals [43, 88, 101]. Laser welding is frequently used for many applications, such as biomedical devices and implants [93], as it offers efficiency through high energy density, high penetration depths, and small welds with spot sizes in the range of $10 - 100\,\mu$m [87]. The laser welding process involves many complex aspects such as melting and flow of molten material [102, 103], metal vaporization [104–106], solidification rate and fusion zone microstructure [107, 108], and heat transfer [103, 109, 110]. Therefore, researchers devote many experimental and some numerical studies on this microjoining process and its interactions.

Microjoining research of the past decades covers choice of laser for various welding tasks, elaborates on challenges of laser welding, and adaption of process parameters to

improve weld quality. The following presents a brief introduction into these aspects to build up knowledge of influencing effects on the metal MEMS functionality. Along with CO_2 lasers [104] and solid-state lasers based on Nd:YAG crystals [91, 104, 111], fiber lasers are commonly used for microwelding of thin foils [97, 105, 111, 112]. Main advantages of fiber lasers are high beam quality, high efficiency, and suitability for highly reflective materials. Regardless of the type of laser, laser welding of thin metal foils poses many challenges investigated in literature:

- Spatter generation [113]
- Oxidation and shielding gas supply [105]
- Focus shift and beam shape deformation due to thermal load and plume [95, 99]
- Bonding defects, material burn through, and undercutting due to insufficient contact of the joining partners [114]
- Humping, the effect of periodically ejected solidified droplets [115]
- Porosity/blow hole generation in the fusion zone [104]
- Heat affected zone (HAZ) and material warpage [44, 92, 98]

To effectively overcome those difficulties, microjoining necessitates intricate set-up of process parameters. Depending on the materials used, thickness of foils, and welding joint type, stable and high quality welding requires optimized laser feed rate [90, 98], beam size [97], laser power [98, 99], focal plane position [116], and, in case of pulsed laser welding, pulse power and duration [100, 117]. Thorough process development of these parameters solves the majority of possible challenges. However, the thermal stress and generated material warpage from the HAZ within thin metal foils remain problematic. The HAZ is the zone adjacent to the fusion zone, where elevated temperatures below melting temperature of the metal occur [96]. As a result of the high temperatures and subsequent cooling in the HAZ, the metal microstructure changes, which causes the material properties within this non-melted area to alter [118, 119]. Similar to annealing of thin foils after cold-rolling (see Section 2.1.1), a possible countermeasure to material warpage caused by thermal stresses is stress relief by high temperature post-processing [120–124]. As described above, such an approach is not pursued as stress relief annealing leads to a loss of the high-strength properties of the strain-hardened metal sheets.

Patschger dedicates many studies on empirical optimization of microjoining of thin metal foils to minimize material warpage of the HAZ [95, 106, 114, 125–127]. The investigations involve laser microjoining of $15 - 100\,\mu$m thick stainless steel foils under variations of process parameters, clamping, and beam quality. The studies show that higher laser feed rate ameliorates thermal efficiency of the weld, leading to a smaller HAZ. Yet, it is important to maintain feed rate within the welding regime, as excessive laser beam velocity leads to a shift of the process from welding to laser cutting [126]. Additionally, the investigations reveal that a gap between joining partners results in weld failures if the gap exceeds approximately half of the material thickness [114]. This finding is used to define a criterion for surface roughness, as low surface quality leads to insufficient contact of the mating surfaces. On the basis of the minimal foil thickness of $25\,\mu$m used in this work, the surface roughness of the foils or rigid parts shall not exceed values of approximately $R_z = 12\,\mu$m.

In contrast to the joints of thin foils to each other in the scope of *Patschger*, the metal MEMS of this work need high joint strength when bonded to a substrate of significantly higher thickness, the rigid MEMS base. Hence, building on the process optimizations of *Patschger*, an additional approach is necessary to increase weld seam penetration depth.

Alternatively to classic welding based on heat conduction [90], a method to increase penetration depth and minimize the HAZ is keyhole welding [105, 106]. Keyhole welding leads to weld seams with high penetration depth, which increases the overall fusion zone of the joining partners. In addition to melting, it involves vaporization of metal deep within the material: The vapor pressure of the vaporized metal causes the molten metal to flow into deep cavities [87]. While many studies show successful deep penetration of metal welds of thin foils [89, 99, 111, 116, 128, 129], keyhole welding entails additional difficulties. Evaporative loss of alloying elements may occur, increasing the risk of brittle fractures between grains of the fusion zone and the HAZ [119]. Another risk involves the beam reflections within the material which increase the material absorption [89]. These multi-reflections are essential to achieve deep penetration and are advantageous for increasing the bead width [99]. However, if the laser feed rate is not fully optimized, these multi-reflections and the resulting metal vaporization raise the risk of entrapped metal gas within the joint, leading to weld seam porosity. Therefore, it is crucial to avoid keyhole multi-reflections within the thin metal sheets by careful positioning of the laser focal plane to the surface of the substrate. While such cavities are less detrimental within the substrate, they affect weld seam integrity more severely within the thin metal foils. These risks can be minimized by process optimization, making keyhole welding a powerful

technique to achieve high joint strength. To further increase fusion zone width and to avoid narrow weld seams, keyhole welding can be combined with spatial oscillation of the laser beam, the so-called "wobble function", to achieve a wider weld seam [129]. Figure 7 illustrates cross-sections of weld seam profiles as a result of the discussed approaches in laser microwelding.

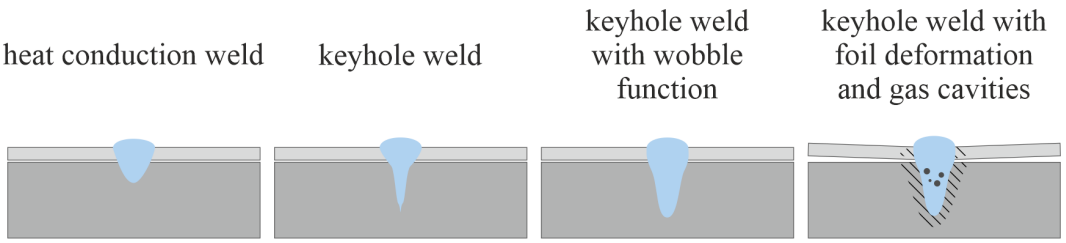

Figure 7: Illustrations of weld seam profiles of thin metal foils welded onto a metal substrate, depending on the welding method. Classic heat conduction welding leads to shallow weld seams, while keyhole welding results in deep, narrow penetration of the material. Implementation of a wobble function increases fusion zone width of a keyhole weld. Possible defects are entrapped gas cavities, leading to weld seam porosity, as well as foil deformation due to thermal stresses. A qualitative indication of the HAZ is displayed as hatched area.

Similar to *Wald et al.* [36], this work uses a fiber laser with a wavelength of 1070 nm to join the foil components of the metal microfluidic MEMS to their rigid base in a lap joint configuration. Keyhole welding at a high feed velocity of 150 $^{\mathrm{mm}}/_{\mathrm{s}}$, with the focal plane on the substrate surface, and using a wobble function ensures high penetration depths and sufficient weld seam width. Core Publication [1] provides a detailed explanation of design and assembly of the titanium micropump, which are similar to the structure and operation of the stainless steel micropump from *Wald et al.* The laser welding assembly process of the micropump begins with stacking of the passive check valve foils (see Figure 6) on the rigid base. The stack is tacked to the base with multiple micro-spot welds [92, 119] to ensure close contact of the foils to the base. A circular weld around each valve joins the valve structure to the base with a hermetic weld (see Figure 8). Subsequently, the actuator diaphragm is placed on top of the passive check valve stack. A larger circular weld joins the actuator diaphragm to the base and valve foil stack, creating the hermetic micropump chamber. The same principle applies to the circular welds of the passive and active microvalves to join their foils to the rigid components (see Core Publications [1–4]).

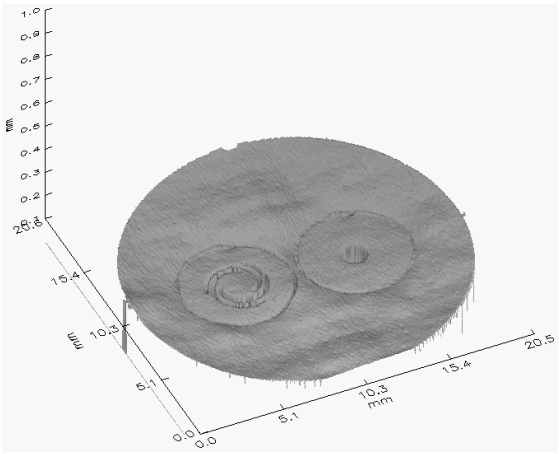

Figure 8: White light interferometry data showing the topology of a foil stack of passive check valves joined to a micropump base. The 50 μm thick foils are stacked and tacked to the rigid base with several micro-spot welds. Circular welds around each valve joins the foils to the base with a hermetic seam. Heat impacts of the laser welding process cause foil warpage, which leads to non-planarity of the foil components.

As described in Section 2.1.1, foil deformations may originate either from foil handling prior to joining or from the microjoining process itself. In the valve foils of the micropump, such foil deformations lead to an initial gap between the valve plate and its valve seat. This gap creates a leakage path, reducing micropump efficiency and pressure build-up. To evaluate the initial gap of steel and titanium micropumps resulting from the employed microjoining process, the topology of laser welded valves as depicted in Figure 8 is analyzed. The 50 μm thick valve foils are joined to a pump base with an effective laser power of 65 W. Initial gap measurements reveal that the gaps between valve plate and valve seat amount to $h_{IG,Steel} = (11.6 \pm 2.2)\,\mu$m and $h_{IG,Ti} = (9.3 \pm 2.5)\,\mu$m. Section 3.1 discusses the impact of these initial gaps on resulting pump leakage further.

Another method to examine material defects in the foil stack after laser welding is the analysis of its cross-section, as shown in Figure 9. Foil warpage of the passive check valve structures is clearly visible. Noticeable dark spots in the fusion zone potentially show entrapped gas cavities, but may also show material defects originating from cross-sectioning. Within the metal MEMS platform, foil deformations affect components of the micropump or the passive safety valve gravely: They comprise components with foil thickness $\leq 50\,\mu$m (see Sections 3.1 and 3.2), while resistance against heat-induced material warpage decreases with reduced material thickness [130]. The thermal stresses also lead to curvature in the actuator foils of pumps and valves, which must be included into design considerations of the bending actuator (see Section 2.1.3).

To ensure microfluidic MEMS functionality and to allow more complex structures within stacks of thin metal foils, optimization of the laser welding process is needed. In general, an efficient method for process optimization is using numerical and analytical models combined with experimental validation. Only few publications address the topic of modeling of the physical processes in microwelding [103, 131], as most research focuses on empirical determination of optimal weld parameters for a specific combination of foil thickness, material, and welding joint type. Furthermore, research on microwelding does not cover the modeling of joining multiple thin sheets to a substrate. An extensive optimization with subsequent experimental validation of the laser welding process is not possible within this work due to limitations in material and infrastructure availability. Therefore, laser welding process optimization is a crucial element of future developments of metal microfluidic MEMS that will build on the literature research of this thesis.

Figure 9: Light microscope photograph of the cross-section of a fully assembled metal micropump. Depicted are the PZT disk (I), the actuator foil (II), the two passive check valve foils (III), and the base (IV). Within this area of the micropump, the inlet valve (V) is presented in detail. During the keyhole welding process, entrapment of vaporized metal may cause porosity of the weld seam (VI). Additionally, foil warpage in the HAZ of the weld seams through the 50 μm thick foils are clearly visible, as thermal stresses cause buckling of the individual foils.

As an alternative to laser welding, increasing research towards diffusion bonding of thin metal sheets [132] may be suitable for the microjoining tasks in the metal microfluidic MEMS platform. Diffusion bonding is based on solid-state diffusion, induced by both, pressure and elevated temperature, on two solid materials in contact, resulting in a high-quality bond of the joining partners on atomic level [133]. *AlHazaa and Haneklaus* [132] provide an extensive review of research advances in the field of diffusion bonding of stainless steel [134–137], titanium and titanium alloys [138–140], titanium alloys to stainless steel [141, 142], and other dissimilar metal welds [143, 144]. Though diffusion bonding results in planar joints with high resistance to brittleness and residual stresses at the bond interface [132], it entails several challenges. Deformations of the metal layer surfaces induced by the applied pressure are common [132], hence, *Gietzelt et al.* devote several studies on the influence of diffusion welding parameters of stainless steel bonds [134, 145,

146]. Additionally, the research group observes decrease of mechanical properties, such as yield strength and tensile strength, due to grain growth at elevated temperature [137]. Finally, diffusion bonding is expensive, as processing times are slow [144], process parameter adjustment involves high effort [132], and mating surfaces require costly preparations such as plasma activation and fine polishing [147, 148]. Process variants like impulse pressure-assisted diffusion bonding aim to ameliorate deformations. The process introduces rapid pressure variations instead of constant bonding pressure [149], but in turn necessitates increased effort in process set-up. Consequently, diffusion bonding is a fairly uncommon process outside of aerospace engineering [132]. A unique exception is the stainless steel micropump fabrication process from *Aizawa and Shiratori* [136], who describe a batch production method that involves diffusion bonding of eight sheets. However, the authors do not elaborate on deformation effects of the joining process.

In conclusion, this thesis work does not pursue microjoining by diffusion bonding, as material preparations and process costs are relatively high compared to the established laser welding process from *Wald et al.* [36]. The diffusion bonding process may become more feasible for small batch productions of research samples in the future as ongoing research promotes process efficiency, accuracy, and cost-effectiveness. The metal microfluidic MEMS assembly of this work involves laser welding instead, with the aforementioned optimization potential as part of future developments.

2.1.3 Driving Mechanism

To fulfill their respective purposes, the driving mechanism of the microfluidic MEMS of this work establishes the fundamental dynamics of their actuator diaphragm. Various actuation mechanisms are applicable in mechanical microfluidic MEMS to enable active and passive actuation. Active micropumps and microvalves based on electromagnetic, electrostatic, thermo-pneumatic, phase change, shape memory alloy, and piezoelectric actuation have been presented in research. A comprehensive overview of research examples of these actuation principles is provided by *Bußmann, Grünerbel, Durasiewicz et al.* [32]. Among these active operating principles, actuation based on the inverse piezoelectric effect is considered an efficient and powerful driving mechanism: It combines relatively low power consumption, high force, good linearity, and fast switching time [18]. Operation of passive mechanical microvalves is based on pressure-induced movement of cantilevers, hinged plates, or balls that close a fluid path by tight contact to a valve seat [24]. The microfluidic devices of this work incorporate either a piezoelectric or pressure-induced driving mechanism. The following section describes the design methods applied in this thesis for purposeful development of the driving mechanism for metal microfluidic MEMS.

The piezoelectric bending actuator of the active metal microfluidic MEMS consists of a metal diaphragm foil welded onto the rigid base and a PZT disk actuator glued onto the metal diaphragm using epoxy. Application of an electric field causes the piezoceramic to expand and contract radially, which results in high transverse deflections of the bending actuator. It generates a volumetric flow by periodic displacement of the fluid out of the pump chamber of a micropump, displaces the suspended plunger in an NC microvalve, and exerts a closing force onto the valve seat of an NO microvalve. Core Publication [1] describes the working principles of the pump and valves in detail. To develop and improve the active component of the pumps and valves, design considerations involve both, structural and manufacturing aspects. Dedicated Finite-Element-Method (FEM) simulations provide further insights into the mechanical response of the MEMS structures to fluidic or contact pressure.

The structural design of piezoelectric actuators is based on the work of *Herz et al.* [150]. In their publication, the authors present an analytical model for the transversal and radial displacement of a piezoelectric bending actuator under pressure and voltage loading. Additionally, they investigate optimized design of a piezoelectric bending actuator for micropumps to achieve maximum stroke at certain pressure conditions. In their model, piezoceramic thickness and actuator diaphragm thickness serve as design parameters for optimized stroke. In turn, the model may also be used for optimization of micropump pressure build-up. The design of the piezoelectric bending actuators of Core Publications [1], [2], and [4] are based on this model.

Apart from structural design, a defined initial deflection of the actuator diaphragm after piezoceramic bonding is crucial for optimized micropump and microvalve functionality. The patented pretension technique of *Herz et al.* [34] is a manufacturing process for introducing a defined stress within the bending actuator to achieve a certain initial deflection after assembly. During glue curing, an applied voltage leads to contraction of the disk actuator. After the bonding process, the voltage load is released from the piezoceramic disk, which cannot relax to its initial form as it is bonded to the metal diaphragm. Hence, the transversal shear stress within the piezoceramic causes the actuator diaphragm to bend into a defined initial deflection. This electro-mechanical pretension allows to create an optimized compression ratio in micropumps as presented in Core Publication [1]. For NO microvalves, this technique enables control and optimization of actuator diaphragm position relative to the integrated O-ring soft sealing that creates

an elevated valve seat. Core Publication [2] describes the empirically achieved pretension factor for fabrication of titanium NO microvalves with optimized leakage characteristics in closed state while allowing open state water flow rates in $^{ml}/_{min}$ range.

When such a specific pretension of the bending actuator is desired, the thermal expansion of the materials during glue curing needs to be taken into account. As the thermal expansion of metal is higher than the piezoceramic material expansion, the heating, glue hardening, and subsequent cooling results in a similar effect as the electro-mechanical pretension. Since the thermal expansion coefficient of stainless steel (AISI 304; $16 \cdot 10^{-6}\,{}^{1}/_{K}$ [151]) is higher than the respective values for PZT (PIC 151; 4 to $8 \cdot 10^{-6}\,{}^{1}/_{K}$ [152]) and titanium (grade 5; $9.0 \cdot 10^{-6}\,{}^{1}/_{K}$ [94]), this thermal pretension affects stainless steel MEMS to a higher degree. For steel micropumps, this thermal pretension adds to the electro-mechanical pretension of the bending actuator, therefore, the voltage load during glue curing must be adjusted accordingly to achieve a desired compression ratio. Similarly, the pretension of bending actuators of steel NO microvalves also depends on this thermal pretension. Hence, this effect must be considered in the adjustment of the bending actuator position relative to the valve seat height.

In contrast to the micropump and NO microvalve, the assembly process of the NC microvalve does not involve an electro-mechanical pretension process. Instead, a flat initial shape of the bending actuator is desired to ensure close contact to another mechanical component of the NC microvalve: the suspended valve plunger. Core Publication [1] provides a detailed description of the structural design and working principle of the NC microvalve. This includes the spring force of the 25 μm thin spring foil that serves as the plunger suspension. This spring force ensures tight closing of the valve in non-actuated state. During actuation, the piezoelectric bending actuator displaces the plunger downwards to open the fluid path through the microvalve. The restoration force of the spring foil acts as a counterforce during actuation. Additionally, the fluid pressure contributes to this counterforce of the bending actuator force, as the pressure acts on the spring foil within the valve chamber. Therefore, design considerations of the driving mechanism working at a certain fluid pressure require careful balance of the piezoelectric force and the restoration force of the spring foil. For failure analysis and subsequent optimization, my thesis work includes an FEM analysis using *ANSYS Mechanical*. It is used to investigate the malfunctioning NC microvalves of Core Publication [1], and allows NC valve optimization presented in Section 3.3.

For operation of the passive microvalve of this work, the driving mechanism is based on a pressure-induced movement of an actuator diaphragm. The structural design of the passive safety valve is similar to the active NO valve, as it comprises a rigid base with an integrated O-ring soft sealing. The design and working principle of the passive safety valve is thoroughly described in Core Publication [3], including the pressure-induced movement of the 50 μm thin actuator foil. A pressure gradient acting on the actuator foil enables a deflection that opens and closes the fluid path through the valve. As it serves as an addition to the metal micropump to create a microdosing drug delivery system (see Core Publication [3]), it is essential to consider the generated pressure of the micropump. The generated fluid pressure contributes to the pressure gradient and therefore, it is a boundary condition in the design considerations of the driving mechanism. These design considerations and the development work of the driving mechanism of the safety valve are presented in the following.

To design the driving mechanism of the safety valve, it is necessary to consider the spring characteristics of the foil as well as the desired deflection of the actuator at a given pressure gradient. By design, the actuator foil inhibits an initial spring force similar to the NC microvalve. It is introduced by an initial deflection of the actuator foil after welding, as the elevation of the soft sealing creates an elevated valve seat. It is worth noticing that the effective spring force of the actuator foil is also highly dependent on the manufacturing accuracy of the soft sealing, see Section 2.1.4. This initial spring force in resting position adds to the initial tightness of the valve and establishes a delivery valve behavior: The generated pump pressure must overcome this initial spring force to open the valve. As bubbles may occur in any microfluidic system, this opening pressure must take considerations on bubble tolerance of the micropump into account. The ⌀20 mm metal micropump is considered bubble tolerant up to a pressure of 30 kPa (see Core Publication [1]). To ensure fluid delivery through the valve in the case of bubbles present in the micropump, the opening pressure of a safety valve shall be this bubble tolerance pressure with a safety factor of 2. Hence, the desired deflection of the stainless steel actuator foil at a pressure gradient of 15 kPa shall be 50 μm, which is the nominal valve seat height. The adaptable design parameters that define the spring foil stiffness in the safety valve are actuator foil thickness and foil diameter. The diameter of the moving area of the actuator foil is determined by the welding diameter, where the actuator foil is attached to the rigid base. To study the actuator foil deflection under pressure load, a model for mechanical simulation of the actuator foil is created in *ANSYS Mechanical*.

In the mechanical simulation, a variation of foil thickness and effective actuator diameter provides insight into the resulting spring characteristics dependent on the design parameters. Foil thickness is varied between $10 - 100\,\mu$m, and actuator diameters of 10.4 mm and 18 mm are modeled. A pressure load up to 20 kPa is applied. Figure 10 shows the resulting deflection of the actuator foil under variation of foil thickness.

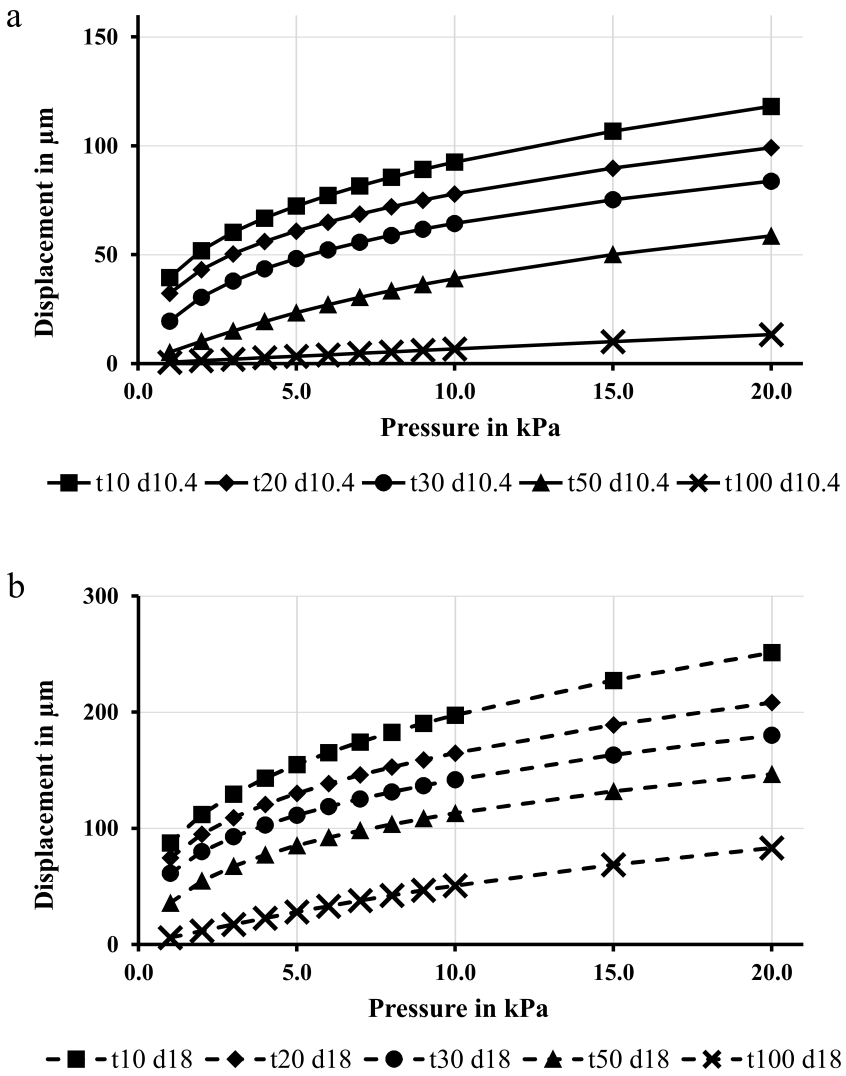

Figure 10: FEM results of pressure-deflection characteristics of stainless steel foils. The data shows deflection of the center of the foil with thickness varying from 10 to 100 μm, and effective actuator diameters of 10.4 mm (**a**) and 18 mm (**b**).

The results show that both, foil thickness and reduced weld diameter, lead to expected increase of the stiffness of the actuator foil. At the desired opening pressure of 15 kPa and with a weld diameter of 18 mm, any foil thickness $\geq 10\,\mu$m exhibits a deflection above the desired value of 50 μm. At a reduced weld diameter of 10.4 mm, a foil thickness of 50 μm results in a deflection of approximately 50 μm. These results render this foil thickness and diameter combination a good design for a safety valve incorporating an O-ring with a nominal elevation of 50 μm. Based on the results of this parameter study, the fabricated safety valves presented in Core Publication [3] have a foil thickness of 50 μm, and a reduced weld diameter.

The MEMS developments within this thesis build on the knowledge gained through numerical and experimental analysis. They are used for both initial development of the first generation of devices as well as optimization in further development steps.

2.1.4 Sealings

In addition to the driving mechanism, the valve seat is an integral part of a microvalve. The combination of a high contact force and a well-designed valve seat achieves tight sealing of a microvalve in closed state. Section 2.1.3 describes the design of the driving mechanisms of the microvalves in this work. The following involves the challenge of creating tight sealing while low fluidic resistance in microvalve open state is desired. In contrast to other standard MEMS materials such as silicon, the surface roughness of metal MEMS components contribute severely to detrimental leakage flows. Hence, additional sealing elements within the microfluidic device such as soft sealings, thin-film coatings, or other measures are evaluated to develop feasible sealing technologies for metal microfluidic MEMS. Additionally, an analytical approach is used to build a deeper knowledge of the interactions leading to leakage flows.

The tightness of valve seats is optimized by incorporation of sealing elements [153–158], by sophisticated structural valve seat design [159–164], or by enhancing the surface quality of the surfaces in contact [159]. In literature, microvalves with elastomers [154, 165], gels [166–168], or paraffin [17, 169, 170] as part of the driving mechanism often show no or low water leakage rates as low as $0.013\,\mu\text{l}/\text{min}$ [167], while open state flow rates remain below $10\,\text{ml}/\text{min}$ [154]. Within the metal microfluidic MEMS platform developed in this thesis, the intended purpose of the microvalves is to combine them with a micropump in a medical microfluidic system. Therefore, the sealings of microvalves are designed to account for the interdependency with the metal micropump to achieve low fluidic

resistance in flow direction of the system. The developments within this thesis aim for low leakage rates in closed state while allowing open state flow rates in the same order of magnitude as generated by the micropump. To this end, the sealings of metal microvalves must inhibit advantageous properties like elasticity or flow effects to impede leakage, whilst avoiding obstruction of the fluid path in open state. To minimize fluidic resistance, the developed microvalves incorporate a valve seat in the MEMS base with valve seat heights below or equal to $50\,\mu$m. The developments within the metal microfluidic MEMS platform cover various investigations of different sealing types in microvalves discussed in the following.

Core Publications [1], [2], and [3] present micro O-rings serving as valve seats in active NC and NO microvalves as well as in the passive safety valves. The fluorocarbon (FKM) sealing rings with circular cross-section are biocompatible, easily installed into micromilled notches in the metal base, and commercially available with nominal chord size as low as $500\,\mu$m. Based on the design considerations of their respective driving mechanism (see Section 2.1.3), the O-rings are integrated into the rigid MEMS base such that the sealing protrudes over its notch with a nominal height of $50\,\mu$m. This protruding part of the O-ring is deformed by the actuator in closed state for tight sealing and creates an elevated valve seat with a height h_{VS}. When contact forces are high, such as the spring force of the NC microvalve (see Core Publication [1]), the rubber material has good sealing capabilities with leakage rates below $1\,\mu\text{l}/\text{min}$ over a wide range of applied fluidic pressure. Conversely, leakage evaluations of NO microvalves or passive safety valves result in leakage rates in the range of $10 - 40\,\mu\text{l}/\text{min}$ at 20 kPa. These results indicate that the required contact force of the O-ring material for ensuring good tightness quality may be high compared to the achievable force of the driving mechanism of these NO valves and passive safety valves. To obtain the elastic deformation characteristics of the rubber sealing, extensive experimental characterization is necessary. Analytical models like Mooney-Rivlin [171–173], Ogden [171, 174], or Neo-Hookean models [175] describe the stress-strain relationship of hyperelastic materials, such as rubber, but depend on experimentally derived coefficients. Due to limitations in test infrastructure, such experimental characterizations are not performed within this thesis to obtain material data for the specific rubber composition used. In Core Publication [3], literature data [176] is used to approximate the elastic behavior of the FKM O-ring after installation into the notch of the safety valve. However, analytical or numerical modeling of the deformation of O-rings in microvalve closed state is not pursued in this thesis. This is due to high manufacturing deviations of the micro O-rings that pose serious difficulties

to both modeling and fabrication. In Core Publications [1] and [3], the manufactured research samples of NC and NO microvalves as well as safety valves show large scattering of experimental data. Component characterizations reveal that O-ring chord sizes vary strongly with $(495 \pm 33)\,\mu$m for NO valve and safety valve sealings and $(585 \pm 45.5)\,\mu$m for NC microvalve sealings. Based on their nominal chord size of $500\,\mu$m, the desired O-ring elevation over its notch results in a valve seat height $h_{VS} = 50\,\mu$m by design. Any deviation of the O-ring chord size directly leads to divergence of h_{VS} from the targeted design value. Due to the strong dependency of the initial spring load of the NC microvalve and safety valve (see Section 2.1.3) to h_{VS}, deviations of O-ring chord sizes affect the functionality of these microvalves severely. Additionally, O-ring chord sizes vary azimuthally by $(36.5 \pm 19.4)\,\mu$m. This causes the actuator foil to get in contact with peak elevations of the O-ring, while valleys in the O-ring topology allow leakage flows. These severe manufacturing inaccuracies lead to large deviations in experimentally obtained leakage rates of microvalves and render numerical or analytical modeling comparative to the fabricated samples infeasible. Core Publication [2] presents an adapted fabrication process, which includes individual characterizations of h_{VS} in NO microvalves to account for O-ring manufacturing inaccuracies. While the proposed electro-mechanical pretension process improves sample-to-sample variation of leakage rates in NO microvalves, it involves high effort in characterization and selection of O-ring sealings. Furthermore, the installation of the O-ring sealings is problematic, as the FEM analysis in Core Publication [3] shows: In microvalve open state, the fluid flow induces a lift of the sealing component which subsequently obstructs the fluid path. To avoid such failure states and difficulties due to manufacturing inaccuracies, microvalve sealings with higher manufacturing control are developed.

As an alternative sealing concept, thin-film coatings on a valve seat achieve advantageous sealing properties. The elasticity of polymers can be used to accomplish high deformations of the sealing material, creating tight seals against a surface in contact. Coating materials presented in microvalve research are polymers such as silicone [177–179], polyimide [180, 181], or Parylene-C [159, 165]. The latter is a chemically inert, biocompatible polymer which is a standard material in medical applications such as implant coatings [182]. Fabrication of Parylene-C coatings is based on chemical vapor deposition (CVD), a precise manufacturing method that offers high yield, pore-free coating, as well as high control of coating thickness. Core Publication [4] describes CVD of Parylene-C in detail.

To improve microvalve tightness whilst eliminating the disadvantages of a movable sealing component, research samples of safety valves are fabricated with 5 and $15\,\mu$m thin

Parylene-C coatings that serve as the valve seat. As this reduction in h_{VS} significantly reduces the initial spring load of the actuator foil, these safety valves comprise steel foils with individual thickness of 25 and 40 μm, structured via PCM from commercially available foil material. To allow microjoining by laser welding, coating of the actuator foils is limited to a circular central area, which, in closed state, is in contact with the valve outlet. Partial Parylene-C deposition is achieved by masking of the foil with a structured mask. After CVD, the exposed steel surface as well as the mask are coated with Parylene-C. As the coating creates a connected transition from the mask to the steel surface, mechanical stripping of the mask causes delamination of the desired Parylene-C coating. Therefore, the mask must be separated from the desired coating area. To this end, a sharp blade is used to manually cut the Parylene-C coating in the transition area.

Examinations of the fabricated actuator foils reveal that the cutting process causes a plastic deformation of the steel foil. Hence, the fabricated safety valves show high leakage rates in closed state due to insufficient contact of the actuator foil to the valve seat, as described in the bachelor thesis by *Güntner* [183]. Additionally, coatings of 5 μm thickness show poor adherence to the steel surface after mask removal, while 15 μm thick coatings exhibit sufficient adhesion. To remedy material defects as a result of the mask removal process, this manufacturing procedure is optimized further.

The work presented in Core Publication [4] involves an improved manufacturing process of thin-film coatings for metal microfluidic MEMS to create steel NO valves with Parylene-C coatings. Figure 11 depicts the optimized process flow applied in this respect. Instead of a coated actuator foil, partial coating of the microvalve base is employed, as the rigid component poses less difficulties in handling. A semiconductor wafer processing tape covers the microvalve base. Subsequently, the tape is laser cut to expose the steel in the desired coating area. After Parylene-C coating via CVD, a laser ablation process is utilized instead of a manual cutting process. A CO_2 laser with a wavelength of 10.6 μm removes the coated mask in the transition area by infra-red laser ablative micromachining. To minimize laser ablation processing time, the laser-aided mask removal is limited to the transition area of the coating. After the remaining mask is separated from the desired coating area, the mask can be mechanically stripped, and the microvalve bending actuator assembly process follows. This improved manufacturing process is successfully utilized to fabricate coated microvalves in Core Publication [4] without introducing material defects.

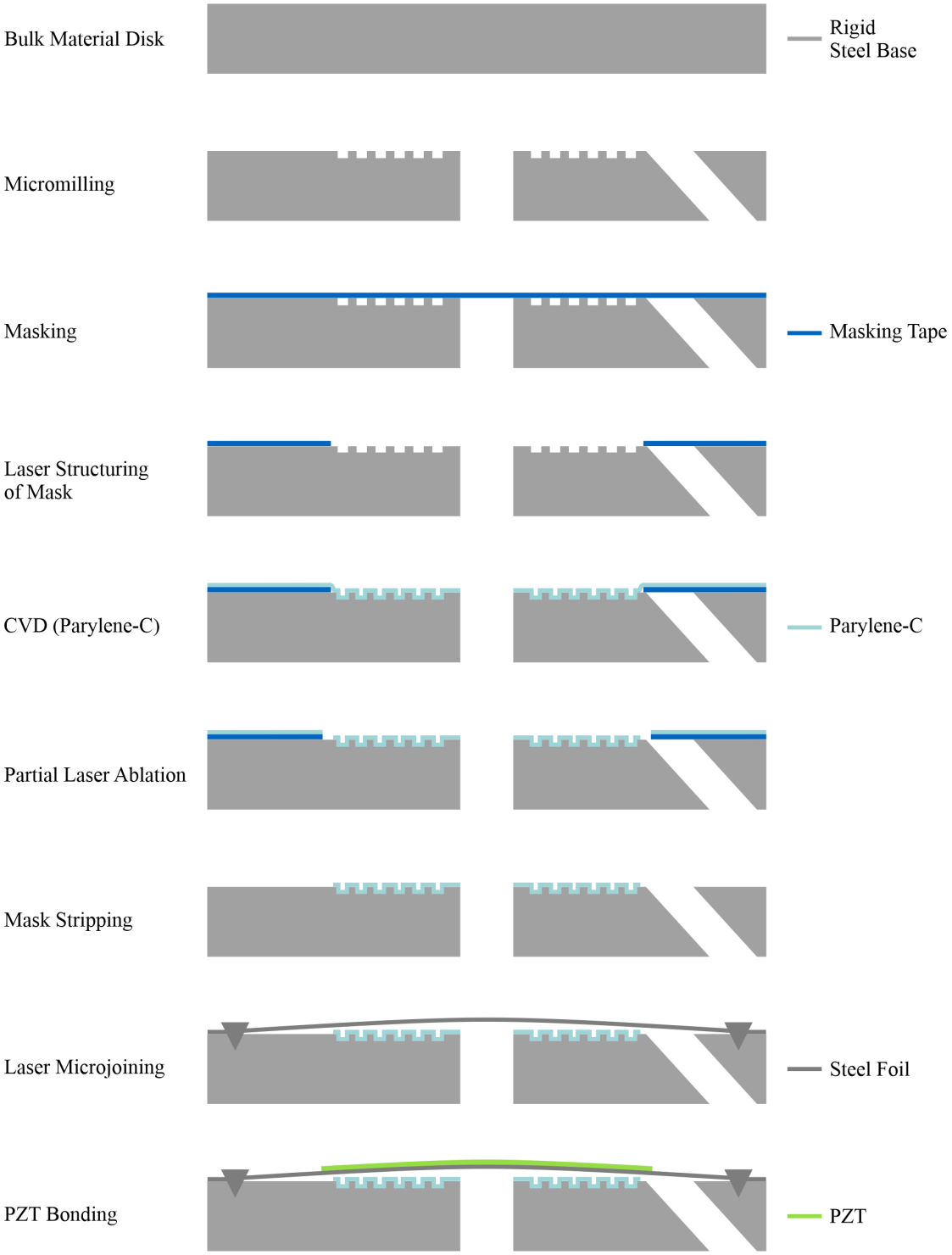

Figure 11: Process flow for manufacturing an NO microvalve with a Parylene-C coated valve seat as presented in Core Publication [4].

While only some NO microvalves of Core Publication [4] are coated, all NO valves of this study possess a micromilled concentric trench structure. This structure serves as a valve seat, similar to silicon microvalves with concentric valve seat rings reported in literature [159, 162]. A sophisticated valve seat structure can achieve tight sealing based on fluidic effects and improved contact mechanics. Core Publication [4] thoroughly describes the anticipated sealing effects of the valve seat trenches, such as fluidic losses due to shear stress. These sealing effects depend on the structural design of the valve seat trenches, which is analyzed by *Hölzl* in an FEM parameter study to obtain design knowledge for potential optimization. The fabrication of the valve seat structure is based on micromilling for high precision microstructuring (see Section 2.1.1), successfully mitigating manufacturing deviations of the valve seat. As experimental evaluations of the NO microvalves show, this approach is suitable for manufacturing of well performing valves (see Section 3.4).

Maier derives an analytical model presented in Core Publication [4] to calculate leakage flows in metal microfluidic MEMS. The model considers the microfluidic flow through the interface of the valve seat and the actuator foil under the influence of contact pressure. It assumes a laminar Poiseuille flow, and the leakage channel height is derived based on the contact mechanics model of *Persson* [184]. The latter is used to calculate a separation height of two surfaces in contact depending on a certain contact pressure. This separation height further depends on the surface roughness as well as the Young's moduli of the materials in contact. The fractal dimension of the metal components is measured as a metric for surface roughness, and the bending actuator model from *Herz et al.* [150] (see Section 2.1.3) is used to calculate the contact pressure. Comparison of the analytically derived leakage flow to experimental data shows that this model is apt to estimate the leakage flow rates of microvalves with and without additional coating on the valve seat. However, further improvements of the model are necessary to enable accurate predictions, as worst case assumptions are made to calculate the separation height.

The design of sealings and valve seats for microfluidic MEMS involves considerations of various fluidic and mechanical effects as well as manufacturing influences. This work advances the understanding of such interdependencies based on experimental, numerical, and analytical investigations. The advancements of structural designs of microscale sealing structures allow fabrication of microvalves with low manufacturing deviations. Moreover, future developments can promote sealing performance based on analytical modeling of leakage rates and the optimization of surface quality and contact pressure.

2.2 Safety Aspects

To protect patients from any bodily harm, medical device developments must mitigate safety risks with utmost care, and are subject to exacting regulations. For medical device approval by the U.S. American Food and Drug Administration FDA, manufacturers must "provide reasonable assurance of the safety and effectiveness" [185] of their device. Once fully developed, it is mandatory to guarantee a high level of device safety in all aspects to protect patient welfare and life. This work resembles advance development of technology for medical devices, and is therefore not subject to any medical device regulations. However, it is important to consider safety and effectiveness requirements from the early development on to avoid costly design changes at progressed stages or termination of development. Hence, several requirements of a safe medical microfluidic device are considered. Safety requirements of medical devices include electrical safety, hermeticity, failure detection, and biocompatibility. Additionally, for drug delivery, uncontrolled drug delivery may be lethal and must therefore be securely prevented. In case of implantable devices, compatibility with medical imaging such as MRI and radiography is necessary. Finally, hydraulic implants often need a pressure release mechanism of the pressurized part in case of power loss of the device. The following discusses possible solutions as well as the safety considerations and efforts of the developments of metal microfluidic MEMS in this work.

Electrical safety is ensured by isolation of the system electronics and all electrical components from any components and surfaces in contact with the patient. In microfluidic MEMS such as micropumps and microvalves, electrical isolation of the piezoceramic to the metal parts must be included in future developments, for example with polymer insulations [186–188].

Furthermore, all electrical components must be hermetically sealed from the body, not only to prevent any possible damage to the patient, but also to avoid damage of any electronic parts. A hermetic seal prevents any adverse effects by interactions of bodily fluids with any part of an implant or leakage of drugs from a drug delivery device. Hermeticity of a metal-based microfluidic system containing metal microfluidic MEMS is readily achieved by laser welding as described in Section 2.1.2 and is a key feature of the metal MEMS platform to avoid leakage.

As leakage of drugs is an extreme health risk to the patient due to possible lethal overdosing, leakage protection is one of the most critical safety requirements. Hence, a possible risk mitigation measure is to introduce a safety component to the system:

For drug delivery applications, the passive safety valve presented in this thesis prevents freeflow through a micropump (see Core Publication [3]). Its patented concept impedes system failure in form of freeflow as a result of external pressure acting on the microfluidic system, hence increasing system safety by design.

Other failure states include fluid path occlusion due to bubbles, agglomeration of drugs or other molecules, or particles, hindering a desired fluid flow. Such failures are detectable in a microfluidic system by added pressure sensors [189–191], but require additional space in the system. To efficiently save space, a bubble or general occlusion detection may be implemented by self-sensing as shown by *Zhang et al.* [192]. Their micropump incorporates piezoceramics with segmented electrodes, therefore, the piezoelectric transducer can be simultaneously used as an actuator as well as a sensor, using both the inverse and the direct piezoelectric effect. The reported self-sensing ability to monitor the generated flow rate can be used to detect deviations from the expected flow rate or full fluid path occlusion. An alarm capability may be connected to such a failure detection, equally important in wearable as well as implantable medical devices.

Both use cases have different prerequisites with a view to required biocompatibility: Implants are in direct contact with the human tissue and are thus often hermetically sealed within a titanium casing [193], as titanium and titanium alloys are safe for use in the human body and offer good tissue compatibility [45, 49, 194]. All components within such a titanium casing must also be compatible with medical imaging, such as MRI, to avoid artifacts [46–48]. Titanium is readily compatible with MRI and other medical imaging techniques [45]. To achieve high tensile strength and a Young's modulus comparable to stainless steel ($E_{Titanium} = 114\,\mathrm{GPa}$ [195] and $E_{Steel} = 195\,\mathrm{GPa}$ [196]), titanium grade 5 (Ti6Al4V) is used for all titanium MEMS in this thesis. Conclusively, the titanium based microfluidic MEMS presented in Core Publications [1] and [2] fulfill many requirements of implants with a view to biocompatibility, medical imaging, and hermetic system integration into a titanium implant casing. In a drug delivery device, all components that are part of the fluid path are connected to the human body. Thus, all wetted surfaces as well as surfaces in contact with the body must be chemically inert to the drug as well as all bodily fluids and cells to avoid any undesirable effects in the patient [5]. Stainless steel alloys are suited materials for such biocompatibility requirements [194, 197] and are advantageous over titanium in terms of cost-effectiveness. Therefore, stainless steel is used for micropumps and passive microvalves for the envisaged drug delivery system outside of the body (see Core Publications [1] and [3]). It is also an economical material choice for initial development lots: When the intended use is an implantable application, using steel as a MEMS material may be an adequate choice to achieve proof

of concept of a certain design feature. In my work, I pursue this approach in Core Publication [4], where steel NO microvalves are fabricated to investigate a micromilled valve seat. Here, stainless steel is a less cost-intensive alternative to titanium, that is the obligatory choice of material for metal MEMS in the final implantable hydraulic application presented in Core Publication [1].

In said Core Publication [1], I present both, the NC and NO microvalve, as suitable components of the microfluidic hydraulic system. Careful selection of the default state of the microvalve is necessary as a result of considerations on the system architecture: In an hydraulic implant, a pressurized reservoir restores a lost body function as the generated pump pressure acts on or within a body tissue. It is a crucial safety aspect of this operating principle to prevent any harmful pressure load on or within a body tissue in non-operated mode to account for possible power loss of a battery-driven device. Hence, depending on the system architecture, an NC or NO default state of a microvalve plays an important role in the overall safety of the system. These dissimilar characteristics of the developed microvalves contribute to the adaptability of the metal microfluidic MEMS platform for creating safe medical devices.

In conclusion, the microfluidic devices of the developed metal MEMS technology platform account for various safety requirements for medical devices, such as biocompatibility, hermeticity, medical imaging compatibility, and flow path control. Other safety aspects must be included in the future, such as electrical safety and failure detection, to advance technology readiness for implantable hydraulic or wearable drug delivery applications.

2.3 Reliability Aspects

Medical devices must guarantee the effectiveness of their device, as well as the stability of the desired functionality to gain approval for clinical use. The ability of proper function over service life time is referred to as reliability, though it is necessary to obtain a clear understanding of the term in the respective application. In the context of the metal microfluidic MEMS platform, it is reasonable to review the definition in the ISO (International Organization for Standardization) standard 14708-4 for implantable infusion pumps. It specifies that manufacturers of active medical devices must "establish appropriate life tests to ensure reliability of the device over the projected service life", which shall determine the performance of the device over time [198].

As described in Section 2.2, this work is an advance development of medical device technology and is therefore not subject to the respective regulations and standardizations. Nevertheless, this thesis aims for early insights regarding the suitability of the metal microfluidic MEMS platform for medical applications: While in early development stages, exhaustive reliability tests may not be possible due to limited sample quantity. Hence, the studies in Core Publications [1], [2], and [4] involve fatigue testing of few research samples as first steps towards reliability analyses. Though an absence of failures or degradation cannot fully guarantee the reliability of a designed device, early indications of weak points, possible failure states, and aging effects may be detected using fatigue tests. In the Core Publications [1], [2], and [4], NO microvalves are operated at elevated actuation frequencies in order to speed up the cumulation of actuation cycles up to a total number of $1 \cdot 10^6$ actuations. Subsequent material inspections and performance analyses allow for initial reliability considerations as well as comparative evaluations of design variations within a DoE. In Core Publication [1], the first generation of metal NO microvalves are subjected to fatigue testing to examine possible material defects of the piezoceramic as a result of mechanical stress when the bending actuator touches down on the O-ring valve seat. The DoE of NO microvalves in Core Publication [2] investigates the suitability of the empirical pretension factor for linear actuator position adjustment respective to valve seat height. The fatigue test serves as an additional test parameter to evaluate the adaptability of the proposed piezoceramic bonding process. Similarly, the DoE of NO microvalves in Core Publication [4] uses fatigue testing as an additional measure to assess the performance capabilities of different design variations in combination with concentric valve seat trenches.

The extend of the fatigue tests conducted within this work is limited and the sample quantity in each study are small. Yet, they can be used as an additional performance criterion in comparative analysis within a DoE, or serve as early failure indicator tests. Future investigations of the metal microfluidic MEMS of this work must include extensive reliability tests to provide dependable data of device performance over lifetime.

3 Devices developed within the Metal Microfluidic MEMS Platform

This chapter presents the development efforts to establish a metal microfluidic MEMS platform for medical applications. It describes the individual optimizations along with the references to the Core Publications in which the research findings are presented. The developments include a micropump, a passive safety valve, an NC microvalve and an NO microvalve. Depending on their intended use, key attributes of all microfluidic MEMS are defined to ultimately accomplish effective and safe medical devices. The individual sections of this chapter summarize the developments of each microfluidic MEMS device. In addition to the results presented in the Core Publications [1–4], this chapter includes so far unpublished work of microfluidic MEMS optimization. The sections provide experimental results of electro-mechanical and fluidic characterizations of the fabricated MEMS of this thesis, as well as research suggestions for further developments of the devices.

Figure 12 provides an overview of the respective development steps of each device. It gives references to previous works, depicts the developments within this thesis, and provides an outlook on future development steps. Based on previous design efforts, the micropump and the NC microvalve are further developed for targeted optimization of their fluidic performances. The NO microvalve as well as the passive safety valve are originally designed in this thesis: my work realizes first manufactured research samples to show their feasibility with subsequent optimizations. Sections 3.1, 3.2, 3.3, and 3.4 discuss the individual developments in detail.

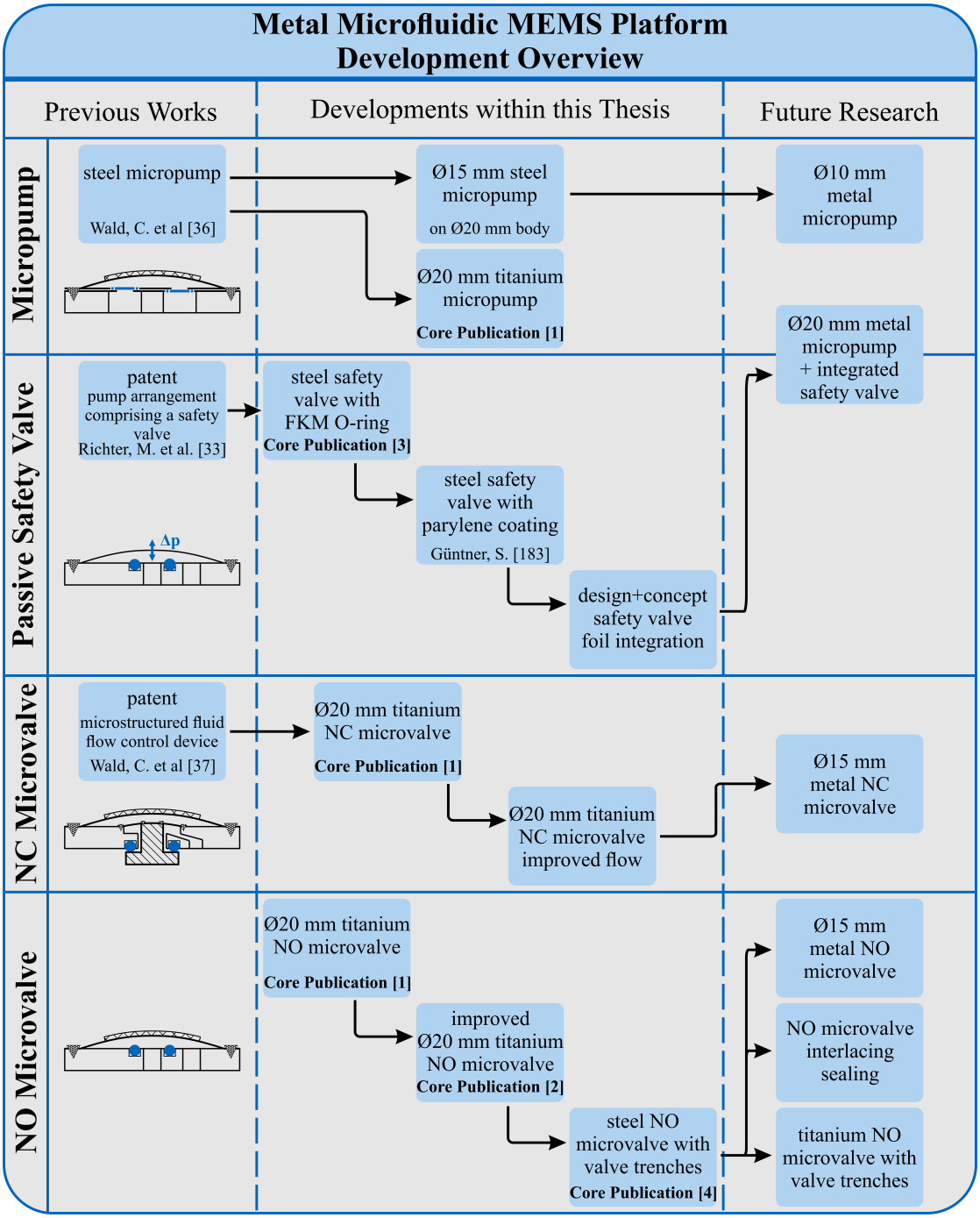

Figure 12: Overview of metal microfluidic MEMS developments. Depicted are the previous works that laid the foundation for the metal microfluidic MEMS platform, the developments I conduct within my thesis, as well as next steps of platform development, in some instances already initiated by my work.

The effectiveness of a medical device is fulfilled once it achieves its intended purpose: to improve patient well-being. The proposed medical applications of the metal microfluidic MEMS platform lead to specific requirements based on the clinical need. Comparing a wearable drug delivery device to an implantable hydraulic system, different fluidic performances lead to the desired functionality of the medical device. While some fluidic characteristics of pumps and valves are fundamental to achieve this functionality, others may not relate directly to the effectiveness of the device, but to safety or efficiency. Hence, Table 1 provides an overview of these fluidic performances, either defined as key or secondary attributes. In the following, these definitions are described thoroughly for pumps and valves with regard to the application.

Table 1: Overview of key and secondary attributes of metal microfluidic MEMS respective to the intended medical application.

Wearable Drug Delivery System		
microfluidic MEMS	*Key Attribute(s)*	*Secondary Attribute(s)*
Steel Micropump	Freeflow Leakage, Dosing Stability, Max. Pressure	Max. Flow Rate
Steel Safety Valve	Freeflow Leakage	Open State Flow Rate
Implantable Hydraulic System		
microfluidic MEMS	*Key Attribute(s)*	*Secondary Attribute(s)*
Titanium Micropump	Max. Pressure, Max. Flow Rate	Leakage
Titanium NC or NO Valve	Leakage	Open State Flow Rate

A micropump is a fluidic micromachine that generates fluid flow and builds up fluid pressure. It is the central component of most microfluidic systems as it enables fluid delivery to a desired target or pressure build-up inside a hydraulic reservoir. The functionalities of microfluidic systems are based on these central pump abilities, hence, they are important attributes of a micropump. Specifically, a micropump for drug delivery must ensure stability and repeatability of the dosed fluid volume. Though, this key attribute is not subject of this thesis, but is investigated in detail by *Bußmann et al.* [199].

A crucial prerequisite to precise drug dosing is high backpressure capability of the micropump. This key attribute enables reliable pumping against tissue pressure as well as hydraulic actuation of an implant to restore lost body functions (see Core Publication [1]). Another obligatory key attribute of a drug delivery system is the prevention of freeflow leakage, mandatory due to the significant health risks of uncontrolled drug release (see Section 2.2). In contrast, backwards leakage flow in an hydraulic implant may be considered a secondary attribute. Here, leakage flows lead to pressure loss in the hydraulic reservoir, merely diminishing system efficiency in contrast to posing a health risk. High generated flow rates greatly benefit response time of an hydraulic implant, rendering this property another key attribute. Adversely, drug delivery applications necessitate precise, repeatable flow rates instead of maximized flow. Hence, in the context of drug delivery, high flow rate capability is ranked lower in priority.

Reviewing the purpose and requirements of microvalves, it becomes apparent that opening and closing of a fluid path is fundamental for active and passive valves, regardless of the envisaged application. The passive safety valve serves as a risk mitigation in combination with the micropump, preventing uncontrolled drug flow; whereas an active NC or NO microvalve enables arbitrary fluid path control for confinement of a high pressure fluid in an hydraulic reservoir. The basic opening and closing functionalities of valves determine their shared key and secondary attributes. To ensure leak-tight closing of a fluid path, low leakage flow rates in closed state are a fundamental key attribute for all microvalves. In microvalve open state, enabling high flow rates through the valve is preferable. Low fluidic resistance enables fast response time of a hydraulic system and is desirable to not impede the generated flow of the micropump. Hence, increase of the open state flow rate is an important secondary development goal, while leakage flow remains key attribute of the microvalve.

The developments within the metal microfluidic MEMS platform optimize the devices based on these key attributes as well as the other fundamental properties presented in Figure 4. The subsequent sections cover each metal microfluidic MEMS device and their respective development steps in detail, including so far unpublished work.

3.1 Micropump

The developments of the piezoelectric metal micropump are based on the stainless steel pump presented by *Wald et al.* [36]. The authors report air flow rates of $> 100\,^{\mathrm{ml}}/_{\mathrm{min}}$ generated by the ∅20 mm steel micropump, but do not present any data of generated water flow. This thesis investigates the liquid flow and pressure capabilities of the ∅20 mm metal micropump, the adaption of the micropump to fulfill requirements of implantable systems, as well as size reduction.

Core Publication [1] presents the fabrication and test of AISI 304 steel micropumps and introduces the titanium micropump intended for implantable use. Based on its Young's modulus comparable to steel (see Section 2.2), titanium grade 5 (Ti6Al4V) is selected, as it exhibits the required medical imaging compatibility for implantable systems. Both steel and titanium pumps show similar maximum water flow rates above $12\,^{\mathrm{ml}}/_{\mathrm{min}}$ and blocking pressure of 75 kPa, suitable for the envisaged hydraulic application. Evaluations of the energy consumption per transported fluid volume reveal high efficiency of the metal micropumps compared to other pumps presented in literature [200, 201]. The water leakage rates at 5 kPa backpressure amount to $(40 \pm 10)\,^{\mu\mathrm{l}}/_{\mathrm{min}}$ for steel pumps and $(50 \pm 40)\,^{\mu\mathrm{l}}/_{\mathrm{min}}$ for titanium micropumps. While mean values are similar, the large scattering of leakage rate data may be caused by a high variation of initial gaps. As described in Section 2.1.2, further development efforts towards a deep understanding of the laser welding process are necessary to optimize micropump leakage.

Following the research findings reported in Core Publication [1], an exploratory feasibility study is pursued to develop a miniaturized metal micropump with increased pressure build-up. A weld seam of 14 mm in diameter is added to two steel micropumps, which in all other parameters and components share the same design as the micropumps presented in Core Publication [1]. With this approach, first insights towards the development of a micropump with a ∅15 mm outer diameter are gained. Based on the bending actuator model of *Herz et al.* [150], a reduction of the movable diaphragm diameter results in increased stiffness of the bending actuator. To further increase actuator force, stiffness, and, hence, micropump pressure build-up (see Section 2.1.3), the piezoceramic thickness is increased to 300 μm. The piezoceramic diameter is reduced to ∅11.7 mm, in proportion to the ∅14 mm movable actuator diaphragm. Figure 13a shows the welded steel micropump with reduced bending actuator diameter. During piezoceramic bonding via gluing, an electric field of $2\,^{\mathrm{kV}}/_{\mathrm{mm}}$ is applied to achieve a high electro-mechanical pretension for high

pump chamber volume. Figure 13b depicts the quasi-static deflection of the bending actuator under voltage load. The piezoelectric actuator exhibits a discernible hysteresis. Under quasi-static actuation between -0.4 to $1.5\,{}^{\mathrm{kV}}/_{\mathrm{mm}}$, the two micropumps show an actuator stroke of $(40.7 \pm 1)\,\mu$m. As no touchdown of the bending actuator to the pump chamber bottom is visible, the stroke measurement indicates successful achievement of a high pump chamber.

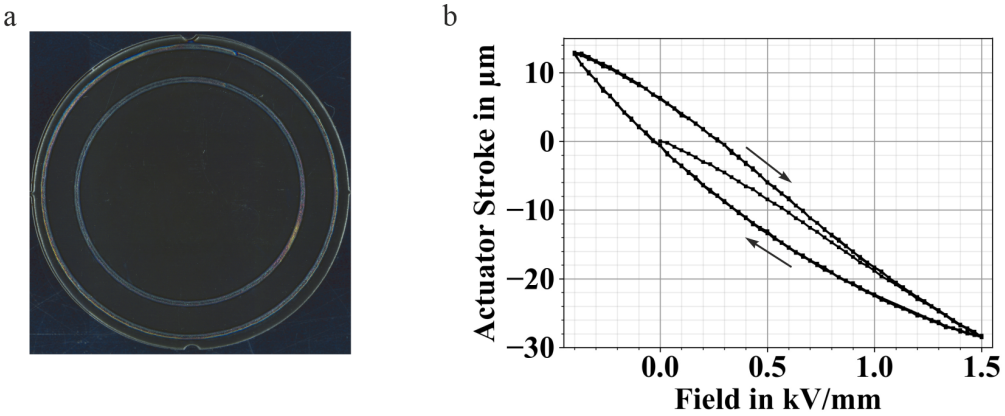

Figure 13: **a** Photograph of a steel micropump with a ∅14 mm pump chamber using ∅20 mm pump components. **b** Actuator stroke of a steel micropump with reduced actuator diameter, determined using white light interferometry.

The assembled micropumps are subsequently characterized for generated water flow rates, leakage, and pressure build-up using the methods described in Core Publication [1]. Figure 14a displays the generated water flow rate at 90 Hz sinusoidal actuation dependent on pressure applied to the micropump outlet. The extrapolated blocking pressure of the micropumps reaches a mean value of 130 kPa, verifying the assumed increase of pressure capability with increased bending actuator thickness. Micropump leakage rates at a backpressure of 5 kPa amount to $(47 \pm 13)\,{}^{\mu\mathrm{l}}/_{\mathrm{min}}$. These leakage rates are similar to the leakage data of the steel micropumps from Core Publication [1], which share the same microvalve design and laser welding configuration. Figure 14b shows the water flow rate under variation of the actuation frequency between 5 to 160 Hz without pressure applied at the pump outlet. The pumps achieve maximum water flow rates up to $(18 \pm 0.8)\,{}^{\mathrm{ml}}/_{\mathrm{min}}$, exceeding the water flow rates of the ∅20 mm micropumps of Core Publication [1]. The flow characteristic reveals a broad linear range. The ∅15 mm micropumps exhibit non-linear flow rate characteristics at frequencies above 140 Hz, whereas ∅20 mm pumps reach non-linearity after 30 Hz. In this non-linear flow regime, inertial effects impede further linear flow increase with increasing frequency. Due to increased actuator stiffness

and piezoceramic thickness, the ∅15 mm micropumps achieves higher forces to overcome fluidic resistances of highly dynamic flows. Another possible contribution to increased linear regime is reduced squeeze film damping. The latter describes thin layers of liquids and gases between two moving elements (or one moving element and a substrate), that exert damping of the mechanical movement due to viscous effects [202–204]. Due to the lateral reduction in pump chamber size, the outer regions of thin fluid layers with high distance to the valves are reduced. Therefore, the reduced pump chamber of the ∅15 mm micropumps may cause less squeeze film damping compared to the ∅20 mm micropumps, which leads to an increased linear flow regime. Further investigations of micropumps with reduced pump chamber size are needed to gain insights into possible contributing aspects of pump chamber fluid dynamics. While supplementary research is necessary, the analysis of these preliminary research samples shows a first feasibility of a metal micropump with ∅15 mm outer diameter. Based on these research findings, the next development step is further miniaturization to attain a ∅10 mm micropump. The leakage rates as a key attribute of the drug delivery system are investigated in detail in combination with the passive safety valve, see Section 3.2.

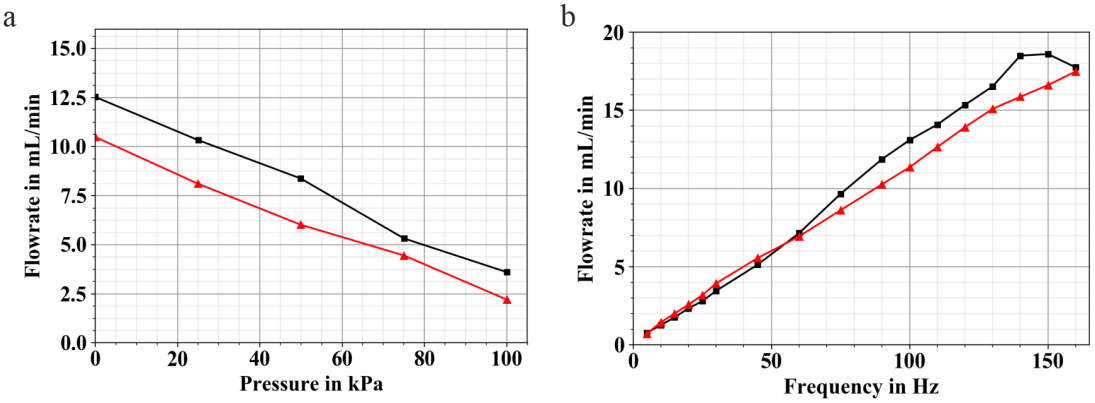

Figure 14: Water flow characteristics of two steel micropumps (red and black curve, respectively) with a pump chamber of 14 mm. **a** Backpressure capability with sinusoidal actuation of 90 Hz and −0.4 to 1.5 $^{kV}/_{mm}$, the extrapolated blocking pressure amounts to 130 kPa. **b** Frequency-dependent water flow rate with sinusoidal actuation from −0.4 to 1.5 $^{kV}/_{mm}$, without backpressure.

3.2 Passive Safety Valve

In this thesis, a passive microvalve based on the safety valve patent from *Richter et al.* [33] is designed, fabricated from AISI 304, and characterized. The metal safety valve serves as a safety measure and complements the micropump in an envisaged wearable drug delivery system. While an established desired drug flow defines the effectiveness of the system to promote patient health, the key attribute of the safety valve and micropump combination is the freeflow leakage in off-state: An indispensable requirement of the drug delivery system is to prevent potentially harmful, uncontrolled drug flow. To this end, the safety valve ensures tight closing of the fluid path in case of detrimental external pressure.

Core Publication [3] describes the working principle as well as fabrication and test of the safety valve. The isolated microvalve is studied to determine the opening pressure for comparison with the driving mechanism design presented in Section 2.1.3. The experimental evaluation of safety valve opening pressure shows deviation from the design value of 15 kPa. The experimentally derived opening pressure of 20 kPa is increased due to the insufficiently low manufacturing tolerances of the O-ring soft sealing, as the initial spring force of the actuator foil is highly dependent on h_{VS}. Another contributing factor to this deviation is thermal stress induced by the laser welding process (see Section 2.1.2).

The safety valve is combined with the ∅20 mm steel micropump to study the fluidic key and secondary attributes of the delivery system with water. The safety valve closes the fluid path, and the system achieves stable freeflow leakage rates of $(31.8 \pm 5)\,\mu\text{l}/\text{min}$ with inlet pressures up to 60 kPa. Additionally, the system exhibits a maximum generated flow rate of $(13.8 \pm 0.7)\,\text{ml}/\text{min}$ as its secondary attribute. Comparison to the generated flow rates of the micropump without safety valve shows that the fluidic resistance of the valve is low, and that the pump is well able to open the safety valve. The measurements confirm a well balanced, interdependent design of the safety valve's driving mechanism with the pressure capability of the micropump. Overall, the investigations provide proof of concept of the microvalve to act as a freeflow protection of the delivery system.

However, some safety valves exhibit malfunctioning with increasing fluid pressure at the inlet of the microvalve. In Core Publication [3], we present a fluidic FEM analysis which reveals that the flow through the valve induces an upwards directed movement of the O-ring. The moving soft sealing component obstructs the fluid path, therefore, further development of the passive safety valve mitigates this risk by omitting the O-ring.

To reduce the risk associated with a movable component within the valve chamber, the safety valves are designed and fabricated with a thin-film polymer coating that serves as a sealing material (see Section 2.1.4). Additionally, experimental characterizations of these safety valves in combination with a micropump are conducted analogously to Core Publication [3], and the findings are presented in [183]. Figure 15 depicts the freeflow leakage rates of the delivery system.

Microvalve failure in form of fluid path obstruction does not occur, hence, using a thin-film coating successfully mitigates this risk. However, freeflow leakage rates of the valves with Parylene-C coating at 20 kPa are increased by one order of magnitude compared to the safety valves with O-rings. Moreover, the freeflow leakage increases with pressure, as the safety valves fail to securely close the fluid path. It is evident that the plastic deformation of the actuator foil introduced by the manufacturing process (see Section 3.2) creates a permanent leakage path, resulting in insufficient valve performance. Hence, future fabrication of safety valves should follow the optimized manufacturing procedure for partial Parylene-C coatings (see Figure 11) to avoid plastic deformation of coated actuator foils.

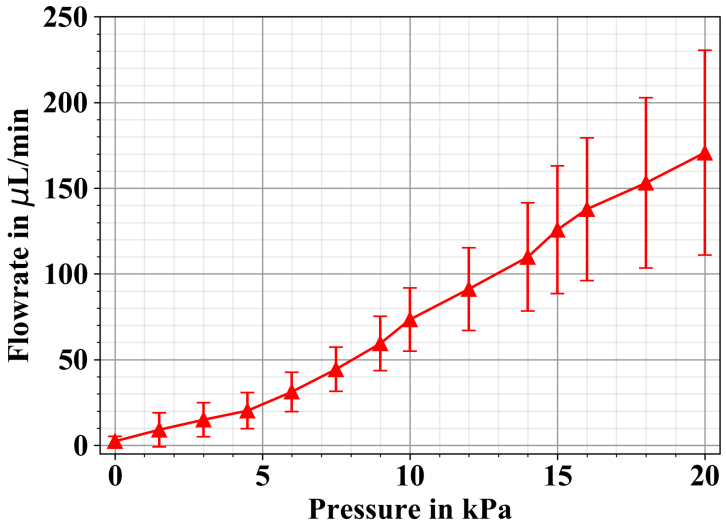

Figure 15: Freeflow leakage rates of a fluid delivery system comprising a micropump and a passive safety valve with a Parylene-C coated actuator foil, figure adapted from *Güntner* [183]. 10 safety valves with a 40 µm thick actuator foil and a 15 µm Parylene-C coating are designed and fabricated, while experimental characterization is contributed by *Güntner* [183].

While key attribute and reliability optimization are substantial, another desirable development goal for metal microfluidic MEMS is miniaturization (see Figure 4). In the context of the envisaged drug delivery system, a miniaturized pump and safety valve configuration reduces size and weight of the system worn by the patient. Hence, integration of the safety valve into the micropump foil stack ultimately promotes patient comfort. As initiation of this crucial development, a first concept of the safety valve integrated into the welded foils of a metal micropump is presented in Figure 16.

The concept of the integrated safety valve is based on a second metal foil stack that is welded onto the bottom of the rigid base of a micropump. As depicted in Figure 16a, the top half of this micropump is equivalent to the original design of the ∅20 mm micropump. Additional micromilled structures in the bottom half of the rigid base and a stack of three foils establish the safety valve functionality. In the CAD model depicted, a 200 μm thick foil partially covers the micromilled structures of the outlet path in the rigid base, and a thin safety valve foil covers the valve seat. Thereby, the fluid flowing through the opened safety valve is directed into the fluid path inside the rigid base towards the pump outlet. An additional foil with 50 μm thickness clamps the safety valve onto the 200 μm thick cover foil.

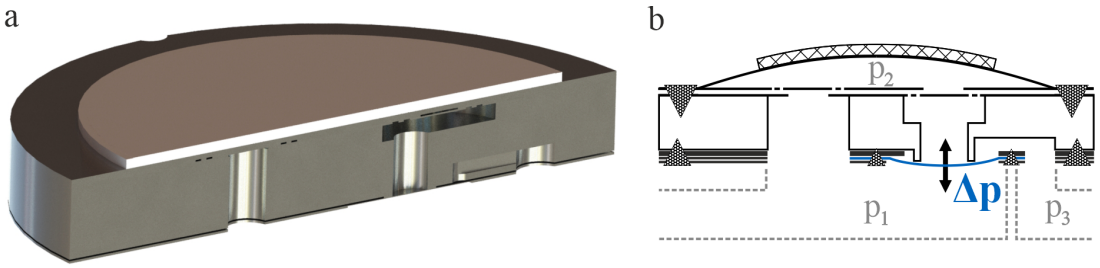

Figure 16: Design of a micropump with an integrated passive safety valve. This concept includes laser welding of metal foils to both sides of the rigid base. **a** CAD model of a piezomounted steel micropump with added safety valve functionality in the bottom foil stack. **b** Schematics of the structural design of the micropump with integrated freeflow protection. The safety valve foil fulfills its desired function depending on the pressure gradient.

Figure 16b shows the schematics of the pump with integrated freeflow protection. The cross-section illustrates the pressure-driven safety valve foil that operates analogously to the working principle presented in Core Publication [3], assuming $p_3 \leq p_1$. To allow this safety valve functionality, the reservoir pressure p_1 acts on the pump inlet as well as the safety valve foil. When operated, the micropump generates a pressure $p_2 > p_1$ such that the resulting pressure gradient opens the safety valve. Hence, a desired flow towards

a delivery target is created. When the pump is not operating and an external pressure $p_1 > p_2$ would force a freeflow through the micropump, the pressure gradient causes the safety valve foil to press down onto its valve seat, closing the fluid path.

Based on this concept, FEM simulations as presented in Section 2.1.3 are necessary for targeted design of the safety valve. Accounting for the pressure capability and bubble tolerance of the micropump, suitable foil thickness, diameter, as well as the valve seat height h_{VS} must be derived for apt spring characteristics of the safety valve. Moreover, adequate sealing as well as required surface qualities and contact pressures can be derived based on calculated leakage rates, using the analytical model presented in Core Publication [4]. As microjoining by laser welding induces material warpage of thin metal foils (see Section 2.1.2), fabrication of integrated safety valves may be challenging. Therefore, advancements in laser welding of thin metal foils are indispensable, and extensive DoE considering variations of process parameters may be necessary to achieve manufacturing feasibility. Subsequent to the fabrication of first research samples, experimental evaluations must involve freeflow leakage rate characterizations to efficiently advance the system's key attribute. Additionally, testing and optimization of secondary attributes such as generated flow rates and pressure capability contribute to the purposeful design of an effective and safe medical device.

3.3 Normally Closed Valve

The titanium NC valve is based on the patented working principle from *Wald et al.* [37]. Following this concept, I fabricate microvalves with micromilled plungers and bases, PCM structured foils, and an FKM O-ring sealing. To account for the requirements in the envisaged use within an hydraulic implant, the NC valves consist of titanium grade 5. The structural design, assembly process, and working principle of the titanium NC microvalve is thoroughly described in Core Publication [1].

Experimental evaluation of the first titanium NC valves provides a proof of concept, but also shows that the spring force and piezoelectric force are not balanced: The majority of NC valve samples fail to open under electric actuation. The bending actuator stroke of the 3 functional valves amounts to $(39.9 \pm 4.0)\,\mu$m. Further analysis of the actuator stroke characteristics provides insights into the interaction of the actuator and the suspended plunger. The observations reveal initial movement of the bending actuator without contact to the plunger. In the context of NC microvalve opening, this movement of about $15\,\mu$m diminishes the efficiency of the valve, as the piezoelectric actuation is not converted to plunger displacement. Hence, reduction of this contact-less regime becomes

an optimization goal for future NC microvalves. Functional NC microvalves presented in Core Publication [1] show low leakage rates of $(0.36 \pm 0.15)\,\mu\text{l}/\text{min}$ at a fluid pressure of 20 kPa. In microvalve open state, a fluid flow of $(9.0 \pm 9.5)\,\text{ml}/\text{min}$ is achieved. As described in Section 2.1.3, an FEM-guided failure analysis using *ANSYS Mechanical* is conducted to investigate the spring foil displacement under mechanical load. As high variations of O-ring chord size are found as the root cause for microvalve malfunction, the valve seat height h_{VS} is defined as a crucial parameter for NC microvalve functionality. The failure analysis findings enable optimization of NC microvalves as shown in the following.

To fabricate an NC microvalve with improved functionality, the valve foil spring force is adapted by optimizing the valve seat height. Prior to microjoining of the foil components to the rigid parts, the topology of the O-ring inserted into the notch of the NC microvalve base is analyzed. This approach allows careful selection of a soft sealing with suitable chord size to ultimately achieve the desired spring foil force, as well as azimuthal O-ring uniformity to avoid leakage paths. Following this approach, a fabricated titanium NC microvalve exhibits enhanced fluidic performance compared to the valves of Core Publication [1]. Figure 17 depicts the experimental results of the improved NC microvalve, obtained by using the same methods as described in Core Publication [1].

Piezoelectric actuation of the NC valve results in a total actuator movement of 65 μm (see Figure 17a). At approximately $0.5\,\text{kV}/\text{mm}$, the bending actuator performs a transversal movement of 35 μm until plunger contact is established. Despite this increase of ineffective movement, successful reduction of spring force of the valve foil is apparent in the displacement within the plunger contact regime. This observation is substantiated by subsequent fluidic characterization. In closed state, water leakage rates amount to $(0.03 \pm 0.02)\,\mu\text{l}/\text{min}$ over a range of 0 to 100 kPa. Improved sealing topology of a selected uniform O-ring further reduces leakage flow compared to NC valves of Core Publication [1]. As depicted in Figure 17b, a maximum flow of up to $34\,\text{ml}/\text{min}$ in open state is achieved at an inlet pressure of 20 kPa. In this optimized NC valve, the actuator force and spring foil restoration force are balanced such that the maximum open flow rate increases by a factor of 3.7 compared to the NC valves presented in Core Publication [1]. To substantiate these findings, more samples must be fabricated following this approach. Furthermore, adaption of the structural design may be necessary to reduce movement of the bending actuator prior to plunger contact for enhanced efficiency, as well as overall size reduction of the NC valve to attain a ⌀15 mm device.

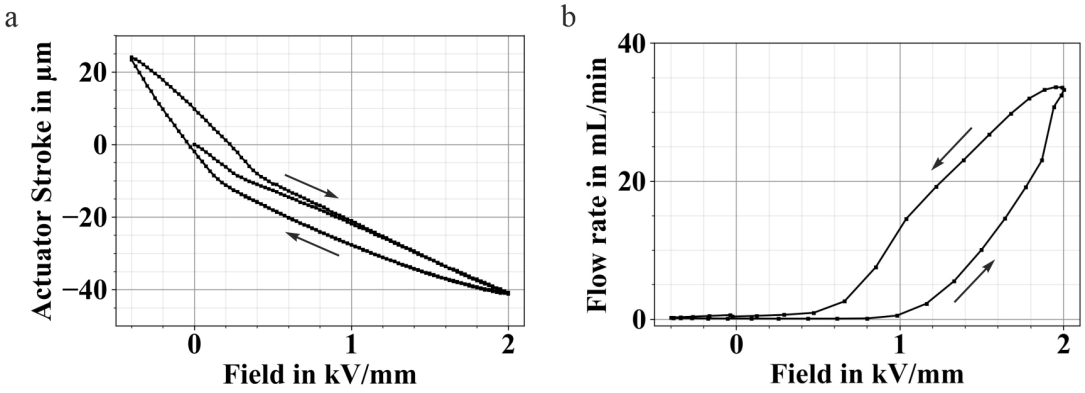

Figure 17: NC microvalve characteristics dependent on piezoelectric actuation. **a** Actuator stroke measurement of the adapted normally closed valve. A change in slope is visible at approximately 0.5 $^{\mathrm{kV}}/_{\mathrm{mm}}$, when the actuator diaphragm establishes contact to the plunger. **b** The microvalve optimization leads to an increase of the maximum open state flow rates at 20 kPa by a factor of 3.7 compared to the previous generation of NC valves presented in Core Publication [1].

3.4 Normally Open Valve

My work includes the original design, adapted manufacturing, and modified valve seat design of metal NO valves. In contrast to the working principle of the NC valve, a simple mechanism implements the valve functionality in the NO valve: a bending actuator presses down on a valve seat to close the fluid path, whereas fluid flow is allowed while the valve is not actuated. Thereby, the NO valve is an important addition to the metal microfluidic MEMS platform, as certain safety considerations necessitate this default state of a microvalve in a medical microfluidic system (see Section 2.2).

In addition to first fabricated NO valves showing feasibility of the concept, several further development steps demonstrate design measures towards increased reliability and safety. Core Publications [1], [2], and [4] present these development efforts in detail, along with the research findings of experimental microvalve characterization.

As part of a titanium based microfluidic platform for hydraulic implants, I present the NO microvalve and its design in Core Publication [1]. This initial design comprises a micromilled base from titanium grade 5 to meet requirements specific to implantable applications, an actuator foil structured via PCM, and an FKM O-ring. Manufacturing of the bending actuator of these first NO valves involves a electro-mechanical pretension during glue curing (see Section 2.1.3) based on the valve seat height h_{VS} derived from

the nominal O-ring dimensions. Hence, the voltage load for electro-mechanical pretension is not optimized for the 24 fabricated NO microvalves. Experimental characterization of the NO valves successfully demonstrate functionality of the device. The valves achieve high open state flow rates of $(27.5 \pm 5.3)\,{}^{\mathrm{ml}}/_{\mathrm{min}}$ and good closed state performance, but the leakage rates of $(10.9 \pm 28.1)\,{}^{\mu\mathrm{l}}/_{\mathrm{min}}$ exhibit high variation. As characterizations of the O-rings show, high manufacturing deviations of the O-ring chord size lead to varying values of h_{VS} (see Section 2.1.4). As a result, optimal balance of high contact pressure to default valve opening is not achieved, as the bending actuator position relative to h_{VS} varies likewise. Moreover, additional experiments subsequent to the characterizations in Core Publication [1] reveal material defects of the piezoceramic. Non-uniform preforming of the disk after bonding induces fracture of the piezoceramic during further NO valve operation. To accomplish performance and material stability, I adapt the electro-mechanical pretension process.

The relationship of h_{VS} and electro-mechanical pretension is addressed in a comprehensive experimental study, presented in Core Publication [2]. A linear relationship of the pretension voltage V_p to the height of the protruding O-ring h_{VS} is assumed, and an empirical factor c is introduced, such that $V_p = c \cdot h_{VS}$. Furthermore, the risk of material defects by reducing the pressing force in the piezoceramic bonding process is reduced. This approach is pursued for a total number of 52 valves in three groups with different sealing materials and nominal chord sizes to verify the proposed process. Evaluations of all manufactured NO valves show successful reduction of leakage rate standard deviation by 52 %, with an overall leakage rate performance of $(13 \pm 13.4)\,{}^{\mu\mathrm{l}}/_{\mathrm{min}}$. Worthy of remark are the significantly low leakage rates of $(7.5 \pm 1.4)\,{}^{\mu\mathrm{l}}/_{\mathrm{min}}$ achieved by NO valves comprising EPDM O-rings with $600\,\mu$m nominal chord size. Additionally, fatigue tests (see Section 2.3) of the NO valves verify increased stability of both material and fluidic performance after a total of $1 \cdot 10^6$ actuation cycles. While the study confirms applicability of the proposed process, high effort is necessary to fabricate the NO valves with individual characterization of h_{VS}. Therefore, I design NO microvalves to achieve high manufacturing accuracy of the valve seat structure.

In Core Publication [4], I present further development of the NO microvalve incorporating a design without soft sealing. It represents a crucial development step, as all medical devices necessitate careful risk analysis and appropriate risk mitigation. The introduced trench design induces several effects leading to leakage rate reduction, including increased contact pressure and sealing surface, as well as fluidic effects in the confined fluid in

the trenches. To acquire proof of concept of the valve seat design, the NO valve with concentric trenches is manufactured from AISI 303 steel as a less cost-intensive alternative to titanium grade 5. In contrast to the AISI 304 material used for steel micropumps and passive safety valves, a different alloy is used to achieve better machinability (see Section 2.1) and higher accuracy of the 100 μm wide trenches (see Section 2.1.1). Despite higher effort in microstructuring, the optimized valve seat structure promotes cost reduction as valve seat characterization of each protruding O-ring is no longer required. As additional optimization measures, I fabricate NO valves with a Parylene-C coating serving as a sealing (see Section 2.1.4) as well as valves with bending actuators capable of achieving higher forces (see Section 2.1.3). In-depth analysis of leakage rates in closed state are conducted via analytical modeling, contributed by *Maier*, to build knowledge on surface quality and contact pressure contributions to leakage flow. The effects of trench design parameters on fluidic resistance in open state are studied via fluidic FEM simulations by *Hölzl*.

The experimental evaluation of the NO microvalves shows that using a micromilled valve seat achieves good sealing performance similar to NO valves with O-ring sealings. The NO valves exhibit low fluidic resistance and high manufacturing accuracy compared to the movable O-ring. Further improvements of valve tightness by increased contact force or surface coating cannot be shown, as low sample quantity leads to insufficient statistics. However, fatigue tests indicate improved stability of the piezoceramic by increasing bending actuator thickness, and enhanced performance stability in closed state with additional coating.

While the feasibility of a micromilled trench design serving as a valve seat is successfully shown, the use of steel as a base material results in complexity of the fabrication of the bending actuator. The dissimilarity of the thermal expansion coefficient of steel and PZT result in thermal pretension of the bending actuator (see Section 2.1.3). This thermal pretension is not adjustable to account for design considerations, as the piezoceramic bonding temperature is fixed. Here, electro-mechanical pretension is not required to create the NO default state of the microvalve, as the thermal pretension leads to a high bending actuator position relative to the valve seat. Hence, contact to the valve seat is established at high electric fields, while the driving mechanism holds potential for a shift towards higher contact pressure and slightly reduced open state flow rates.

Therefore, optimization and further development of the NO valve with concentric valve seat trenches must include reduction of initial bending actuator distance to the valve seat. Since process parameters of the piezoceramic bonding process may not be adapted,

modifications of the valve seat design or the welding process can be considered for improvements of the steel NO microvalve. The design of the rigid valve base may be changed to include an elevated valve seat. Mitigations of foil warpage due to laser welding (see Section 2.1.2) may reduce the stress within the actuator foil, resulting in a lower bending actuator position.

As the envisaged application of the NO valve is a hydraulic implant, it is necessary to fabricate future research samples from titanium grade 5 to gain early insights into the feasibility of the trench design. Thermal pretension is only a minor contributor to bending actuator pretension for the titanium-based microfluidic MEMS of this platform, hence, this material choice may result in improvement of the driving mechanism.

Further design considerations of the NO valve sealing structure may include a structured part of the actuator foil on the side that faces the valve chamber. The structure may be created such that in closed state, the actuator foil and rigid base structures interlace to form a tight maze sealing. Such an interlacing design may be realized by PCM structured trenches in the actuator foil, complementary to elevated valve seat rings with micromilled trenches in the rigid base. Moreover, miniaturization of the NO valve to an outer diameter of $\varnothing 15\,\mathrm{mm}$ is an important development goal to attain size reduction of the overall envisaged implant.

4 Publication Summaries

Core publication [1]:
Piezoelectric titanium based microfluidic pump and valves for implantable medical applications

published by A. B. Bußmann* and C. P. Durasiewicz*, S. H. A. Kibler, and C. K. Wald *in* Sensors and Actuators A: Physical, p. 112649, 2021

*A. B. Bußmann and C. P. Durasiewicz contributed equally.

This publication presents the design, working principle, and experimental performance data of three titanium based microfluidic devices: a micro diaphragm pump, an NO microvalve, and an NC microvalve. The intended use of these devices is an implantable hydraulic microfluidic system for urological applications. The paper presents the successful manufacturing and test of the titanium microfluidic MEMS, and provides a detailed analysis of key and secondary attributes of the introduced pump and valves. All three devices share a similar design of their titanium base, are manufactured using the same processes, and comprise the same type of PZT actuator disk. Therefore, the established titanium microfluidic MEMS platform is suitable for hermetic integration into a fully implantable, MRI and biocompatible system.

Characterizations of key attributes include achieved water flow rates and pressure build-up of the diaphragm micropumps and water leakage rates in closed state of microvalves. We study micropump backflow leakage and microvalve water flow in open state as secondary attributes, respectively. Lastly, the paper focuses on each microfluidic device in a specific detail: We discuss the effects of material change in our pumps from stainless steel to titanium, investigate early fatigue indications in a small study of NO valves, and conduct a failure analysis of NC valves including FEM simulations.

The experimentally evaluated performance of titanium micropumps is compared to stainless steel micropumps based on a group of $n = 24$ each. Results show similarly high flow rate and pressure build-up performances, while backflow leakage measurements

reveal large scattering. As possible root cause for leakage deviations, we suspect thermal impacts of the laser welding, inducing material stresses in the valve foils. In a detailed discussion, we conclude that the small difference in the Young's moduli of steel and titanium does not affect the micropump characteristics of both groups, as other factors dominate, such as the deviations of piezoceramic material or changes in the fluidic periphery.

Our microvalve characterizations show feasibility of both NO and NC microvalve type. In closed state, we observe low leakage rates at the operating pressure of the envisaged application. The $n = 24$ NO valves exhibit high flow rates in open state as their secondary attribute and $n = 2$ valves show divergent indications of fatigue after $1 \cdot 10^6$ actuation cycles. The majority of manufactured NC microvalves fail to operate in open state. With dedicated failure analysis, we identify that material deviations of the O-ring soft sealing affect critical design parameters of the NC valve. The insufficient manufacturing accuracy of the O-rings also influences the performance of NO valves, as leakage rate evaluations reveal high sample-to-sample variation. The obtained deep understanding lays the basis for the development of improved microvalves.

This paper summarizes the successful work on a micropump design transfer from stainless steel to a high strength titanium alloy, as well as two novel microvalves of NO and NC type. It builds the foundation for further improvements of the metal micropump, as well as NO and NC microvalve development.

Individual contributions:
My contribution to this work includes the original design of the NO valve, manufacturing and experimental characterization of all titanium micropumps and microvalves, as well as FEM simulations and failure analysis. I analyzed and curated the acquired data, identified crucial influencing parameters and drew conclusions for further developments. Overall, I planned and executed the research activity of the titanium microfluidic devices, authored, revised, and edited the manuscript.

My colleague A. B. Bußmann planned and executed the experimental research of the steel micropumps and analyzed the data of both titanium and steel micropumps in detail. Additionally, manuscript conceptualization, authoring, review and editing of the manuscript were contributed by A. B. Bußmann. S. H. A. Kibler and C. K. Wald originally designed the NC valve and the stainless steel micropump, respectively, and both contributed by funding acquisition, supervision of the research, as well as manuscript review and editing.

Core publication [2]:
Piezoceramic mounting process and adapted pretension for improved microvalve functionality and reliability

published by C. P. Durasiewicz, S. T. Güntner, and S. H. A. Kibler *in* Proceedings of MikroSystemTechnik Kongress 2021, Stuttgart-Ludwigsburg, 08.-10. Nov. 2021, ISBN 978-3-8007-5656-8, VDE e.V. (Hrsg.)

In this publication, the NO microvalve is further developed for improved fluidic performance and increased reliability of the piezoceramic actuator. In Core Publication [1], we identify the insufficiently low manufacturing precision of the O-ring soft sealing as the root cause for large scattering of leakage rate data of NO valves. Furthermore, analysis of the valves reveal material failures of the piezoceramic disk, such as non-uniform preforming and fracturing after NO valve operation. To address these problems linked to the varying valve seat height h_{VS} of NO valves, we adapt the bonding process for manufacturing of the piezoelectric bending actuator within an experimental approach.

Firstly, the maximal pressing force on the piezoceramic during glue curing is reduced to 5 N to prevent material failure of the piezoceramic caused by excessive bending over the O-ring. Secondly, the voltage load during glue curing for electro-mechanical pretension (see Section 2.1.3) is adapted respective to the measured valve seat height h_{VS} of each valve. An empirically derived pretension factor c (here: $c = 1.6$) is implemented such that the resulting bending actuator position respective to h_{VS} ensures optimized closing of the valve, while allowing open state flow rates in the range of $^{\mathrm{ml}}/_{\mathrm{min}}$. Following this approach, the voltage load V_P for electro-mechanical pretension is calculated as a function of the measured valve seat height: $V_P = c \cdot h_{VS}$.

To verify the applicability of the proposed process to a broad range of h_{VS}, we conduct a comparative study of three groups of NO valves. In an extensive DoE, we vary the valve seat height and sealing material across a total of $n = 52$ titanium NO valves. The first group resembles the design of NO valves of Core Publication [1], as they comprise the same type of FKM O-rings with a nominal chord size of 500 μm. The second group incorporates an O-ring made of EPDM and 600 μm nominal chord size. The third group of NO valves is build without O-rings, hence, they are assembled without electro-mechanical pretension of the bending actuator, as $h_{VS} = 0$.

Experimental evaluation of all fabricated microvalves shows significant reduction of leakage rate data scattering with adapted pretension compared to the NO valves of Core Publication [1]: The standard deviation of water leakage at 20 kPa is reduced

from 28.1 $\mu l/min$ to 13.4 $\mu l/min$ as a result of the adapted electro-mechanical pretension. Exceptionally low leakage rates of $(7.5 \pm 1.4)\,\mu l/min$ are attained by NO valves comprising EPDM O-rings. Actuator stroke characteristics of the three groups deviate due to different hyperelastic behavior of the respective rubber materials and the omitted electro-mechanical pretension, respectively. In addition to fluidic characterization after fabrication, we subject NO valves of each type to a fatigue test. All microvalves show both material and sealing performance stability after $1 \cdot 10^6$ actuation cycles, which further demonstrates the improved robustness resulting from the proposed fabrication process.

The work presented in Core Publication [2] demonstrates successful device optimization by adapting the NO microvalve fabrication process. The proposed piezoceramic bonding procedure ensures similar leakage rate performance and reliable piezoelectric actuation of NO valves. The developments of NO valves presented in Core Publication [4] build on the insights gained by analysis of NO valves without O-rings.

Individual contributions:
My contributions to this publication involved the design of the overall research activity including the proposed manufacturing process and DoE, the fabrication of the tested titanium microvalves, as well as planning and supervision of the mechanical and fluidic characterizations. Additionally, I performed all fatigue tests, analyzed and curated all acquired data and derived the research findings. I conceptualized, authored, and edited the manuscript.

S. T. Güntner performed mechanical and fluidic experiments under my supervision, and S. H. A. Kibler contributed by funding acquisition as well as manuscript review and editing.

Core publication [3]:
'Safety Valve': A metal-based, self-securing switchable microvalve for medical applications

published by C. P. Durasiewicz, W. Hölzl, and G. Schrag *in* Proceedings of MikroSystem-Technik Kongress 2021, Stuttgart-Ludwigsburg, 08.-10. Nov. 2021, ISBN 978-3-8007-5656-8, VDE e.V. (Hrsg.)

In this study, we present the passive microvalve, the so-called 'safety valve', to control the flow path of a microfluidic drug dosing system, and characterize fabricated samples to gain proof of principle. We present the design of the self-securing switchable microvalve for medical applications, describe its working principle, and fabricate the valve from stainless steel. Based on observations of microvalves in a detected failure state, dedicated FEM simulations provide insights into fluidic phenomena, paving the path to further device optimization.

The working principle of the safety valve bases on its specific three fluid port design. The pressures present at the control port p_1 and the inlet port p_2 induce switching of the valve between fail-safe (closed) state and delivery (open) state. As described in Section 2.1.3, the actuator foil of the safety valve experiences a certain spring load due to the elevated valve seat. Therefore, fluid flow, i.e. uncontrolled drug release, is prevented from the outlet port p_3 if $p_1 + p_{spring} > p_2$.

In our study, we fabricate and subsequently characterize safety valves for open state water flow rates and fluidic resistance. The pressure dependent flow characteristics show that valve opening takes place at a differential pressure of $p_2 - p_1 = \Delta p = 20\,\mathrm{kPa}$ instead of the designed target value of $p_{spring} = 15\,\mathrm{kPa}$. Moreover, open state flow data exhibits large scattering due to high variation of the spring load of the actuator foil, which indicates poor manufacturing accuracy of the O-ring soft sealing. Of the $n = 12$ tested safety valves, we observe a flow-induced increase of fluidic resistance in five samples leading to flow path obstruction. We investigate the observed flow path obstruction by conducting dedicated FEM simulations of the flow through the microvalve for failure analysis. The simulations reveal flow-induced movement of the O-ring soft sealing as root cause for this malfunctioning.

In addition to characterizations of the individual safety valves, we create a microfluidic delivery system by combining a piezoelectric steel micropump with the safety valve. We analyze the delivery system in fail-safe state and evaluate the key attribute of the system: we observe freeflow leakage rates of $(31.8 \pm 5)\,{}^{\mu\mathrm{l}}/_{\mathrm{min}}$ in a pressure range of up to 60 kPa.

Additionally, we characterize the fluidic system in delivery state for its secondary attribute, the delivered water flow rate, and find a maximum of $(13.8 \pm 0.7)\,{}^{\mathrm{ml}}/_{\mathrm{min}}$.

The research findings provide proof of principle of the metal-based safety valve, as passive microvalves are successfully tested in delivery state and fail-safe state when combined with the piezoelectric micropump. The failure analysis of microvalves with flow-induced flow obstruction reveals fluid-structure-interactions of the O-ring soft sealing with the fluid flow through the valve. The gained insights of occurring flow phenomena lay the basis for a deeper understanding of the functionality of the component.

Individual contributions:
I contributed to this work by planning of the overall research activity, original design of the passive microvalve, as well as fabrication and experimental characterization of the microvalves. Moreover, I analyzed and curated all experimentally acquired data and drew conclusions on device performance and failure analysis. I conceptualized, authored, and edited the manuscript.

W. Hölzl performed the FEM simulations, curated and analyzed all numerically derived data, as well as authored and edited the manuscript. G. Schrag contributed by funding acquisition, manuscript review and editing, as well as supervision of the research.

Core publication [4]:
Piezoelectric Normally Open Microvalve with Multiple Valve Seat Trenches for Medical Applications

published by C. P. Durasiewicz, S. T. Güntner, P. K. Maier, W. Hölzl, and G. Schrag *in* Applied Sciences, vol. 2021, no. 11, p. 9252

This work describes the development of an NO microvalve without soft sealing to increase device reliability. The research findings presented in Core Publications [2] and [3] suggest that while low leakage rates are achieved, an O-ring soft sealing poses multiple risks to microvalve manufacturing, piezoceramic material stability, and device functionality. To reduce the design complexity of the device, we omit the additional component of the NO microvalve and introduce a valve seat with concentric trenches that are micromilled into the rigid base. In this study, we extensively investigate the valve seat design parameters in a fluidic FEM analysis, derive an analytical model for leakage rates in closed state, as well as fabricate and test the microvalve with micromilled valve seat trenches. Moreover, we pursue multiple approaches to further reduce leakage rates, such as additional coating of the valve seat and increased actuator force.

In our study, we design a metal NO microvalve with concentric trenches serving as a valve seat, similar to microvalves presented in research for low leakage gas applications. In addition to experimental investigation, we conduct an extensive parameter study using fluidic 3D finite element simulations to analyze the influence of trench width and depth on the fluidic resistance of the valve. Moreover, we derive an analytical leakage rate model that includes considerations of contact mechanics to model the leakage path in the interface of metal foil and the valve seat. Thereby, we calculate the leakage rates through the microvalve with concentric trenches in dependence of the fluid pressure as well as surface qualities and compression force exerted by the piezoelectric bending actuator.

We fabricate a total of $n = 25$ microvalves with a concentric trench design micromilled into the rigid base. The microvalve base material chosen in this feasibility study is stainless steel as a less cost-intensive choice compared to titanium grade 5. To investigate further leakage rate reduction measures, we fabricate $n = 10$ of these valves with an additional Parylene-C coating on the valve trenches. Other $n = 5$ valves comprise a piezoelectric bending actuator capable of exerting higher compression forces, that we design based on the model of *Herz et al.*[150] (see Section 2.1.3). We conduct experimental evaluations of electro-mechanical characteristics, fluidic key and secondary attributes, as well as performance after fatigue testing analogously to Core Publication [2].

Actuator stroke measurements show that the NO valve without O-ring exhibits discernible regimes of open and closed state. Microvalve open state characterizations reveal an open flow range of up to 120 $^{\mathrm{ml}}/_{\mathrm{min}}$ at an inlet pressure of 100 kPa. The key attribute of the microvalves, the leakage rates in closed state, are similar to leakage rates of valves with O-rings presented in Core Publications [1] and [2]. With leakage rate values in the range of 20 to 25 $^{\mu\mathrm{l}}/_{\mathrm{min}}$ at a pressure of 20 kPa, we successfully demonstrate that the trench design is an adequate, risk reducing alternative to the O-ring soft sealing to enable good sealing abilities of an NO microvalve. Comparing the leakage rates of the three investigated NO valve designs, no significant differences between the groups could be found. We are able to estimate the leakage rates of our NO valves with our analytical model with some overestimation of the experimentally collected data.

Fatigue tests of the microvalves involve operation up to a total of $1 \cdot 10^6$ actuation cycles and subsequent evaluation of performances. The fatigue analysis reveals enhanced leakage rate stability by Parylene-C coating or increased piezoelectric actuator force. Moreover, the findings of this investigation indicate increased piezoceramic material stability with increased thickness.

The work presented in this publication demonstrates the suitability of our proposed trench design to create an NO microvalve without an additional soft sealing component. With this demonstrated risk mitigation measure and the gained insights of 3D fluid simulations as well as analytical modeling, we pave the path for further designs of safe and reliable metal microvalves for medical applications.

Individual contributions:
My contribution to this work include overall research activity planning, original design of the microstructured valve seat design, as well as the fabrication of the microvalves. I performed fatigue tests of the NO valves, analyzed and curated all experimentally acquired data, and drew conclusions to the research findings. Additionally, I supervised the work of S. T. Güntner and P. K. Maier. I conceptualized, authored, and edited the manuscript.

S. T. Güntner performed CAD design of the microstructured valve seat as well as mechanical and fluidic experiments under my supervision. P. K. Maier derived the analytical leakage rate model, experimentally acquired surface roughness data, and authored and edited the manuscript. W. Hölzl performed the FEM simulations, curated and analyzed all numerically derived data, as well as authored and edited the manuscript. G. Schrag contributed by manuscript conceptualization, review, and editing, as well as supervision of the research.

5 Summary and Outlook

This thesis develops a versatile metal microfluidic MEMS platform for wearable and implantable medical applications. It addresses the need for efficient, reliable microfluidic devices to allow treatment of diseases that lack apt solutions to date. The metal-based technology platform readily fulfills many requirements specific to medical use. The used processing technologies add to these advantages as they offer hermetic welding as well as economic small and medium lot size production. The developed metal micropumps and microvalves exhibit diverse functionalities for flow generation or flow path control. Combination of these MEMS devices enables versatile creation of medical microfluidic systems to attain treatment-specific functionality. Thereby, the established metal MEMS platform as well as the acquired design knowledge make valuable contributions towards the development of miniaturized, effective medical devices.

The identified microfluidic and technological challenges are used to derive development goals for the metal microfluidic MEMS. The goals pursued by the developments of this work are backpressure and flow rate of a micropump, freeflow prevention of a passive safety valve, leakage rates of NC and NO microvalves, as well as miniaturization. To purposefully achieve these characteristics, design considerations involve material properties, structural design, and fabrication processes of metal microfluidic MEMS. To this end, a comprehensive overview of microstructuring of the rigid and foil-based metal components, their microjoining process, the MEMS driving mechanism, as well as sealing structures and elements are provided. Through literature review, numerical simulations, as well as experimental and analytical analyses, crucial knowledge on influencing parameters in metal microfluidic MEMS design and feasible process technologies is built.

Based on these established methods, the metal microfluidic MEMS are designed, fabricated, and characterized to confirm the advancements of mechanical and fluidic characteristics. The main research efforts of micropump, passive safety valve, NO and NC microvalve development are presented in Core Publications [1], [2], [3], and [4], while some so far unpublished research is firstly reported in this thesis.

The micropump developments of this work show suitability of the metal micropumps to meet the requirements of medical applications. The research on titanium grade 5 pumps confirms the applicability of the MRI and biocompatible material to achieve high force actuation and ensure high yield strength. The ∅20 mm metal micropumps exhibit high water flow rates, good backpressure capabilities, as well as energy efficiency. Additionally, the ∅15 mm steel micropump advances these fluidic key performances along with favorable miniaturization.

To ensure freeflow protection of a microfluidic system for drug delivery, a metal-based safety valve is firstly realized based on the patented concept of a pressure-driven microvalve from *Richter et al.* Characterizations of fabricated research samples comprising an FKM O-ring soft sealing provide proof of concept and show good fluidic performance. As some safety valves with O-ring exhibit malfunctioning due to detrimental flow effects, microvalves are fabricated comprising a Parylene-C coating that successfully mitigates this failure state. Nevertheless, the coated design fails to establish improved leakage rate performance. With the proposed improved fabrication of the Parylene-C coating, future research may pursue the presented concept of safety valve integration into the micropump.

Similarly, the NC microvalve is fabricated based on the patented structural design from *Wald et al.* and the feasibility of the working principle is verified. However, microvalve failure occurs in several research samples. Subsequent failure analysis of the NC valve involving numerical simulation of the spring foil component reveals high manufacturing deviations as root cause for microvalve malfunctioning. Based on the gained insights of influencing parameters, the spring foil characteristics of the NC microvalve are optimized and high fluidic performance in both open and closed state is shown.

Lastly, the piezoelectric NO microvalve is developed further in various development steps to advance the reliability of the device by design and improved manufacturing. The first fabricated research samples base on my original design and exhibit good fluidic performance, while sample-to-sample variation of leakage rates and induced piezoceramic material failure necessitate device optimization. NO valve advancement is demonstrated by improved fabrication of the piezoceramic bending actuator, leading to high performance stability over device lifetime. To further reduce the risk of microvalve malfunction, the movable sealing component is omitted. A sophisticated valve seat design with micromilled trenches is realized, capable of good leakage rate performance similar to NO valves with O-rings. Additional design measures such as increased actuator force and a Parylene-C coating are successfully implemented using apt manufacturing processes. Experimental

evaluations indicate improvement of piezoceramic material and leakage rate stability as a result of these added design features, respectively.

In conclusion, I successfully create and advance a metal-based microfluidic platform for medical applications as a result of my devoted research efforts. The micropumps and microvalves exhibit distinctive functionalities that contribute to the adaptability of the technology platform for effective and reliable medical devices. Based on the fluidic performance, the elementary advantages in system integration and manufacturability, as well as acquired design knowledge, the metal microfluidic MEMS platform is well suitable to promote patient well-being as part of active medical devices.

Outlook

While this work shows feasibility and advancements of micropumps and microvalves, further optimization potentials of the devices remain. Based on the research efforts presented, future developments can promote performance and miniaturization. Soft sealings with reliable adherence to the metal substrate and high manufacturing accuracy are substantial for microvalve developments. Additionally, increased force generation of the piezoelectric bending actuator can be achieved using multilayer actuators [205, 206], which may be used to improve performance of the metal pumps and valves. However, the largest impact on overall optimization of the metal-based technology platform stems from an improved microjoining process.

By reducing the heat impact and consequential foil warpage due to laser welding, significant increase of leakage rate performance can be achieved. Advancements of the laser welding process can be substantial to enable the safety valve functionality in the envisaged integration into the micropump foil stack. Moreover, reduction of the initial gap height h_{IG} of the micropump can further improve fluidic performance of the device. It may likewise be a crucial prerequisite to further miniaturization, as the heat impact defines the minimal distance of the weld seam to the valve structures. Another optimization aspect of the microjoining process is the material tension within the metal foils that alters the foil stiffness as a result of the thermal load. Both process adaption as well as analytical models of the occurring effect promote further device developments.

Utilizing the presented knowledge combined with advancements of the microjoining process, further miniaturization of the metal microfluidic MEMS are achievable. With reduced size and weight of pumps and valves, developments may target applications with strict space requirements, will further improve patient comfort, and enable the creation of more complex fluidic systems.

Bibliography

[1] A. B. Bußmann, C. P. Durasiewicz, S. H. A. Kibler, and C. K. Wald, "Piezoelectric titanium based microfluidic pump and valves for implantable medical applications," *Sensors and Actuators A: Physical*, p. 112649, 2021.

[2] C. P. Durasiewicz, S. T. Güntner, and S. H. A. Kibler, "Piezoceramic mounting process and adapted pretension for improved microvalve functionality and reliability," *Proceedings of MikroSystemTechnik Kongress 2021, Stuttgart-Ludwigburg, 08.-10. November 2021*, no. ISBN 978-3-8007-5656-8, VDE e.V. (Hrsg.).

[3] C. P. Durasiewicz, W. Hölzl, and G. Schrag, "'Safety Valve': A metal-based, self-securing switchable microvalve for medical applications," *Proceedings of MikroSystemTechnik Kongress 2021, Stuttgart-Ludwigburg, 08.-10. November 2021*, no. ISBN 978-3-8007-5656-8, VDE e.V. (Hrsg.).

[4] C. P. Durasiewicz, S. T. Güntner, P. K. Maier, W. Hölzl, and G. Schrag, "Piezoelectric normally open microvalve with multiple valve seat trenches for medical applications," *Applied Sciences*, no. 11, p. 9252, 2021.

[5] D. F. Williams, "On the mechanisms of biocompatibility," *Biomaterials*, vol. 29, no. 20, pp. 2941–2953, 2008.

[6] J. G. Smits, "Piezoelectric micropump with three valves working peristaltically," *Proceedings of the 5th International Conference on Solid-State Sensors and Actuators and Eurosensors III*, vol. 21, no. 1, pp. 203–206, 1990.

[7] M. K. Mishra, V. Dubey, P. M. Mishra, and I. Khan, "MEMS technology: A review," *Journal of Engineering Research and Reports*, pp. 1–24, 2019.

[8] Y.-H. Joung, "Development of implantable medical devices: from an engineering perspective," *International neurourology journal*, vol. 17, no. 3, pp. 98–106, 2013.

[9] R. Rapp, Schomburg, W. K. Schomburg, j. Schulz, and W. Stark, "Liga micropump for gases and liquids," *Sensors and Actuators A: Physical*, vol. 40, no. 1, pp. 57–61, 1994.

[10] K. Nakahara, M. Yamamoto, Y. Okayama, K. Yoshimura, K. Fukagata, and N. Miki, "A peristaltic micropump using traveling waves on a polymer membrane," *Journal of Micromechanics and Microengineering*, vol. 23, no. 8, p. 085024, 2013.

[11] G. Liu, C. Shen, Z. Yang, X. Cai, and H. Zhang, "A disposable piezoelectric micropump with high performance for closed-loop insulin therapy system," *Sensors and Actuators A: Physical*, vol. 163, no. 1, pp. 291–296, 2010.

[12] A. G. Demir, B. Previtali, and M. Bestetti, "Microvalve actuation with wettability conversion through darkness/UV application," *Journal of Micromechanics and Microengineering*, vol. 21, no. 2, p. 025019, 2011.

[13] C.-H. Cheng and Y.-P. Tseng, "Characteristic studies of the piezoelectrically actuated micropump with check valve," *Microsystem Technologies*, vol. 19, no. 11, pp. 1707–1715, 2013.

[14] A. Pradeep, V. R. S., J. Stanley, B. G. Nair, and T. S. Babu, "Automated and programmable electromagnetically actuated valves for microfluidic applications," *Sensors and Actuators A: Physical*, vol. 283, pp. 79–86, 2018.

[15] A.-L. Zhang, Y.-W. Cai, Y. Xu, and W.-Y. Liu, "A new ball check valve based on surface acoustic wave," *Ferroelectrics*, vol. 540, no. 1, pp. 138–144, 2019.

[16] S. Svensson, G. Sharma, S. Ogden, K. Hjort, and L. Klintberg, "High-pressure peristaltic membrane micropump with temperature control," *Journal of Microelectromechanical Systems*, vol. 19, no. 6, pp. 1462–1469, 2010.

[17] G. Sharma, S. Svensson, S. Ogden, L. Klintberg, and K. Hjort, "High-pressure stainless steel active membrane microvalves," *Journal of Micromechanics and Microengineering*, vol. 21, no. 7, p. 075010, 2011.

[18] D. J. Laser and J. G. Santiago, "A review of micropumps," *Journal of Micromechanics and Microengineering*, vol. 14, no. 6, pp. R35–R64, 2004.

[19] S. Mohith, P. Navin Karanth, and S. M. Kulkarni, "Recent trends in mechanical micropumps and their applications: A review," *Mechatronics*, vol. 60, pp. 34–55, 2019.

[20] F. Abhari, H. Jaafar, N. A. M. Yunus, "A comprehensive study of micropumps technologies," *International Journal of Electrochemical Science*, no. 9765 - 9780, Vol. 7, 2012.

[21] N.-T. Nguyen, X. Huang, and T. K. Chuan, "MEMS-micropumps: A review," *Journal of Fluids Engineering*, vol. 124, no. 2, p. 384, 2002.

[22] P. Woias, "Micropumps - past, progress and future prospects," *Sensors and Actuators B: Chemical*, vol. 105, no. 1, pp. 28–38, 2005.

[23] J.-Y. Qian, C.-W. Hou, X.-J. Li, and Z.-J. Jin, "Actuation mechanism of microvalves: A review," *Micromachines*, vol. 11, no. 2, p. 172, 2020.

[24] K. W. Oh and C. H. Ahn, "A review of microvalves," *Journal of Micromechanics and Microengineering*, vol. 16, no. 5, pp. R13–R39, 2006.

[25] E. Chappel, "A review of passive constant flow regulators for microfluidic applications," *Applied Sciences*, vol. 10, no. 24, p. 8858, 2020.

[26] A. K. Au, H. Lai, B. R. Utela, and A. Folch, "Microvalves and micropumps for BioMEMS," *Micromachines*, vol. 2, no. 4, pp. 179–220, 2011.

[27] Y.-N. Wang and L.-M. Fu, "Micropumps and biomedical applications – a review," *Microelectronic Engineering*, vol. 195, pp. 121–138, 2018.

[28] A. N. Khan, A. Ermakov, G. Sukhorukov, and Y. Hao, "Radio frequency controlled wireless drug delivery devices," *Applied Physics Reviews*, vol. 6, no. 4, p. 041301, 2019.

[29] E. Meng and T. Hoang, "Micro- and nano-fabricated implantable drug-delivery systems," *Therapeutic delivery*, vol. 3, no. 12, pp. 1457–1467, 2012.

[30] C. L. Stevenson, J. T. Santini, and R. Langer, "Reservoir-based drug delivery systems utilizing microtechnology," *Advanced drug delivery reviews*, vol. 64, no. 14, pp. 1590–1602, 2012.

[31] N.-C. Tsai and C.-Y. Sue, "Review of MEMS-based drug delivery and dosing systems," *Sensors and Actuators A: Physical*, vol. 134, no. 2, pp. 555–564, 2007.

[32] A. B. Bußmann, L. M. Grünerbel, C. P. Durasiewicz, T. A. Thalhofer, A. Wille, and M. Richter, "Microdosing for drug delivery application—a review," *Sensors and Actuators A: Physical*, vol. 330, no. 6, p. 112820, 2021.

[33] M. Richter and J. Kruckow, "Pump arrangement comprising a safety valve," U.S. Patent 20100290935A1, 2010.

[34] M. Herz, M. Richter, and M. Wackerle, "Method for manufacturing a bending transducer, a micro pump and a micro valve, micro pump and micro valve," U.S. Patent 9410641B2, 2016.

[35] M. Richter, R. Linnemann, and P. Woias, "Robust design of gas and liquid micropumps," *Sensors and Actuators A: Physical*, vol. 68, no. 1-3, pp. 480–486, 1998.

[36] C. K. Wald and M. Richter, *Low-Cost Stainless Steel Micro Pumps for miniaturized early fire detection systems: MikroSystemTechnik Kongress 2015 ; 26. - 28. Oktober 2015 in Karlsruhe ; proceedings.* Berlin: VDE-Verl., 2015.

[37] C. Wald, Sebastian Kibler, M. Wackerle, and Y. Congar, "Microstructured fluid flow control device," U.S. Patent 20210041280A1, 2021.

[38] "Regulation (eu) 2017/745 of the european parliament and of the council of 5 april 2017 on medical devices, amending directive 2001/83/ec, regulation (ec) no 178/2002 and regulation (ec) no 1223/2009 and repealing council directives 90/385/eec and 93/42/eec."

[39] H. Shao, L. Liu, and H. L. Qu, "Machinability study on 3%Co–12%Cr stainless steel in milling," *Wear*, vol. 263, no. 1, pp. 736–744, 2007.

[40] D. O'Sullivan and M. Cotterell, "Machinability of austenitic stainless steel SS303," *Journal of Materials Processing Technology*, vol. 124, no. 1, pp. 153–159, 2002.

[41] E. O. Ezugwu and Z. M. Wang, "Titanium alloys and their machinability - a review," *Journal of Materials Processing Technology*, vol. 68, no. 3, pp. 262–274, 1997.

[42] M. Kikuchi and O. Okuno, "Machinability evaluation of titanium alloys," *Dental materials journal*, vol. 23, no. 1, pp. 37–45, 2004.

[43] J. N. Dupont, S. W. Banovic, and A. R. Marder, "Microstructural evolution and weldability of dissimilar welds between a super austenitic stainless steel and nickel-based alloys," *Welding Journal*, vol. 82, no. 6, p. 125, 2003.

[44] E. Ranatowski, "Weldability of titanium and its alloys-progress in joining," *Advances in Materials Science*, vol. 8, no. 2, pp. 69–76, 2008.

[45] D. M. Brunette, P. Tengvall, M. Textor, and P. Thomsen, *Titanium in medicine: material science, surface science, engineering, biological responses and medical applications*. Springer Science & Business Media, 2012.

[46] R. Buchli, P. Boesiger, and D. Meier, "Heating effects of metallic implants by MRI examinations," *Magnetic Resonance in Medicine*, vol. 7, no. 3, pp. 255–261, 1988.

[47] A. Holton, E. Walsh, A. Anayiotos, G. Pohost, and R. Venugopalan, "Comparative MRI compatibility of 316l stainless steel alloy and nickel–titanium alloy stents: Original article technical," *Journal of Cardiovascular Magnetic Resonance*, vol. 4, no. 4, pp. 423–430, 2002.

[48] A. Klocke, J. Kemper, D. Schulze, G. Adam, and B. Kahl-Nieke, "Magnetic field interactions of orthodontic wires during magnetic resonance imaging (MRI) at 1.5 tesla," *Journal of Orofacial Orthopedics/Fortschritte der Kieferorthopädie*, vol. 66, no. 4, pp. 279–287, 2005.

[49] A. T. Sidambe, "Biocompatibility of advanced manufactured titanium implants - a review," *Materials*, vol. 7, no. 12, pp. 8168–8188, 2014.

[50] L. Alting, F. Kimura, H. N. Hansen, and G. Bissacco, "Micro engineering," *CIRP Annals*, vol. 52, no. 2, pp. 635–657, 2003.

[51] E. Gentili, L. Tabaglio, and F. Aggogeri, "Review on micromachining techniques," in *AMST'05 Advanced Manufacturing Systems and Technology* (E. Kuljanic, ed.), (Vienna), pp. 387–396, Springer Vienna, 2005.

[52] F. Vollertsen, *Micro Metal Forming*, vol. 2 of *Lecture notes in production engineering*. Berlin, Heidelberg: Berlin, Heidelberg: Springer Berlin / Heidelberg, 2013.

[53] M. A. Câmara, J. C. Rubio, A. M. Abrão, and J. P. Davim, "State of the art on micromilling of materials, a review," *Journal of Materials Science & Technology*, vol. 28, no. 8, pp. 673–685, 2012.

[54] M. Takács, B. Verö, and I. Mészáros, "Micromilling of metallic materials," *Journal of Materials Processing Technology*, vol. 138, no. 1-3, pp. 152–155, 2003.

[55] D. P. Adams, M. J. Vasile, G. Benavides, and A. N. Campbell, "Micromilling of metal alloys with focused ion beam–fabricated tools," *Precision Engineering*, vol. 25, no. 2, pp. 107–113, 2001.

[56] D. J. Guckenberger, T. E. de Groot, A. M. D. Wan, D. J. Beebe, and E. W. K. Young, "Micromilling: a method for ultra-rapid prototyping of plastic microfluidic devices," *Lab on a Chip*, vol. 15, no. 11, pp. 2364–2378, 2015.

[57] W. E. Frazier, "Metal additive manufacturing: A review," *Journal of Materials Engineering and Performance*, vol. 23, no. 6, pp. 1917–1928, 2014.

[58] J. J. Lewandowski and M. Seifi, "Metal additive manufacturing: A review of mechanical properties," *Annual Review of Materials Research*, vol. 46, no. 1, pp. 151–186, 2016.

[59] R. M. Mahamood, *Laser metal deposition process of metals, alloys, and composite materials*. Springer, ISBN 331964985X, 2018.

[60] A. Townsend, N. Senin, L. Blunt, R. K. Leach, and J. S. Taylor, "Surface texture metrology for metal additive manufacturing: a review," *Precision Engineering*, vol. 46, pp. 34–47, 2016.

[61] N. Tuncer and A. Bose, "Solid-state metal additive manufacturing: A review," *JOM*, vol. 72, no. 9, pp. 3090–3111, 2020.

[62] A. Vafadar, F. Guzzomi, A. Rassau, and K. Hayward, "Advances in metal additive manufacturing: A review of common processes, industrial applications, and current challenges," *Applied Sciences*, vol. 11, no. 3, p. 1213, 2021.

[63] M. Yakout, M. A. Elbestawi, and S. C. Veldhuis, "A review of metal additive manufacturing technologies," *Solid State Phenomena*, vol. 278, pp. 1–14, 2018.

[64] S. D. Nath, A. Okello, R. Kelkar, G. Gupta, M. Kearns, and S. V. Atre, "Adapting L-PBF process for fine powders: a case study in 420 stainless steel," *Materials and Manufacturing Processes*, pp. 1–12, 2021.

[65] J. P. Oliveira, T. G. Santos, and R. M. Miranda, "Revisiting fundamental welding concepts to improve additive manufacturing: From theory to practice," *Progress in Materials Science*, vol. 107, p. 100590, 2020.

[66] T. Mayer, G. Brändle, A. Schönenberger, and R. Eberlein, "Simulation and validation of residual deformations in additive manufacturing of metal parts," *Heliyon*, vol. 6, no. 5, p. e03987, 2020.

[67] K. Frydrych and K. Kowalczyk-Gajewska, "Microstructure evolution in cold-rolled pure titanium: Modeling by the three-scale crystal plasticity approach accounting for twinning," *Metallurgical and Materials Transactions A*, vol. 49, no. 8, pp. 3610–3623, 2018.

[68] G. Zhang, H. Jiang, S. Tian, and Y. Zhang, "Effects of deformation conditions on the microstructure, texture and mechanical properties of Ti6Al4V alloy," *Materials Research Express*, vol. 6, no. 10, p. 1065b7, 2019.

[69] T. Kizu, K. Okuda, Y. Nagataki, T. Urabe, and K. Seto, "Influence of tensile strain on young's modulus in high-strength cold-rolled steel sheets," *ISIJ International*, vol. 55, no. 7, pp. 1502–1511, 2015.

[70] X. Huang, K. Suzuki, M. Yuasa, and Y. Chino, "Microstructural and textural evolution of pure titanium during differential speed rolling and subsequent annealing," *Journal of Materials Science*, vol. 49, no. 8, pp. 3166–3176, 2014.

[71] Z. Du, Y. Ma, F. Liu, N. Xu, Y. Chen, X. Wang, Y. Chen, T. Gong, and D. Xu, "The influences of process annealing temperature on microstructure and mechanical properties of near beta high strength titanium alloy sheet," *Materials (Basel, Switzerland)*, vol. 12, no. 9, 2019.

[72] K. Ahmmed, C. Grambow, and A.-M. Kietzig, "Fabrication of micro/nano structures on metals by femtosecond laser micromachining," *Micromachines*, vol. 5, no. 4, pp. 1219–1253, 2014.

[73] O. Balachninaitė, V. Tamulienė, L. Eičas, and V. Vaičaitis, "Laser micromachining of steel and copper using femtosecond laser pulses in GHz burst mode," *Results in Physics*, vol. 22, p. 103847, 2021.

[74] N. Faisal, D. Zindani, K. Kumar, and S. Bhowmik, "Laser micromachining of engineering materials - a review," in *Micro and Nano Machining of Engineering Materials: Recent Developments* (K. Kumar, D. Zindani, N. Kumari, and J. P. Davim, eds.), pp. 121–136, Cham: Springer International Publishing, 2019.

[75] J. Lehr and A.-M. Kietzig, "Production of homogenous micro-structures by femtosecond laser micro-machining," *Optics and Lasers in Engineering*, vol. 57, pp. 121–129, 2014.

[76] J. Lopez, E. Mottay, C. Loumena, Y. Zaouter, and M. Faucon, "Micromachining of metal and silicon using high average power ultrafast fiber lasers," in *Pacific*

International Conference on Applications of Lasers and Optics, p. M503, Laser Institute of America, 2010.

[77] P. Mannion, J. Magee, E. Coyne, and G. M. O'Connor, "Ablation thresholds in ultrafast laser micromachining of common metals in air," in *Opto-Ireland 2002: Optics and Photonics Technologies and Applications* (T. J. Glynn, ed.), SPIE Proceedings, p. 470, SPIE, 2002.

[78] M. Pfeiffer, A. Engel, S. Weißmantel, S. Scholze, and G. Reisse, "Microstructuring of steel and hard metal using femtosecond laser pulses," *Physics Procedia*, vol. 12, pp. 60–66, 2011.

[79] D. M. Allen, "The state of the art of photochemical machining at the start of the twenty-first century," *Proceedings of the Institution of Mechanical Engineers, Part B: Journal of Engineering Manufacture*, vol. 217, no. 5, pp. 643–650, 2003.

[80] D. M. Allen and H. J. Almond, "Characterisation of aqueous ferric chloride etchants used in industrial photochemical machining," *Journal of Materials Processing Technology*, vol. 149, no. 1-3, pp. 238–245, 2004.

[81] R. Roy, D. Allen, and O. Zamora, "Cost of photochemical machining," *Journal of Materials Processing Technology*, vol. 149, no. 1-3, pp. 460–465, 2004.

[82] P. Nageswara Rao and D. Kunzru, "Fabrication of microchannels on stainless steel by wet chemical etching," *Journal of Micromechanics and Microengineering*, vol. 17, no. 12, pp. N99–N106, 2007.

[83] J. Zhang and Y. Meng, "A study of surface texturing of carbon steel by photochemical machining," *Journal of Materials Processing Technology*, vol. 212, no. 10, pp. 2133–2140, 2012.

[84] D. M. Allen, "Photochemical machining: from 'manufacturing's best kept secret' to a $6 billion per annum, rapid manufacturing process," *CIRP Annals*, vol. 53, no. 2, pp. 559–572, 2004.

[85] D. Agrawal and D. Kamble, "Optimization of photochemical machining process parameters for manufacturing microfluidic channel," *Materials and Manufacturing Processes*, vol. 34, no. 1, pp. 1–7, 2019.

[86] ACE Advanced Chemical Etching Ltd, "Chemical etching: https://ace-uk.net/processes/chemical-etching/," accessed on 25.02.2022.

[87] M. Naeem, "Developments in laser microwelding technology," in *Handbook of Laser Welding Technologies : Woodhead Publishing Series in Electronic and Optical Materials* (S. Katayama, ed.), pp. 163–211, Woodhead Publishing, 2013.

[88] M. M. Hailat, A. Mian, Z. A. Chaudhury, G. Newaz, R. Patwa, and H. J. Herfurth, "Laser micro-welding of aluminum and copper with and without tin foil alloy," *Microsystem Technologies*, vol. 18, no. 1, pp. 103–112, 2012.

[89] M. Maina, Y. Okamoto, R. Inoue, S.-i. Nakashiba, A. Okada, and T. Sakagawa, "Influence of surface state in micro-welding of copper by Nd:YAG laser," *Applied Sciences*, vol. 8, no. 12, p. 2364, 2018.

[90] M. Hummel, C. Schöler, A. Häusler, A. Gillner, and R. Poprawe, "New approaches on laser micro welding of copper by using a laser beam source with a wavelength of 450 nm," *Journal of Advanced Joining Processes*, vol. 1, p. 100012, 2020.

[91] A. Olowinsky, T. Kramer, N. Dumont, and H. Hanebuth, "New applications of laser beam micro welding," in *International Congress on Applications of Lasers & Electro-Optics*, pp. 1803–1812, Laser Institute of America, 2001.

[92] L. D. Cedeño-Viveros, E. Vázquez-Lepe, C. A. Rodríguez, and E. García-López, "Influence of process parameters for sheet lamination based on laser micro-spot welding of austenitic stainless steel sheets for bone tissue applications," *The International Journal of Advanced Manufacturing Technology*, vol. 115, no. 1-2, pp. 247–262, 2021.

[93] M. M. Quazi, M. Ishak, M. A. Fazal, A. Arslan, S. Rubaiee, M. H. Aiman, A. Qaban, F. Yusof, T. Sultan, M. M. Ali, and S. M. Manladan, "A comprehensive assessment of laser welding of biomedical devices and implant materials: recent research, development and applications," *Critical Reviews in Solid State and Materials Sciences*, vol. 46, no. 2, pp. 109–151, 2021.

[94] G. Lütjering and J. C. Williams, *Titanium*. Engineering materials and processes, Berlin and New York: Springer, 2nd ed. ed., 2007.

[95] A. Patschger, J. Bliedtner, M. Hild, and J. Pierre Bergmann, "Flexible and efficient laser remote welding of ultra-thin metal foils," *Journal of Laser Applications*, vol. 24, no. 5, p. 052005, 2012.

[96] S. Katayama, ed., *Handbook of Laser Welding Technologies : Woodhead Publishing Series in Electronic and Optical Materials*. Woodhead Publishing, 2013.

[97] J. Kim, S. Kim, K. Kim, W. Jung, D. Youn, J. Lee, and H. Ki, "Effect of beam size in laser welding of ultra-thin stainless steel foils," *Journal of Materials Processing Technology*, vol. 233, pp. 125–134, 2016.

[98] A. Kurc-Lisiecka and A. Lisiecki, "Laser welding of stainless steel," *Journal of Achievements in Materials and Manufacturing Engineering*, vol. 1, no. 98, pp. 32–40, 2020.

[99] I. Miyamoto, S.-j. Park, and T. Ooie, "Precision microwelding of thin metal sheet with fiber laser," in *International Congress on Applications of Lasers & Electro-Optics*, p. 172631, Laser Institute of America, October 14–17, 2002.

[100] A. Ascari, A. Fortunato, G. Guerrini, E. Liverani, and A. Lutey, "Long pulse laser micro welding of commercially pure titanium thin sheets," *Procedia Engineering*, vol. 184, pp. 274–283, 2017.

[101] A. Kumar, S. Neogy, N. Keskar, and D. J. Biswas, "Laser microwelding of stainless steel and pure aluminum foil," *Journal of Laser Applications*, vol. 34, no. 1, p. 012022, 2022.

[102] M. Boley, F. Abt, R. Weber, and T. Graf, "X-ray and optical videography for 3D measurement of capillary and melt pool geometry in laser welding," *Physics Procedia*, vol. 41, pp. 488–495, 2013.

[103] X. He, J. W. Elmer, and T. DebRoy, "Heat transfer and fluid flow in laser microwelding," *Journal of Applied Physics*, vol. 97, no. 8, p. 084909, 2005.

[104] A. Matsunawa, J.-D. Kim, N. Seto, M. Mizutani, and S. Katayama, "Dynamics of keyhole and molten pool in laser welding," *Journal of Laser Applications*, vol. 10, no. 6, pp. 247–254, 1998.

[105] I. Miyamoto, S.-j. Park, and T. Ooie, "Ultrafine-keyhole welding process using single-mode fiber laser," in *International Congress on Applications of Lasers & Electro-Optics*, p. M201, Laser Institute of America, October 13–16, 2003.

[106] A. Patschger, M. Hild, J. P. Bergmann, and J. Bliedtner, "Examinations on laser-welded joints of ultra-thin metallic foils," in *International Congress on Applications of Lasers & Electro-Optics*, pp. 794–803, Laser Institute of America, September 23–27, 2012.

[107] H. Sheikhbahaee, M. R. Pakmanesh, S. J. Mirahmadi, and S. Asghari, "Investigating governing parameters influencing solidification process in pulsed laser micro-welding of AISI 316l thin foils using finite element method," *The International Journal of Advanced Manufacturing Technology*, vol. 116, no. 5-6, pp. 1819–1830, 2021.

[108] T. Zacharia, S. A. David, J. M. Vitek, and T. DebRoy, "Heat transfer during nd: Yag pulsed laser welding and its effect on solidification structure of austenitic stainless steels," *Metallurgical and Materials Transactions A*, vol. 20, no. 5, pp. 957–967, 1989.

[109] S. Akella, H. Vemanaboina, and R. Kumar Buddu, "Heat flux for welding processes: Model for laser weld," *Sreyas International Journal of Scientists and Technocrats*, vol. 1, no. 1, pp. 10–15, 2016.

[110] P. Perulli, M. Dassisti, and G. Casalino, "Thermo-mechanical simulation of hybrid welding of DP/AISI 316 and TWIP/AISI 316 dissimilar weld," *Materials (Basel, Switzerland)*, vol. 13, no. 9, 2020.

[111] M. Naeem, S. Lewis, and J. Chinn, "Microwelding performance comparison between a low power (125W) pulsed Nd:YAG laser and a low power (100-200W) single mode fiber laser," in *Pacific International Conference on Applications of Lasers and Optics*, pp. 721–726, Laser Institute of America, April 16–18, 2008.

[112] M. Naeem and S. Lewis, "Micro joining and cutting with a single mode fiber laser," in *Pacific International Conference on Applications of Lasers and Optics*, pp. 400–405, Laser Institute of America, April 3–5, 2006.

[113] A. F. H. Kaplan and J. Powell, "Spatter in laser welding," *Journal of Laser Applications*, vol. 23, no. 3, p. 032005, 2011.

[114] A. Patschger, A. Hopf, T. Loose, J. Bliedtner, and J. P. Bergmann, "New approach to clamping in microwelding," *Journal of Laser Applications*, vol. 27, no. S2, p. S29013, 2015.

[115] A. Otto, A. Patschger, and M. Seiler, "Numerical and experimental investigations of humping phenomena in laser micro welding," *Physics Procedia*, vol. 83, pp. 1415–1423, 2016.

[116] P. G. Riofrío, C. A. Capela, J. Am Ferreira, and A. Ramalho, "Interactions of the process parameters and mechanical properties of laser butt welds in thin

high strength low alloy steel plates," *Proceedings of the Institution of Mechanical Engineers, Part L: Journal of Materials: Design and Applications*, vol. 234, no. 5, pp. 665–680, 2020.

[117] M. Baruah and S. Bag, "Influence of pulsation in thermo-mechanical analysis on laser micro-welding of Ti6Al4V alloy," *Optics & Laser Technology*, vol. 90, pp. 40–51, 2017.

[118] M. Baruah and S. Bag, "Microstructural influence on mechanical properties in plasma microwelding of Ti6Al4V alloy," *Journal of Materials Engineering and Performance*, vol. 25, no. 11, pp. 4718–4728, 2016.

[119] M. N. M. Salleh, M. Ishak, M. M. Quazi, and M. H. Aiman, "Microstructure, mechanical, and failure characteristics of laser-microwelded AZ31B Mg alloy optimized by response surface methodology," *The International Journal of Advanced Manufacturing Technology*, vol. 99, no. 1-4, pp. 985–1001, 2018.

[120] P. Edwards and M. Ramulu, "Surface residual stresses in Ti-6Al-4V friction stir welds: Pre- and post-thermal stress relief," *Journal of Materials Engineering and Performance*, vol. 24, no. 9, pp. 3263–3270, 2015.

[121] F. G. Mur, D. Rodríguez, and J. A. Planell, "Influence of tempering temperature and time on the alpha'-Ti-6Al-4V martensite," *Journal of alloys and compounds*, vol. 234, no. 2, pp. 287–289, 1996.

[122] Y.-K. Kim, S.-H. Park, Y.-J. Kim, B. Almangour, and K.-A. Lee, "Effect of stress relieving heat treatment on the microstructure and high-temperature compressive deformation behavior of Ti-6Al-4V alloy manufactured by selective laser melting," *Metallurgical and Materials Transactions A*, vol. 49, no. 11, pp. 5763–5774, 2018.

[123] B. D. Venkatesh, D. L. Chen, and S. D. Bhole, "Effect of heat treatment on mechanical properties of Ti-6Al-4V ELI alloy," *Materials Science and Engineering: A*, vol. 506, no. 1-2, pp. 117–124, 2009.

[124] G. Yan, M. J. Tan, A. Crivoi, F. Li, S. Kumar, and C. H. Nicholas Chia, "Improving the mechanical properties of tig welding Ti-6Al-4V by post weld heat treatment," *Procedia Engineering*, vol. 207, pp. 633–638, 2017.

[125] A. Patschger, J. Bliedtner, and J. P. Bergmann, "Approaches to increase process efficiency in laser micro welding," *Physics Procedia*, vol. 41, pp. 592–602, 2013.

[126] A. Patschger, M. Güpner, J. Bliedtner, and J. P. Bergmann, "Remote micro welding with multi-mode and single-mode fiber lasers – a comparison," in *International Congress on Applications of Lasers & Electro-Optics*, pp. 805–815, Laser Institute of America, October 6–10, 2013.

[127] A. Patschger, J. Bliedtner, and J. P. Bergmann, "Process-limiting factors and characteristics of laser-based micro welding," *Physics Procedia*, vol. 56, pp. 740–749, 2014.

[128] M. Petrich, M. Stambke, and J. P. Bergmann, "Examinations on laser remote welding of ultra-thin metal foils under vacuum conditions," *Physics Procedia*, vol. 56, pp. 768–775, 2014.

[129] F. Schmitt, "Laser beam micro welding with high brilliant fiber lasers," *Journal of Laser Micro/Nanoengineering*, vol. 5, no. 3, pp. 197–203, 2010.

[130] M. Güpner, A. Patschger, and J. Bliedtner, "Influence of process parameters on the process efficiency in laser metal deposition welding," *Physics Procedia*, vol. 83, pp. 657–666, 2016.

[131] G. Tsoukantas and G. Chryssolouris, "Theoretical and experimental analysis of the remote welding process on thin, lap-joined AISI 304 sheets," *The International Journal of Advanced Manufacturing Technology*, vol. 35, no. 9-10, pp. 880–894, 2008.

[132] A. AlHazaa and N. Haneklaus, "Diffusion bonding and transient liquid phase (TLP) bonding of type 304 and 316 austenitic stainless steel - a review of similar and dissimilar material joints," *Metals*, vol. 10, no. 5, p. 613, 2020.

[133] N. F. Kazakov, *Diffusion bonding of materials*. Elsevier, 2013.

[134] T. Gietzelt, V. Toth, A. Huell, F. Messerschmidt, and R. Dittmeyer, "Systematic investigation of the diffusion welding behavior of the austenitic stainless steel 304 (1.4301)," *Advanced Engineering Materials*, vol. 16, no. 11, pp. 1381–1390, 2014.

[135] M. Katoh, N. Sato, T. Shiratori, and Y. Suzuki, "Reduction of diffusion bonding temperature with recrystallization at austenitic stainless steel," *Tetsu-to-Hagane*, vol. 102, no. 1, pp. 34–39, 2016.

[136] T. Aizawa and T. Shiratori, "Microforming of stainless steel miniature pump by additive sheet-manufacturing," *Materials Transactions*, vol. 61, no. 2, pp. 266–271, 2020.

[137] T. Gietzelt, M. Walter, V. Toth, F. Messerschmidt, and M. Blem, "Comprehensive study of the influence of the bonding temperature and contact pressure regimes during diffusion bonding on the deformation and mechanical properties of AISI 304," *Advanced Engineering Materials*, vol. 23, no. 8, p. 2100188, 2021.

[138] D. G. Sanders and M. Ramulu, "Examination of superplastic forming combined with diffusion bonding for titanium: Perspective from experience," *Journal of Materials Engineering and Performance*, vol. 13, no. 6, pp. 744–752, 2004.

[139] O. A. Kaibyshev, R. V. Safiullin, R. Y. Lutfullin, O. R. Valiakhmetov, R. M. Galeyev, A. Dutta, T. Raghu, and G. G. Saha, "Advanced superplastic forming and diffusion bonding of titanium alloy," *Materials Science and Technology*, vol. 22, no. 3, pp. 343–348, 2006.

[140] H. Liu, J. Cao, P. He, and J. C. Feng, "Effect of hydrogen on diffusion bonding of commercially pure titanium and hydrogenated Ti6Al4V alloys," *International Journal of Hydrogen Energy*, vol. 34, no. 2, pp. 1108–1113, 2009.

[141] I. Tomashchuk and P. Sallamand, "Metallurgical strategies for the joining of titanium alloys with steels," *Advanced Engineering Materials*, vol. 20, no. 6, p. 1700764, 2018.

[142] D.-f. Mo, T.-f. Song, Y.-j. Fang, X.-s. Jiang, C. Q. Luo, M. D. Simpson, and Z.-p. Luo, "A review on diffusion bonding between titanium alloys and stainless steels," *Advances in Materials Science and Engineering*, vol. 2018, pp. 1–15, 2018.

[143] Y. Fang, X. Jiang, D. Mo, D. Zhu, and Z. Luo, "A review on dissimilar metals' welding methods and mechanisms with interlayer," *The International Journal of Advanced Manufacturing Technology*, vol. 102, no. 9-12, pp. 2845–2863, 2019.

[144] K. O. Cooke and A. M. Atieh, "Current trends in dissimilar diffusion bonding of titanium alloys to stainless steels, aluminium and magnesium," *Journal of Manufacturing and Materials Processing*, vol. 4, no. 2, p. 39, 2020.

[145] T. Gietzelt, V. Toth, A. Huell, and R. Dittmeyer, "Determining the dependence of deformation during diffusion welding on the aspect ratio using samples made of SS 304 (1.4301)," *Advanced Engineering Materials*, vol. 19, no. 2, p. 1600344, 2017.

[146] T. Gietzelt, V. Toth, and A. Huell, "Challenges of diffusion bonding of different classes of stainless steels," *Advanced Engineering Materials*, vol. 20, no. 2, p. 1700367, 2018.

[147] R. Reuven, A. Bolind, N. Haneklaus, C. Cionea, C. Andreades, G. Buster, P. Hosemann, and P. Peterson, "Ni interlayer to improve low-pressure diffusion bonding of 316l ss press fit tube-to-tubesheet joints for coiled tube gas heaters," *Journal of Nuclear Engineering and Radiation Science*, vol. 3, no. 3, 2017.

[148] N. Haneklaus, R. Reuven, C. Cionea, P. Hosemann, and P. F. Peterson, "Development of engineering parameters for low pressure diffusion bonds of 316 ss tube-to-tube sheet joints for fhr heat exchangers," in *TMS 2016 145th Annual Meeting & Exhibition*, pp. 583–588, Springer, 2016.

[149] A. AlHazaa, N. Haneklaus, and Z. Almutairi, "Impulse pressure-assisted diffusion bonding (ipadb): Review and outlook," *Metals*, vol. 11, no. 2, p. 323, 2021.

[150] M. Herz, D. Horsch, G. Wachutka, T. C. Lueth, and M. Richter, "Design of ideal circular bending actuators for high performance micropumps," *Sensors and Actuators A: Physical*, vol. 163, no. 1, pp. 231–239, 2010.

[151] S. J. Collocott and G. K. White, "Thermal expansion and heat capacity of some stainless steels and feni alloys," *Cryogenics*, vol. 26, no. 7, pp. 402–405, 1986.

[152] PI Ceramic GmbH, "Piezoelectric ceramic products: Fundamentals, characteristics and applications," *Catalogue*, vol. CAT125E R3, 2016.

[153] T. Lemke, J. Kloeker, G. Biancuzzi, T. Huesgen, F. Goldschmidtboeing, and P. Woias, "Fabrication of a normally-closed microvalve utilizing lithographically defined silicone micro o-rings," *Journal of Micromechanics and Microengineering*, vol. 21, no. 2, p. 025011, 2011.

[154] S. Chen, S. Lu, Y. Liu, J. Wang, X. Tian, G. Liu, and Z. Yang, "A normally-closed piezoelectric micro-valve with flexible stopper," *AIP Advances*, vol. 6, no. 4, p. 045112, 2016.

[155] A. Shabanian, F. Goldschmidtboeing, S. Vilches, H.-H. Phan, A. Bhat Kashekodi, P. Rajaeipour, and P. Woias, "A novel piezo actuated high stroke membrane for micropumps," *Microelectronic Engineering*, vol. 158, pp. 26–29, 2016.

[156] X. Wu, S.-H. Kim, C.-H. Ji, and M. G. Allen, "A solid hydraulically amplified piezoelectric microvalve," *Journal of Micromechanics and Microengineering*, vol. 21, no. 9, p. 095003, 2011.

[157] G.-S. Chung and K.-B. Han, "Characteristics of a micromachined piezovalve combined with a multilayer ceramic actuator," *Microelectronics Journal*, vol. 38, no. 6-7, pp. 690–694, 2007.

[158] B. Yang, B. Wang, and W. K. Schomburg, "A thermopneumatically actuated bistable microvalve," *Journal of Micromechanics and Microengineering*, vol. 20, no. 9, p. 095024, 2010.

[159] J. Lv, Y. Jiang, D. Zhang, Y. Zhao, and X. Sun, "Characterization on the fatigue performance of a piezoelectric microvalve with a microfabricated silicon valve seat," *Journal of Micromechanics and Microengineering*, vol. 24, no. 1, p. 015013, 2014.

[160] Michael Scheuenpflug, Daniel Guenther, Franz Irlinger, Tim Lueth, "Microfluidic module system with piezo driven microvalve for synthesis of radiopharmaceutical products," *Proceedings of IEEE EMBS*, 2007.

[161] E.-H. Yang, C. Lee, J. Mueller, and T. George, "Leak-tight piezoelectric microvalve for high-pressure gas micropropulsion," *Journal of Microelectromechanical Systems*, vol. 13, no. 5, pp. 799–807, 2004.

[162] D. Zhang, J. Lv, Y. Jiang, H. Chen, and J. Fu, "A piezoelectric microvalve with a flexure-hinged driving frame and microfabricated silicon sealing pair," *Mechatronics*, vol. 24, no. 5, pp. 511–518, 2014.

[163] C. Lee, E.-H. Yang, S. M. Saeidi, and J. M. Khodadadi, "Fabrication, characterization, and computational modeling of a piezoelectrically actuated microvalve for liquid flow control," *Journal of Microelectromechanical Systems*, vol. 15, no. 3, pp. 686–696, 2006.

[164] E.-H. Yang, C. Lee, and J. M. Khodadadi, "Development of MEMS-based piezoelectric microvalve technologies," *Sensors and Materials*, vol. 19, no. 1, pp. 001–018, 2007.

[165] P.-J. Chen, D. C. Rodger, M. S. Humayun, and Y.-C. Tai, "Floating-disk parylene microvalves for self-pressure-regulating flow controls," *Journal of Microelectromechanical Systems*, vol. 17, no. 6, pp. 1352–1361, 2008.

[166] P. V. M. Ramanamurthy, R. Ahrens, and S. Karmalkar, "Piezoelectric microvalve," *Indian Journal of Pure & Applied Physics*, no. 0019-5596, 2007.

[167] T. Rogge, Z. Rummler, and W. K. Schomburg, "Polymer micro valve with a hydraulic piezo-drive fabricated by the amanda process," *Sensors and Actuators A: Physical*, vol. 110, no. 1-3, pp. 206–212, 2004.

[168] H. N. Schwerdt, U. Amjad, J. Appel, A. M. Elhadi, T. Lei, M. C. Preul, R. E. Bristol, and J. Chae, "In vitro hydrodynamic, transient, and overtime performance of a miniaturized valve for hydrocephalus," *Annals of Biomedical Engineering*, vol. 43, no. 3, pp. 603–615, 2015.

[169] K. Kolari, T. Havia, I. Stuns, and K. Hjort, "Flow restrictor silicon membrane microvalve actuated by optically controlled paraffin phase transition," *Journal of Micromechanics and Microengineering*, vol. 24, no. 8, p. 084003, 2014.

[170] B. Yang and Q. Lin, "A latchable microvalve using phase change of paraffin wax," *Sensors and Actuators A: Physical*, vol. 134, no. 1, pp. 194–200, 2007.

[171] A. Pannikottu, J. Seiler, and J. J. Leyden, "Non-linear finite element analysis support testing for elastomer parts," *American Chemical Society Division of Rubber Chemistry*, 1995.

[172] M. Kunnil, D. Yamarthi, and S. K. Kompally, "Finite element analysis of elastomers using ANSYS," in *International Conference on Nuclear Engineering*, pp. 75–82, American Society of Mechanical Engineers, 2012.

[173] S. Shen, D. Zhong, S. Qu, and R. Xiao, "A hyperelastic-damage model based on the strain invariants," *Extreme Mechanics Letters*, vol. 52, p. 101641, 2022.

[174] N. Elango and R. Marappan, "Analysis on the fundamental deformation effect of a robot soft finger and its contact width during power grasping," *The International Journal of Advanced Manufacturing Technology*, vol. 52, no. 5-8, pp. 797–804, 2011.

[175] J. Jung, I. Hwang, and D. Lee, "Contact pressure and strain energy density of hyperelastic u-shaped monolithic seals under axial and radial compressions in an insulating joint: A numerical study," *Applied Sciences*, vol. 7, no. 8, p. 792, 2017.

[176] A. Makino, W. R. Hamburgen, and J. S. Fitch, "Fluoroelastomer pressure pad design for microelectronic applications," *CiteseerX*, 1993.

[177] T. Ohori, S. Shoji, K. Miura, and A. Yotsumoto, "Partly disposable three-way microvalve for a medical micro total analysis system," *Proceedings of the 5th International Conference on Solid-State Sensors and Actuators and Eurosensors III*, vol. 64, no. 1, pp. 57–62, 1998.

[178] M. Khoo and C. Liu, "Micro magnetic silicone elastomer membrane actuator," *Sensors and Actuators A: Physical*, vol. 89, no. 3, pp. 259–266, 2001.

[179] X. Yang, C. Grosjean, Yu-Chong Tai, and Chih-Ming Ho, "A MEMS thermopneumatic silicone membrane valve," in *Proceedings IEEE The Tenth Annual International Workshop on Micro Electro Mechanical Systems*, pp. 114–118, 1997.

[180] M. Kohl, K. D. Skrobanek, and S. Miyazaki, "Development of stress-optimised shape memory microvalves," *Sensors and Actuators A: Physical*, vol. 72, no. 3, pp. 243–250, 1999.

[181] C. J. van Mullem, K. J. Gabriel, and H. Fujita, "Large deflection performance of surface micromachined corrugated diaphragms," in *Transducers: 1991 International Conference on Solid-State Sensors and Actuators*, pp. 1014–1017, 1991.

[182] M. Cieślik, M. Kot, W. Reczyński, K. Engvall, W. Rakowski, and A. Kotarba, "Parylene coatings on stainless steel 316l surface for medical applications–mechanical and protective properties," *Materials science & engineering. C, Materials for biological applications*, vol. 32, no. 1, pp. 31–35, 2012.

[183] S. T. Güntner, *Development of a sealing design for active NO valves and analysis of the sealing design with Parylene-C coating for hydraulically actuated SafetyValves: Entwicklung eines Dichtdesigns für aktive NO-Ventile und Analyse des Dichtdesigns mit Parylene-C-Beschichtung bei hydraulisch aktuierten SafetyValves.* Bachelor thesis, Ostbayerische Technische Hochschule, Amberg-Weiden, 2021.

[184] B. N. J. Persson, "Relation between interfacial separation and load: a general theory of contact mechanics," *Physical review letters*, vol. 99, no. 12, p. 125502, 2007.

[185] Public Law 94-295, "Medical device amendments of 1976," *90 Stat. 539*, 1976.

[186] K. S. Ramadan, D. Sameoto, and S. Evoy, "A review of piezoelectric polymers as functional materials for electromechanical transducers," *Smart Materials and Structures*, vol. 23, no. 3, p. 033001, 2014.

[187] K. Prashanthi, M. Naresh, V. Seena, T. Thundat, and V. Ramgopal Rao, "A novel photoplastic piezoelectric nanocomposite for MEMS applications," *Journal of Microelectromechanical Systems*, vol. 21, no. 2, pp. 259–261, 2012.

[188] M. Rübner, C. Körner, and R. F. Singer, "Integration of piezoceramic modules into die castings - procedure and functionalities," in *Emboding Intelligence in Structures and Integrated Systems*, Advances in Science and Technology, pp. 170–175, Trans Tech Publications LtdSwitzerland, 2008.

[189] O. Fuchs, Y. Fouillet, S. Maubert, M. Cochet, C. Chabrol, N. David, X. Médal, and R. Campagnolo, "A novel volumetric silicon micropump with integrated sensors," *Microelectronic Engineering*, vol. 97, pp. 375–378, 2012.

[190] E. Chappel, C. Conan, S. Mefti, F. Cannehan, G.-L. Lettieri, S. Proennecke, L. Zanotti, M. Ferrera, A. Merassi, and L. Oggioni, "Infusion micro-pump development using MEMS technology," *HAL archives ouvertes*, 2012.

[191] A. T. Evans, J. M. Park, S. Chiravuri, and Y. B. Gianchandani, "A low power, microvalve regulated architecture for drug delivery systems," *Biomedical Microdevices*, vol. 12, no. 1, pp. 159–168, 2010.

[192] Z. Zhang, J. Kan, S. Wang, H. Wang, J. Wen, and Z. Ma, "Flow rate self-sensing of a pump with double piezoelectric actuators," *Mechanical Systems and Signal Processing*, vol. 41, no. 1-2, pp. 639–648, 2013.

[193] G. Jiang and D. D. Zhou, "Technology advances and challenges in hermetic packaging for implantable medical devices," in *Implantable Neural Prostheses 2: Techniques and Engineering Approaches* (D. Zhou and E. Greenbaum, eds.), pp. 27–61, New York, NY: Springer New York, 2010.

[194] T. Hanawa, "Research and development of metals for medical devices based on clinical needs," *Science and technology of advanced materials*, vol. 13, no. 6, p. 064102, 2012.

[195] M. Peters, J. Hemptenmacher, J. Kumpfert, and C. Leyens, "Structure and properties of titanium and titanium alloys," *Titanium and titanium alloys: fundamentals and applications*, pp. 1–36, 2003.

[196] Z. Chen, U. Gandhi, J. Lee, and R. H. Wagoner, "Variation and consistency of young's modulus in steel," *Journal of Materials Processing Technology*, vol. 227, pp. 227–243, 2016.

[197] V. Geanta, I. Voiculescu, R. Stefanoiu, and E. R. Rusu, "Stainless steels with biocompatible properties for medical devices," *Key Engineering Materials*, vol. 583, pp. 9–15, 2013.

[198] International Organization for Standardization, "Implants for surgery - active implantable medical devices: Part 4: Implantable infusion pumps," ISO 14708-4, 2008.

[199] A. Bußmann, H. Leistner, D. Zhou, M. Wackerle, Y. Congar, M. Richter, and J. Hubbuch, "Piezoelectric silicon micropump for drug delivery applications," *Applied Sciences*, vol. 11, no. 17, p. 8008, 2021.

[200] P.-H. Cazorla, O. Fuchs, M. Cochet, S. Maubert, G. Le Rhun, Y. Fouillet, and E. Defay, "A low voltage silicon micro-pump based on piezoelectric thin films," *Sensors and Actuators A: Physical*, vol. 250, pp. 35–39, 2016.

[201] A. F. Doll, M. Wischke, A. Geipel, F. Goldschmidtboeing, O. Ruthmann, U. T. Hopt, H.-J. Schrag, and P. Woias, "A novel artificial sphincter prosthesis driven by a four-membrane silicon micropump," *Sensors and Actuators A: Physical*, vol. 139, no. 1-2, pp. 203–209, 2007.

[202] W. S. Griffin, H. H. Richardson, and S. Yamanami, "A study of fluid squeeze-film damping," *Journal of Basic Engineering*, no. 88(2), pp. 451–456, 1966.

[203] A. H. Nayfeh and M. I. Younis, "A new approach to the modeling and simulation of flexible microstructures under the effect of squeeze-film damping," *Journal of Micromechanics and Microengineering*, vol. 14, no. 2, pp. 170–181, 2004.

[204] C. Zhang, G. Xu, and Q. Jiang, "Characterization of the squeeze film damping effect on the quality factor of a microbeam resonator," *Journal of Micromechanics and Microengineering*, vol. 14, no. 10, pp. 1302–1306, 2004.

[205] S. M. Pilgrim, A. E. Bailey, M. Massuda, F. C. Poppe, and A. P. Ritter, "Fabrication and characterization of pzt multilayer actuators," *Ferroelectrics*, vol. 160, no. 1, pp. 305–316, 1994.

[206] T. Lemke, G. Biancuzzi, C. Farhat, B. Vodermayer, O. Ruthmann, T. Schmid, H. J. Schrag, P. Woias, and F. Goldschmidtboeing, "High performance micropumps utilizing multilayer piezo actuators," *Proceedings of Eurosensors XXII*, pp. 589–592, 2008.

Appendix

Sensors and Actuators A 323 (2021) 112649

Contents lists available at ScienceDirect

Sensors and Actuators A: Physical

journal homepage: www.elsevier.com/locate/sna

Piezoelectric titanium based microfluidic pump and valves for implantable medical applications

Agnes Beate Bußmann[a,b,*,1], Claudia Patricia Durasiewicz[a,c,*,1], Sebastian Heinrich Alexander Kibler[a], Christian Klaus Wald[a]

[a] Fraunhofer EMFT Research Institution for Microsystems and Solid State Technologies, Hansastrasse 27d, 80686, Munich, Germany
[b] KIT, MAB - Biomolecular Separation Engineering, Fritz-Haber-Weg 2, 76131, Karlsruhe, Germany
[c] TUM, TEP - Chair of Physics of Electrotechnology, Theresienstrasse 90, 80333, Munich, Germany

ARTICLE INFO

Article history:
Received 9 November 2020
Received in revised form 15 January 2021
Accepted 19 February 2021
Available online 26 February 2021

Keywords:
Micropump
Microvalve
Titanium
Piezoelectric bending actuator
Microfluidic system
Microfluidic implant

ABSTRACT

Medical devices often require precise movement of fluids. Automated implants with no need for manual handling improve patient care significantly. However, existing microfluidic devices do not fulfil the necessary specifications of size, safety, hermetic sealing, and artefact free medical imaging, as well as energy efficiency combined with adapted fluidic properties. In this work we designed, manufactured, and experimentally evaluated three piezoelectric microfluidic devices for implant automation: a diaphragm pump, a normally closed valve, and a normally open valve. All devices are made of titanium, minimizing the risk of artefacts in medical imaging. They have similar form factors and use the same actuation method. For the later, a specific mounting process of the piezo actuator enables outstanding fluidic performance during experimental evaluations. The titanium micropumps show a maximal flow of (14 ± 2.2) ml/min and pressure build-up of 75 kPa. The normally closed valve's leakage rates are extremely low with less than 1 µL/min. Detailed investigations further include the actuator stroke, a lifetime study for normally open valves, and a numerical and experimental evaluation of the normally closed valve's spring foil. The introduced titanium technology platform is ideally suited for system integration accounted for by the use of the same actuation principle and the similar form factor and a simple design. The development of small, smart, and energy efficient implants for improved treatment is possible based on the introduced platform.

1. Introduction

The transport of liquids is an ubiquitous task in implantable medical applications. Examples are, among others, microfluidic systems to move body fluids, dose medication precisely, or hydraulic implants [1–3]. Prosthetic hands [4], extra-aortic balloon (EAB) pumps [5], as well as artificial sphincters base on hydraulic actuation. These implants can be realized using flexible, fluid-filled actuators, such as artificial fingers [4], or a cuff placed around a vessel or muscular tube, to facilitate a biological function. The actuators are operated using intra- or extracorporeal pumps and/or valves. Cuffs in EAB devices are dynamically pressurized by extracorporeal pumps to levels of 250–300 mmHg (333–400 mbar), providing cardiac support by increased blood flow for patients suffering from heart failure [5]. However, current systems are too large for implantation. Sphincter implants [6,7] restore opening and closing functionalities in the rectal or urinary path. Current systems on the market are manual devices which the patient operates by hand. Furthermore, the physician sets the pressure to a fixed level that is not adapted to the patient's activity, which can cause tissue damage. Even if specifications vary largely with the use case, a small, light, automated, and user-friendly device is desired for future developments of implants. Ever since the first studies on piezoelectric diaphragm pumps [8], many different kinds of micropumps have been developed to enable reliable, safe, and economic medical products [9,10].

Micropumps in research achieve water flow rates of up to 9.1 mL/min or water pressures of up to 40 kPa, though fail to exhibit high flow and pressure simultaneously [11]. Additionally, the

Abbreviations: EAB, extra-aortic balloon; FEM, finite-element-modelling; FKM, fluorocarbon; MRI, magnetic resonance imaging; NC, normally closed; NO, normally open.

* Corresponding authors at: Fraunhofer EMFT Research Institution for Microsystems and Solid State Technologies, Hansastrasse 27d, 80686, Munich, Germany.
E-mail addresses: Agnes.Bussmann@emft.fraunhofer.de (A.B. Bußmann), Claudia.Patricia.Durasiewicz@emft.fraunhofer.de (C.P. Durasiewicz).

[1] A. Bußmann and C. Durasiewicz contributed equally.

https://doi.org/10.1016/j.sna.2021.112649

occurrence of bubbles due to degassing or cavitation [12] impacts the fluidic performance. For safety reasons, medical applications require bubble tolerance, even under backpressure. We therefore seek to develop a high performance micropump with bubble tolerance capabilities. This is ensured by an adapted design including a large compression ratio (ratio of displaced volume to dead volume in the pump chamber [13]). A high ratio can be achieved by a specific mounting procedure for the piezo ceramic: a voltage, applied during glue hardening, causes the actuator diaphragm to permanently bulge out, creating the pump chamber [14]. The achieved compression ratio leads to a high pressure build-up with air and enables bubble tolerance.

Microvalves are an important additional component for implantable applications, for instance as a safety measure. Based on different actuation methods, e.g., piezoelectric, shape memory alloy, electrostatic, or magnetic, various types of microvalves have been developed [15,16]. The two basic groups of valves are normally closed (NC) and normally open (NO) valves. NC valves block the fluidic path, only opening when actuated. By contrast, NO valves allow flow while not actuated and are actively closed. Both types offer adapted properties for different applications. Examples of piezoelectric valves are presented in research [17–19]. Water leakage rates as low as 0.013 μL/min [20] and water free flow of up to 8.75 mL/min [21] are achieved. In contrast to existing microvalves, we want to combine low leakage of a soft sealing on a solid valve seat with a large free flow operating range. Valves are designed to benefit from the high force and fast response time abilities of piezoelectric actuation, which allows their usage in challenging flow conditions such as high differential pressure.

Fluidic conditions are not the only demanding aspect in microfluidic systems. The electrical system needs to be hermetically sealed from the fluid path to prevent damage. Use within the human body requires additional sealing, and every material in contact with tissue has to be biocompatible. Metal pumps, such as stainless steel pumps [22,23], offer welding as possible hermetic sealing. However, stainless steel has a large disadvantage when it comes to long-term medical implants: this material causes artifacts in magnetic resonance imaging (MRI) scanning, as evaluations on different implants have shown [24–26]. A suitable material to solve this issue is titanium, which offers numerous advantages for use in medical applications [27] in addition to its MRI compatibility: When exposed to air, its surface forms biocompatible and antibacterial titanium dioxide [28,29]. Titanium components can be hermetically sealed from the human body, e.g., by welding titanium covers to them [30]. Since no different materials are bonded together, the risk of galvanic corrosion is minimized [31]. So far there are examples of micropumps and valves partly manufactured of titanium [32–35].

In our work, we develop a titanium platform of microfluidic devices for medical implants. It includes new designs of a NO valve and a NC valve, making use of the beneficial properties of titanium. In addition, we adapt the proven design of known steel micropumps [22] to titanium. The small and light devices are designed to allow easy integration into efficient products. These automated solutions aim to increase patients' comfort.

2. Micropump and valve design

Hydraulic actuators usually rely on a combination of pumps and valves. For microfluidic implants, many combinations are imaginable and design strongly depends on the exact use case. Fig. 1 depicts a generalized fluidic setup for hydraulic actuation. The pump actively transports fluid from P1 to P2 and builds up a pressure, while an active valve maintains or releases the pressure as needed. P1 and P2 are volumes that can either be the hydraulically actuated part or a fluid reservoir. In case of a malfunction such as the loss of power, the implant has to remain in a safe state, where any critical pressure is released to prevent risk of injury. Therefore, depending on the exact design, e.g., a pressurized or non-pressurized reservoir, the use of a NO or NC valve is required. A NO valve ensures pressure release in non-actuated state, for a hydraulically actuated volume at P2 where a permanently applied pressure can cause injury. Whereas if a constant pressure is unproblematic regarding safety aspects, a NC valve can be used to enable a more energy efficient use.

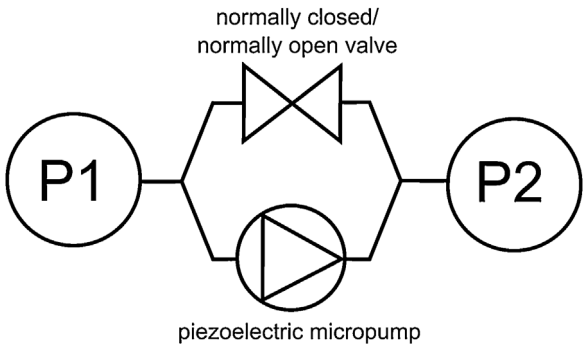

Fig. 1. Fluidic setup of a hydraulic actuation unit. The pump transports fluid between a reservoir and the actuated part, which are depicted as P1 and P2 here. The valve can maintain and release the built up pressure as required. Different working principles achieved with alternative circuit arrangements are possible. The decision for a normally closed or a normally open valve depends, among others, on safety aspects, since a pressure release of the actuated part in the case of power loss is often necessary.

In general, piezoelectric actuation allows for energy efficient driving (v.i., "Experimental Results and Discussion") [9]. Even a NO valve, operated to be closed most of the time, does not require excessive energy, since the piezoelectric ceramic acts as a capacitance and leakage currents are low. Hence, the applied voltage remains stable over long periods. Therefore, this titanium technology platform enables the development of space and energy efficient products.

For easy combination, we design the three devices to use the same actuation principle, be manufactured in similar processes, and be geometrically alike. Titanium and FKM, the wetted materials of the microfluidic devices developed, were sourced in medical grade. Those materials exhibit beneficial traits and are already used in medical devices. However, a detailed biocompatibility testing is necessary and not yet part of this study, which focuses on the technical development. Since the hydraulic fluid system is a closed circuit setup, contact to the body does not occur during orderly function. A critical element is the piezoelectric actuator. The lead content as well as the electric contact makes hermetic sealing and electric isolation indispensable. The devices are designed to allow such sealing, e.g., by laser welding.

2.1. Titanium pump

The design of the titanium micro diaphragm pump (Fig. 2a) is similar to our steel pumps [22]. The pump includes a titanium body in combination with a glued on piezoelectric disc actuator (PIC 151, d = 16 mm; 200 μm) (Fig. 2c). The body consists of a base plate and three titanium foils: two valve foils and one actuator foil. All metal parts are laser welded to form the impermeable pump chamber. The current device has a diameter of 20 mm and a height of 1.5 mm.

Pumping bases on the indirect piezoelectric effect, causing a mechanical deformation when the piezoelectric ceramic is exposed to electrical actuation. Hence, applying an alternating high voltage signal results in an oscillating vertical diaphragm deflection

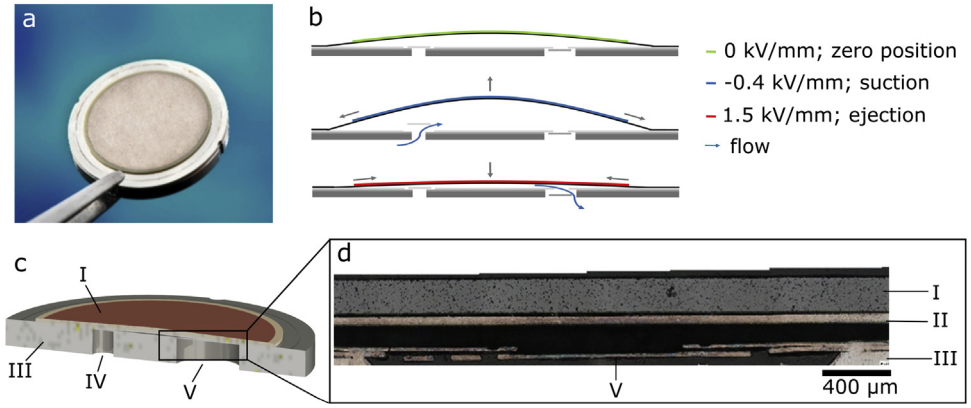

Fig. 2. **a** Picture of a piezoelectric titanium micropump. **b** working principle. Due to the indirect piezoelectric effect, an alternating high voltage causes an oscillating movement of diaphragm. In combination with two passive spring valves, this leads to an effective flow. **c** model of the pump showing the piezo actuator (I), the pump body (III), the inlet (IV) and outlet (V). **d** section of the outlet valve (V) welded to the pump body (III) with piezo ceramic (I) glued to the actuator diaphragm (II).

and creates a fluid movement through two passive spring valves (Fig. 2b).

The pretension technique [36] for piezo mounting promotes a high pumping performance. The ceramic is exposed to a defined electric field while curing the glue. Therefore, bonding takes place in a contracted state of the piezo. After curing, the voltage is removed and the expansion of the ceramic bulges out the pump chamber. This specific mounting establishes a large compression ratio (displaced volume / dead volume) and therefore leads to self-priming and bubble tolerant pumps up to at least 30 kPa.

2.2. Normally open valve

The design of the titanium NO valve is similar to the titanium pumps, though the passive check valves are omitted (Fig. 3a). The bending actuator is a 100 µm titanium foil with a glued on piezo ceramic (PIC 151, d =16 mm; 200 µm). It is laser welded to the valve body, which includes two drilled openings for valve inlet and outlet. An O-ring soft sealing (medical grade FKM, nominal thickness of 500 µm), integrated into the valve body before laser welding, enables low leakage rates. The current device has a diameter of 20 mm and a height of 2.6 mm.

During non-actuated mode, fluid can pass through the clearance between the soft sealing and actuator membrane of the NO valve (Fig. 3). Exposure of the piezo ceramic to an electrical field causes a deflection towards the valve chamber bottom. Eventually, the diaphragm compresses the O-ring and blocks fluid movement (Fig. 3b). The pretension technique for piezo mounting is the driving factor for the valves' fluidic performance in its open state. It adjusts the chamber height and therefore determines the valve's fluidic resistance. Blocking is ensured as long as the actuator's force is greater than the force introduced to the membrane by fluid pressure. The NO valves use the same bending actuator as the titanium pumps and therefore overcome a minimal pressure of 80 kPa.

2.3. Normally closed valve

While the overall setup of the normally closed valve is more complex (Fig. 4a and b), its bending actuator is the same as for the pumps and NO valves. The NC valve includes an O-ring (medical grade FKM, nominal thickness of 500 µm) that is integrated into the valve's body. The soft sealing is compressed by a plunger, suspended by a 50 µm thin spring foil that pulls it upwards. The current device has a diameter of 20 mm and a height of 3.6 mm.

For manufacturing, the plunger is inserted in the valve body from beneath, bringing it into contact with the soft sealing. The spring foil is welded to the plunger and subsequently to the valve body. A difference in height of the two weld planes causes the initial pre displacement of the spring foil, which pulls the plunger upwards and compresses the soft sealing. The pre displacement is designed to be 100 µm, adding up the difference in height of the plunger and the valve body, and the soft sealing's elevation. The valve body, the plunger, and the spring foil form the impermeable valve chamber. Finally, the actuator foil is laser welded to the valve body.

Blocking of the flow in non-actuated mode is ensured due to the spring foil's restoring force (Fig. 4c). Moreover, a pressure acting on either the spring foil or the plunger induces an additional closing force. Therefore, a fluidic pressure applied on either the valve's inlet or outlet increases sealing of the double normally closed valve. A high voltage on the bending actuator causes the diaphragm, and therefore the plunger, to move downwards. The plunger loses contact to the soft sealing and opens the fluid path (Fig. 4c). Opening takes place as long as the actuator's force is greater than the restoring force of the spring foil.

The initial spring force displacement is crucial for a functioning device, since it determines the balance of sufficient opening in actuated state and low leakage in closed mode. Therefore, the elastic behavior of the spring foil is investigated experimentally

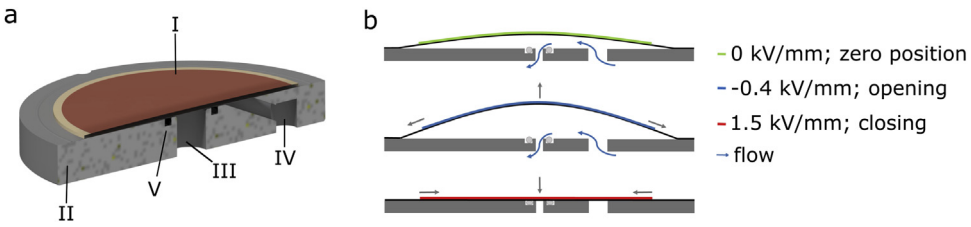

Fig. 3. **a** Model of a normally open valve showing the bending actuator (I), the valve body (II), the outlet (III) and inlet (IV) as well as the FKM sealing (V). **b** working principle. In the non-actuated state, the diaphragm hovers over the sealing, allowing for fluid flow. Using the indirect piezoelectric effect, the valve can be actively opened, further decreasing its fluidic resistance, or actively closed, using a high positive voltage to compress the sealing.

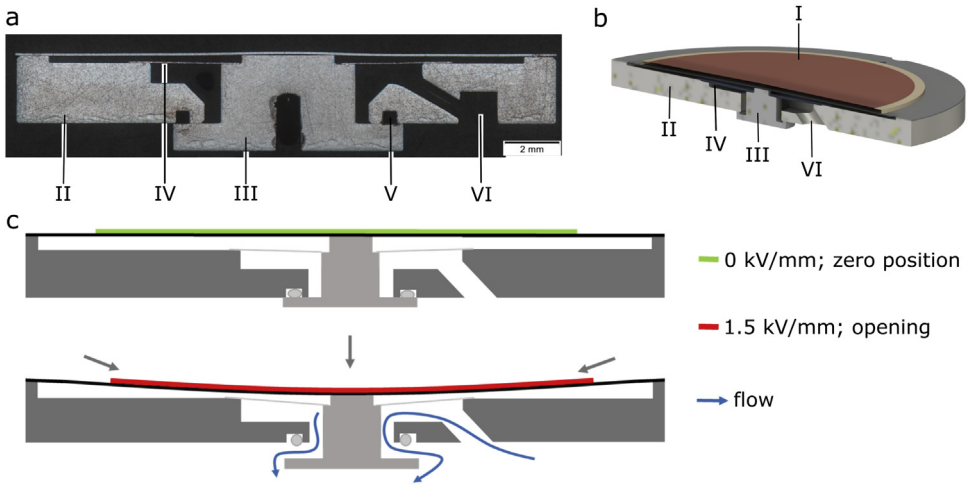

Fig. 4. **a** Section of a normally closed valve showing the valve body (II), the plunger (III), the sealing notch (V) as well as the inlet of the valve (IV).The plunger (III) is welded to a spring foil (IV) and compresses a FKM sealing in the notch (V). **b** model of the valve including the glued on piezo actuator (I). **c** working principle. In non-actuated state, the spring foil pulls the plunger up, closing the valve's outlet. The indirect piezoelectric effect causes the actuator diaphragm to move downwards when a high voltage is applied, which opens the fluid path.

and with finite-element-modelling (FEM) simulation. By variation of the initial spring displacement its effect on the spring force is determined.

3. Materials and methods

For assembly of the novel micropump and valves, we use solely titanium, since it offers high resistance to plastic deformation and is commonly used in medical applications [37]. Rigid parts, such as the pump/valve body, or the plunger of the NC valve, are manufactured using high precision milling. The structured foil components are etched from cold-rolled titanium sheet material of different thicknesses (from 25 μm to 100 μm). Inspecting the topologies of all components ensures flatness of foils, surface smoothness of milled parts, and compliance with geometric requirements. For assembly, foil components are welded to the pump/valve bodies using a fiber laser. The parts are aligned with dowel pins and firmly pressed together to ensure a high-strength bond resulting in hermetic sealing of the devices' chambers. After laser welding, piezo ceramics are mounted using a two-component epoxy glue.

3.1. Stroke measurements

The stroke measurement describes the optical detection of the diaphragm displacement using a quasi-static voltage (amplifier SVR 500−3, piezosystem jena GmbH). Exact movement is determined with a white light profilometer (Fries Research and Technology). The optical sensor has a range of 3 mm and a maximal resolution of 30 nm. The applied voltage passes through the whole range of interest several times to detect the hysteresis as well as initial repolarization of the ceramic. The measurement automation ensures that the time between two recorded voltages is kept constant, minimizing piezoelectric time effects as sources of error. The measurement accuracy of the total actuator stroke is 2 μm, as evaluated from repetitive measurements of several samples.

Furthermore, displacement measurements investigate the NC valve's initial spring tension and elastic behavior. We manufactured four samples specifically for this measurement. The plunger of the valve is not covered with an actuator membrane and can therefore be accessed directly by an applied pressure. A pressure controller (Mensor CPC3000: range -0.5 bar to 2 bar, accuracy: ±0.5 mbar) applies an increasing pressure to the top side of the spring foil, thus forcing a movement of the plunger that is detected optically.

3.2. Fluidic test

We conduct fluidic characterization for each manufactured sample using DI water at room temperature. The sensors used are: Coriflow sensors of different ranges (Bronkhorst MINI CORI-FLOW M14: range 0.5 mL/min to 167 mL/min, accuracy: ± 0.2% and ML120V00: range 0.8 μL/min to 500 μL/min, accuracy: ± 0.2%); a pressure controller (Mensor CPC3000; v.s.) and two piezoresistive pressure sensors (EPCOS Gauge pressure transducers AKR 1.000 C40: range 0.0 bar–1.0 bar, accuracy: ±6 mbar). The latter are placed in the flow path to evaluate the pressure drop over the sample. It is important to notice that the use of coriflow sensors depicts an additional flow resistance in the fluidic path and therefore diminishes the achievable flow rate. Thus, the presented results are the minimal achievable performance.

Micropumps are fluidically characterized by their frequency dependent flow rate at zero backpressure, their pressure dependent flow, and leakage. For evaluations of the frequency dependent flow rate, the pump is actuated with a sinusoidal actuation of -0.4 kV/mm to 1.5 kV/mm. A frequency sweep from 5 Hz to 80 Hz is conducted and the resulting flow recorded after stabilization. All experiments are realized using the same setup, since any changes in the periphery can cause large differences in fluidic performance. Furthermore, pressure dependent flow with 30 Hz sinusoidal actuation is measured. A linear extrapolation of the data enables calculation of the theoretical blocking pressure. We shorten measurement time of the large number of samples by omitting experimental investigations of the blocking pressure. In addition to active flow, we evaluate leakage through the passive check valves with pressure up to 40 kPa.

Fluidic testing of microvalves includes testing of the actuated and non-actuated mode. In our experiments, valves are actuated using a sinusoidal signal with a frequency of f =0.01 Hz and electric fields of -0.4 kV/mm to 2.0 kV/mm. We evaluate the pressure dependent characteristics of an actuated valve for closing and opening lead times. For both actuated and non-actuated valve testing, an applied head pressure is varied using a pressure controller. During open valve testing, the fluid pressure allows a flow through the valve and the flow rate dependent on the electrical field is mea-

sured. For closed valve testing, the pressure dependent leakage through the valve is tested.

3.3. Simulation

For investigation of mechanical tension within the foil components of titanium devices, ANSYS workbench 2019 R1 is used for FEM analysis. Non-linear analysis of large-deformation loads on thin foils is conducted for evaluation of pressure-induced deformations in the elastic regime. This data is compared to mechanical evaluation and crucial for further valve development.

3.4. Data statement

The actuator stroke, fluidic test, and simulation data that support the findings of this study are available in Fordatis – Research Data Repository of Fraunhofer-Gesellschaft with the identifier [https://doi.org/10.24406/fordatis/74] [38].

4. Experimental results and discussion

Medical applications, such as hydraulic implants, require very specific fluidic characteristics. A detailed experimental evaluation is necessary to adapt devices to those requirements and improve the pump and valves further. Table 1 provides an overview of the introduced devices and their fluidic characteristics described hereafter.

4.1. Titanium pump

To assess the titanium pumps' performance, we manufactured a batch of our known steel pumps in parallel to titanium samples and compare the obtained results.

The actuator stroke of a micro diaphragm pump determines the displaced volume per actuation cycle. Optical stroke measurements serve as initial function tests and enable the detection of a touchdown of the diaphragm to the pump chamber bottom, caused by deviations during the piezo mounting process. Fig. 5a displays an example of a titanium pump stroke measurement. The quasi-static actuation is applied from 0.4 kV/mm to 2 kV/mm, covering the operating range as well as an additional positive voltage range for potential touchdown detection. The piezoelectric hysteresis is clearly visible.

The stroke of 24 titanium samples is (79.2 ± 4.3) µm. It is compared to 24 steel pumps' average stroke of (79.8 ± 2.9) µm (Fig. 5b). None of the overall 48 samples exhibit a touchdown. Titanium and steel actuator foils have a thickness of 100 µm. Since titanium is more flexible than steel (Young's modulus of $E_{Ti\text{-}foil}$ =112 GPa compared to $E_{Steel\text{-}foil}$ =195 GPa [39,40]), one expects a higher actuator stroke. Using considerations of Herz et al. [41], we calculated the theoretic difference as approximately 7 µm. Nevertheless, we cannot detect this difference. Other influences such as variations during laser welding, piezo mounting, and deviations in the raw material overlay the influence of the Young's modulus. For instance, incoming goods inspection of the used piezo lot reveals an average thickness of (202 ± 2.8) µm, capacitance of (21.9 ± 0.6) nF and weight of (314 ± 4.4) mg. Comparison of each individual piezo characteristic and device performance reveals no direct dependence. This is due to the sample size of 48 devices, which does not allow to differentiate all influencing parameters.

Fig. 5c shows the measured flow rate of titanium and steel pumps. Both show an initial linear frequency dependence of the flow. Within the linear range, the average flow rate of titanium and steel pumps is alike and reaches up to 11 mL/min. Non-linear behavior starts at approximately 30 Hz, where the inertia of the fluid and passive check valves limits further linear increase and causes a decrease of flow for even faster actuation. The maximal flow is higher for titanium pumps with (14.2 ± 2.5) mL/min compared with (12.2 ± 2.2) mL/min for steel pumps. However, error bars of both groups overlap. The cause for the deviation in maximal flow rate without any difference in the linear regime is not yet solved conclusively. A hypothesis is that the increased elasticity of the spring valves due to the change in material can lead to higher flow rates as inertia effects are less pronounced. It is important to note that the maximal flow strongly depends on the fluidic periphery and pump comparison should always take place in the linear regime.

The flowrate of diaphragm pumps does not only depend on the actuation frequency but also on the applied backpressure. A fixed actuation with increasing backpressure shows a linear decrease in flow (Fig. 5d). Titanium and steel pumps behave very similarly. The extrapolated blocking pressure is approximately 75 kPa. An ideal pump's flow rate is backpressure independent, which can be achieved in further development steps, e.g., with design adaptions [42]. Here, the backpressure dependent flow gives additional information on the micropump's quality. While a pump with poor valves can show reasonable flow without any backpressure, its behavior with pressure is usually deficient. Especially bubble tolerance can suffer, if valves are insufficiently closed. Leakage measurements give further insights on the valve quality. The titanium samples show an average leakage of (0.05 ± 0.04) mL/min with 5 kPa applied to the pumps outlet. This is similar to the steel pumps' leakage of (0.04 ± 0.01) mL/min.

Some characteristics of the individual devices show large variation. While the actuator stroke has a variance of 5%, the flow rate error reaches up to 20% (Fig. 5) and the leakage shows a large scattering with a deviation of up to 80%. The stroke variation can be caused by deviations in raw material characteristics and geometry, such as the piezo characteristics mentioned above. The notably larger scattering of the flow rate is likely due to differences in the valve quality. This hypothesis is substantiated by the extreme scattering of the leakage measurement. A deformed valve that causes large leakage rates allows backflow during the pump stroke and limits the fluidic performance. Such a deformation can be caused by the raw material quality as well as occur during the laser welding process due to heat effects. Not all crucial influences are fully understood yet. We aim to minimize the sample to sample variation in further development steps, considering each individual influence.

The power consumption of the bending actuator is experimentally determined on the pump samples to be 2 mJ/stroke with no dependency on the frequency in the relevant range up to 100 Hz or backpressure conditions. Hence, the pumps' power consumption depends on the frequency and the power per displaced volume depends on the applied pressure. Without applied backpressure, titanium and steel pumps have an energy requirement in the linear regime of 330 J/L. The maximal flow in the non-linear regime requires 420 J/L for titanium pumps and 440 J/L for steel pumps. The resulting power consumption only includes the piezoelectric actuation, while the efficiency of the driving electronics needed to actuate the devices is not taken into account. In general, piezoelectric pumps are considered energy efficient compared to other actuation types [43], however, few authors give exact information. The presented actuator proves to be energy efficient compared to other piezoelectric pumps that require 900 J/L [44] or 1400 J/L [45]. The only pump that requires less energy per displaced volume known to the authors bases on electrostatic actuation and is designed for smaller flow rates and lower backpressure [46].

4.2. Normally open valve

Equivalent to micropump stroke testing, NO valves are tested with a quasi-static actuation from -0.4 kV/mm to 2 kV/mm. Piezo-

Table 1
Overview of design parameters and experimental results of the introduced devices.

	Titanium Pump	Stainless Steel Pump	Normally Open Valve	Normally Closed Valve
Number of tested samples	24	24	24	3
Size in mm³	Ø20 × 1.5	Ø20 × 1.5	Ø20 × 2.6	Ø20 × 3.6
Driving Voltage in V	−80 to 300	−80 to 300	−80 to 500	−80 to 400
Frequency in Hz	up to 80	up to 80	not applicable	not applicable
Actuator stroke in µm	79.2 ± 4.3	79.8 ± 2.9	57.3 ± 6.3	39.9 ± 4.0
Energy consumption in J/l (linear regime)	330	330	not applicable	not applicable
Energy consumption in J/l (maximal flow rate)	420	440	not applicable	not applicable
Maximal flow rate in ml/min	14.2 ± 2.5	12.2 ± 2.2	not applicable	not applicable
Extrapolated blocking pressure in kPa	75	75	not applicable	not applicable
Leakage at 5 kPa backpressure in µl/min	50 ± 40	40 ± 10	3.4 ± 6.3	2.6 ± 1.9
Open state flow at 20 kPa in ml/min	not applicable	not applicable	27.5 ± 5.3	9.0 ± 9.5
Leakage at 20 kPa in µl/min	not applicable	not applicable	10.9 ± 28.1	0.36 ± 0.15

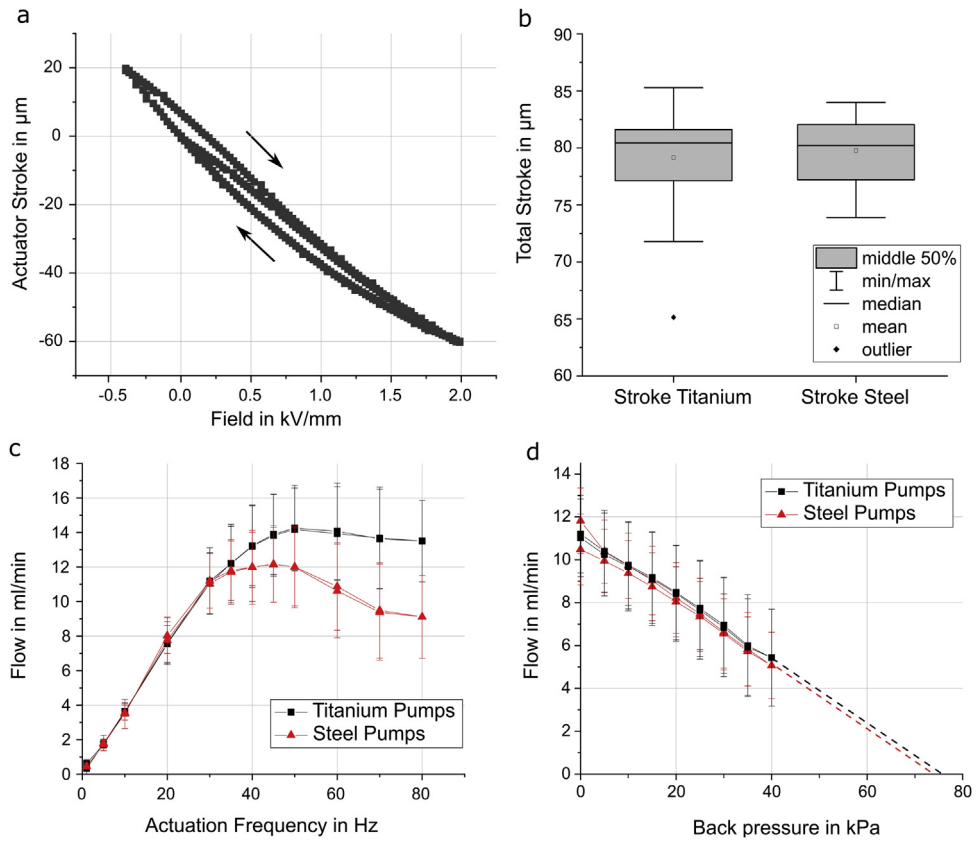

Fig. 5. **a** Typical stroke measurement of a titanium pump. The piezoelectric hysteresis is visible and no touchdown to the pump chamber bottom is detected. **b** box-plot for stroke comparison. The change in material does not cause a change in stroke. **c** average frequency dependent flow rate with no backpressure and sinusoidal actuation of -0.4 to 1.5 kV/mm ($n_{Titanium}$ = 24, n_{Steel} = 24). Both pump types show the same behavior in the linear flow regime. Error bars depict the standard deviation. **d** backpressure capability ($n_{Titanium}$ = 24, n_{Steel} = 24) with sinusoidal actuation of 30 Hz and -0.4 to +1.5 kV/mm. The extrapolated blocking pressure is 75 kPa and does not change with a change in material. Error bars depict the standard deviation.

electric hysteresis as well as the re-polarization initial curve are visible (Fig. 6a). The overall stroke of 24 NO valves is (57.3 ± 6.3) µm. The mechanical blocking of the actuator diaphragm due to the O-ring is clearly visible at approx. 1.3 kV/mm (Fig. 6a). The variance of the stroke is larger for the NO-valves as for the pumps, since the mechanical blocking on the O-ring limits the actuator movement. Due to deviations in O-ring thickness, this actuator blocking occurs at lower or higher actuation voltage.

Fluidic testing of the NO valve includes flow characterization with dynamic actuation (0.1 Hz, sinusoidal waveform) as well as leakage testing with a constant electric field. Fig. 6b shows the opening and closing characteristics of an exemplary NO valve during actuation with 20 kPa head pressure. A strong hysteresis of the passive flow through the valve occurs during actuated mode, which is caused by the piezoelectric hysteresis already observed in stroke measurements, as well as transient flow mechanisms causing fluidic hysteresis. When the electrical field starts to increase from a negative value, the valve is starting to close from its fully opened state. With a high velocity fluid flow being present at full opening, the dynamic pressure within the valve chamber is low during this flow phase. Compared to the opening operation of the valve with a decreasing electrical field, the pre-existing flow field exhibits low velocities and high dynamic pressures. Therefore, the dynamic pressures being present in the valve are different during opening and closing operation, resulting in different flow rates at the same head pressure. The average maximum passive flow of 24 samples is (27.5 ± 5.3) mL/min.

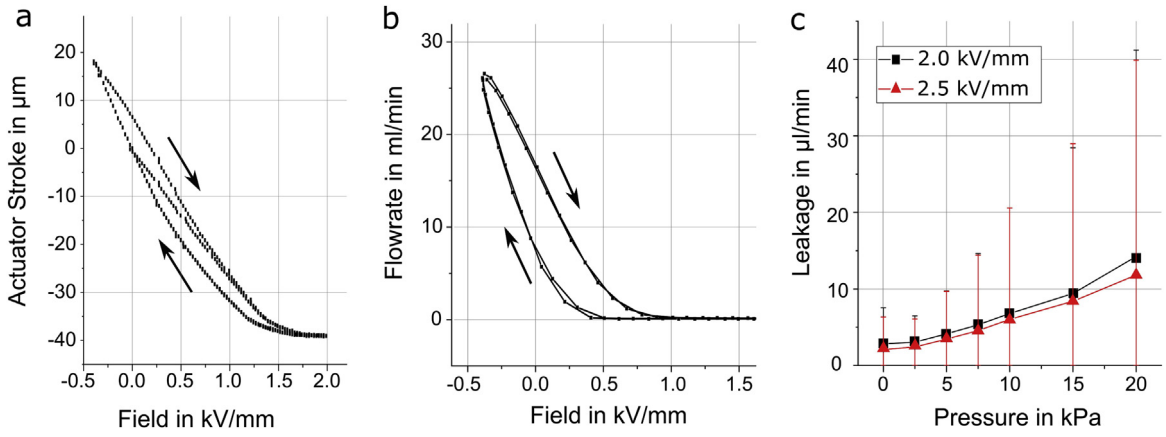

Fig. 6. **a** Typical stroke measurement of a normally open valve. A change in slope is visible at approximately 1.3 kV/mm, when the actuator starts to compress the O-ring creating a large counter force. **b** typical flow characteristic of a normally open valve with 20 kPa head pressure showing complete blockage at approximately 1 kV/mm. Active opening (negative voltage applied) allows a flow of 26 mL/min. **c** average pressure dependent leakage rates of 24 actuated valves at 20 kPa head pressure. Error bars show the standard deviation.

During leakage characterization of NO valves, the actuation field further extends towards positive voltages up to 2.5 kV/mm. This additional field increases the compression of the O-ring by deflecting the diaphragm further. Fig. 6c shows the pressure dependent leakage rates of 24 samples at 2.0 kV/mm and 2.5 kV/mm. The leakages through the tested valves are less than 50 µL/min in the tested pressure range of up to 20 kPa. With an electrical field of 2.0 kV/mm applied, the maximum leakage rate observed is (14.8 ± 27.4) µL/min, while the maximum leakage at 2.5 kV/mm is (10.9 ± 28.1) µL/min. The large sample to sample variation can be caused by geometric differences of the used O-ring. As later characterization shows, the thickness of the O-rings in the used batch varies strongly with (495 ± 33) µm. To further improve leakage rates, the inspection of individual O-rings is planned in future development steps.

4.3. Lifetime investigation normally open valve

An investigation of the piezo lifetime was conducted for micropumps in previous studies [23]. Lifetime evaluations in this study include two devices (NO valve 1 and NO valve 2) to gain first insights whether a shorter lifetime of NO valves is to be expected due to additional mechanical stress (touchdown on the O-ring) compared to micropumps.

A failure due to piezo cracking is detected optically and electrically by measuring the samples' capacitance. A crack decreases the capacitance significantly, since only the electrically contacted part of the piezo is detected.

Prior to life time evaluations, the valves are characterized regarding actuation behavior and leakage. All life time tests are conducted on samples filled with water, and without applied pressure, using sinusoidal actuation, with an electrical field of (-0.2 to +1.9) kV/mm. The valves are actuated at frequencies of [0.1; 1; 2; 10; 20; 50; 100; 275] Hz and 10^4 cycles are driven per frequency step. After each frequency, the capacitance is measured. Finally, the NO valves are driven at 100 Hz until a total amount of one million cycles. Piezo failure was not detected and capacitances remained constant at (14.9 ± 0.2) nF and (15.8 ± 0.3) nF (NO valve No. 1 and No. 2, respectively). Valve performance testing is repeated including stroke measurements, as well as actuation and leakage testing at 20 kPa head pressure. For NO valve No. 2, the change in performance is < 5% (total stroke, leakage rate at p = 20 kPa), whereas the stroke of NO valve No. 1 decreases by 30% and leakage at 20 kPa increases by 100% compared to results right after assembly. The different behavior after lifetime testing is assumed to be under the influence of thickness variation among the O-rings used within the NO valves. For future studies, geometric characterization of the soft sealing in the valves is implemented in order to find correlations to the phenomena observed.

4.4. Normally closed valve

In initial testing, many of the manufactured NC valves showed to be non-functional, since even with high actuation voltages no open state was reached. During failure analysis, we examined the used O-rings regarding their thickness. Their mean thickness deviates significantly from the nominal value of 500 µm and shows large sample-to-sample variation with an average of (585 ± 45.4) µm. Moreover, slightly compensating the increased O-ring thickness, the corresponding sealing notch depth is 50 µm larger as designed. The initial spring displacement is therefore higher than the targeted value of 100 µm, which causes an increase of the spring force and subsequently an imbalance of the forces in the mechanical system. Consequently, the piezoelectric actuator's force is too low to open many of the manufactured valves.

The three functional NC valves are tested for stroke and fluidic performance. Overall stroke of the three NC valves is (39.9 ± 4.0) µm with a quasi-static actuation of 0.4 kV/mm to 2 kV/mm. Fig. 7a shows a typical stroke measurement of one exemplary valve. The slope is steep for negative voltages, where the actuator diaphragm is not in contact with the plunger. This part of the curve characterizes the mechanical behavior of the bending actuator. A change in slope occurs at the touchdown of the diaphragm to the plunger (Fig. 7a). The counter force of the spring foil attached to the plunger reduces possible movement.

Fluidic testing of the NC valve includes flow characterization with actuation as well as leakage testing during non-actuated mode at 20 kP head pressure. Leakage through all three tested valves is less than 1 µL/min with an average of (0.36 ± 0.15) µL/min. This is in good accordance with the designed high O-ring compression enabling a tight seal. Fig. 7b depicts the opening and closing characteristics of a NC valve in actuated mode. Same as for NO valves, a fluidic hysteresis occurs due to piezo hysteresis and dynamic pressure differences. The average maximum flow of three samples at 20 kPa head pressure is (9.0 ± 9.5) mL/min.

4.5. Spring foil investigation normally closed valve

The elastic deformation of the NC valve's spring foil is crucial for its functionality. Therefore, we conduct an experimental and

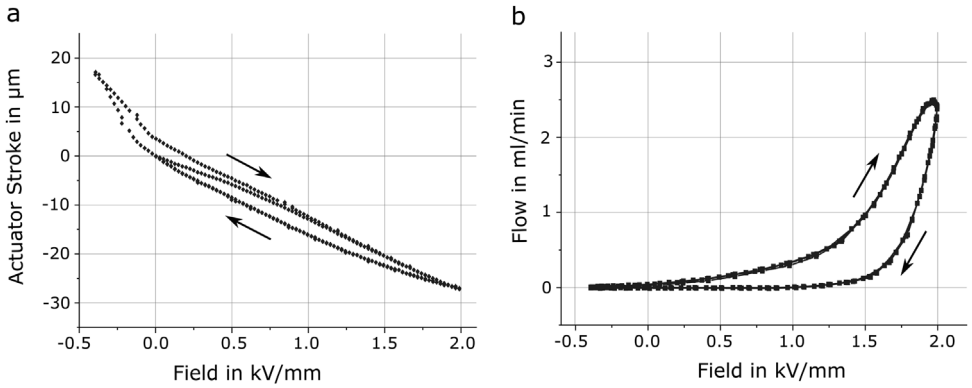

Fig. 7. **a** Typical stroke measurement of a normally closed valve. A change in slope is visible at approximately -0.2 kV/mm, when the actuator diaphragm loses touch to the plunger. **b** typical flow characteristic of a normally closed valve at 20 kPa pressure difference showing a blockage of the fluid flow up to 0.25 kV/mm and a maximal flow in open state of 2.5 mL/min with 20 kPa pressure applied.

numerical investigation. A comparison of the data enables targeted design changes to achieve desired opening and leakage behavior.

A half model of the spring foil (thickness of 50 µm) is investigated and a fine, structured hexagonal mesh is implemented (Fig. 8a). A pressure load is applied to the inner area, which is the interface of the spring foil and the plunger (Fig. 8b). This inner area (C, yellow), which is welded to the plunger, can solely move in z direction, while movement in x or y direction is suppressed in order to comply with the physics of the weld. The area of the outer weld line connecting the foil to the valve body is defined as a fixed support (A, blue). It is restrained in all six degrees of freedom. Boundary condition B (red) is the applied pressure load that leads to a displacement by elastic deformation of the structure. Fig. 8c shows the deformation in true scale, with z-displacement presented in false color.

We evaluate the spring foil deformation under pressure load with regard to an initial spring displacement (Fig. 8d). The dotted curves show the pressure dependent behavior starting at a given displacement by forcing an inner ring position in order to imitate the initial displacement during manufacturing. The solid line depicts experimental results. It is evident from the FEM data that the displacement depends strongly on the initial spring displacement after laser welding. Higher initial displacement leads to stiffer behavior of the foil.

Experimental data is in good agreement with the FEM data assuming a 120 µm initial spring displacement. The increased O-ring elevation of 35 µm can cause such a shift from the designed 100 µm initial displacement to 120 µm when assuming O-ring compression, which was not individually evaluated for each device in this study. The total stroke of the spring foil at 100 kPa pressure load is below 20 µm for a high initial spring displacement (120 µm) in numerical evaluations as well as for experimental results. Such a low displacement of the spring foil and the plunger leads to a low decompression of the O-ring, not opening the valve. Further improvement of the design and adaptation of O-rings is necessary. A displacement of 40 µm or more, which allows full opening, in the blocking pressure range of the piezoelectric actuator of roughly 80 kPa is possible for an initial spring displacement of 50 µm. Therefore, design parameters need adaptation towards lower initial spring tension.

5. Conclusion

This work summarizes the development and evaluation of a titanium based microfluidic platform for medical applications. The combination of the piezoelectric micropump, a NC as well as a NO microvalve offers many possibilities to develop small and energy efficient implants with broad functionality and automated control instead of manual operation.

The titanium micropumps show promising results. With (79.2 ± 4.3) µm, their stroke height is similar to comparable steel pumps showing (79.8 ± 2.9) µm of stroke. The flow characteristics of both pump types are alike, which matches their similar stroke. Within the linear regime, the novel titanium pumps reach an average flow of (11 ± 2) mL/min. The average maximal flow of the 24 samples is (14.2 ± 2.5) mL/min and thereby 2 mL/min higher than the one of the steel samples. The backpressure capability is also very promising, showing an extrapolated blocking pressure of 75 kPa.

In this work, we also describe the development and evaluation of new titanium NO valves. Even though they use the same actuator, the valves show a smaller stroke of (57.3 ± 6.3) µm as compared to the titanium pumps, since a touchdown to the O-ring blocks further membrane movement. Leakage rates of all 24 samples are in an acceptable range below 50 µL/min. The sample-to-sample variation of leakage is rather high with an average of (10.9 ± 28.1) µL/min. Further improvement to minimize variations is necessary and possible. Nonetheless, already good closing behavior is achieved and many samples exhibit low leakage, proofing the feasibility of this device. Free flow is evaluated for 20 kPa head pressure, which is a realistic pressure the pump easily provides. The high flow of (27.5 ± 5.3) mL/min displays a low flow resistance, which is important for efficient system architecture.

In the NO valve, premature failure can occur due to the touchdown of the actuator membrane on the O-ring, which causes a different strain distribution within the piezo ceramic compared to the pumps where the membrane can move freely. Preliminary lifetime tests on two samples showed no piezo failure within one million cycles. However, fluidic performance changed unreproducibly, making further design considerations and lifetime testing necessary.

Manufacturing of functional NC valves posed problems, since extremely low tolerances of all parts are necessary. The large deviation in O-ring thickness observed leads to a too high initial spring tension acting on the plunger and a resulting high spring force countering piezo-actuator movement. Therefore, only three out of thirty samples showed valve functionality, while all others stayed constantly closed. Comparison of measured O-ring thicknesses and FEM simulation are in good agreement and indicate that slight design changes can increase the yield of working valves tremendously. The three functioning samples show very promising results. Leakage in closed (non-actuated) mode is extremely low with (0.36 ± 0.15) µL/min.

The introduced titanium platform offers great possibilities for microfluidic applications, especially in the medical field. The pre-

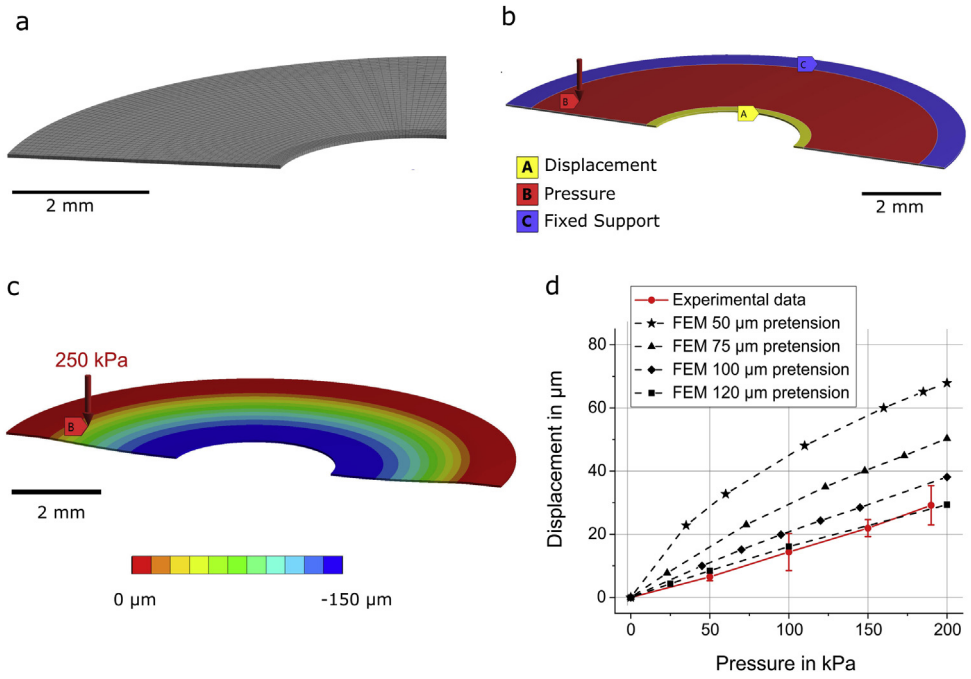

Fig. 8. **a** Half model of the spring foil with structured mesh. **b** boundary conditions. The outer ring (C) is set as fixed support and the displacement of the inner ring (A) is evaluated with a given pressure applied to area B. **c** deformed model in true scale for a pressure of 250 kPa. **d** experimental and FEM results of the spring foil's displacement under pressure load. With 50 µm initial displacement, the numerical solution differs strongly from the experimental results, while a calculation using 120 µm pre-displacement shows fitting results.

sented pump combines high flow rates with high backpressure abilities. We designed and tested microvalves with low leakage rates and high free flow, making them suitable for reliable flow restrictors with low fluidic resistance in open state. Additionally, we showed possibilities for further improvement. All devices consist only of titanium, FKM sealing, and a glued on piezo ceramic, achieving MRI-compatibility. In addition, compatibility with a large variety of fluids is given since all wetted surfaces are titanium or FKM. Especially for medical applications, energy efficiency can be a crucial property. Piezoelectric actuation offers an energy efficient as well as space saving actuation method for both pumps and valves. Furthermore, the similar form factor of the devices enable easy and space efficient combination. The choice between NC and NO valves makes it possible to design well-adapted systems with the lowest possible energy consumption. The introduced devices are the base of a microfluidic titanium-based technology platform. The aim of future research is to further develop existing devices and extend the functionality of the platform further.

CRediT authorship contribution statement

Agnes Beate Bußmann: Conceptualization, Data curation, Formal analysis, Investigation, Methodology, Project administration, Resources, Validation, Visualization, Writing - original draft, Writing - review & editing. **Claudia Patricia Durasiewicz:** Data curation, Formal analysis, Investigation, Methodology, Project administration, Resources, Validation, Writing - original draft, Writing - review & editing. **Sebastian Heinrich Alexander Kibler:** Funding acquisition, Supervision, Methodology, Validation, Writing - review & editing. **Christian Klaus Wald:** Funding acquisition, Methodology, Supervision, Validation, Writing - review & editing.

Declaration of Competing Interest

The authors report no declarations of interest.

Acknowledgements

This work was partly funded by the "Bayrische Forschungsstiftung" within the project "Aktive, theranostische Blasenschließmuskeltechnologie" (active, theranostatic bladder sphincter technology) as well as the Federal Ministry of Education and Research [project reference numbers 16FMD01K, 16FMD02, and 16FMD03].

All authors have read and agreed to the published version of the manuscript.

References

[1] C.W. Jenke, S. Kibler, Y. Gao, A. Hollot, T. Neuhann, B. Kirchhof, B. Montag, M. Geiger, J. Neitzel, C. Kutter, M. Richter, Optimiation of a piezoelectric micropump actuator for medical application in glaucoma and phthisis therapy, Actuator 2014, 14th International Conference on New Actuators & 8th International Exhibition on Smart Actuators and Drive Systems. Conference Proceeding (2014).

[2] L. Marziale, G. Lucarini, T. Mazzocchi, E. Gruppioni, S. Castellano, A. Davalli, R. Sacchetti, D. Pistolesi, L. Ricotti, A. Menciassi, Artificial sphincters to manage urinary incontinence: a review, Artif. Organs 42 (2018) E215–E233, http://dx.doi.org/10.1111/aor.13164.

[3] H. Anhalt, N.J. Bohannon, Insulin Patch Pumps: Their Development and Future in Closed-Loop Systems, DIABETES TECHNOLOGY & THERAPEUTICS, 2010.

[4] A. Kargov, T. Werner, C. Pylatiuk, S. Schulz, Development of a miniaturised hydraulic actuation system for artificial hands, Sens. Actuators A Phys. 141 (2008) 548–557.

[5] P. Solanki, Aortic counterpulsation: C-pulse and other devices for cardiac support, J. Cardiovasc. Transl. Res. 7 (2014) 292–300, http://dx.doi.org/10.1007/s12265-014-9548-6.

[6] S. Siracusano, L. Fondacaro, E. Melega, Artificial urinary (AUS) and anal (AAS) sphincter, in: S. Siracusano, G. Dodi, M. Pennisi, C. Gozzi, A.L. Pastore, M.A. Cerruto (Eds.), Complications of Surgery for Male Urinary and Fecal Incontinence, Springer International Publishing, Cham, 2020, pp. 43–53.

[7] H.-J. Schrag, F.F. Padilla, A. Doll, F. Goldschmidtböing, P. Woias, U.T. Hopt, German Artificial Sphincter System-GASS: development of a novel and highly integrated sphincter prosthesis for therapy of major fecale incontinence based on piezotechnology, Biomed. Eng./Biomedizinische Technik 49 (2004) 273–277, http://dx.doi.org/10.1515/BMT.2004.051.

[8] M.V. Sefton, H.M. Lusher, S.R. Firth, M.U. Waher, Controlled release micropump for insulin administration, Ann. Biomed. Eng. 7 (1979) 329–343, http://dx.doi.org/10.1007/BF02364120.

[9] D.J. Laser, J.G. Santiago, A review of micropumps, J. Micromech. Microeng. (2004) R35–R64.
[10] S. Mohith, P.N. Karanth, S.M. Kulkarni, Recent trends in mechanical micropumps and their applications: a review, Mechatronics 60 (2019) 34–55, http://dx.doi.org/10.1016/j.mechatronics.2019.04.009.
[11] Y.-N. Wang, L.-M. Fu, Micropumps and biomedical applications – a review, Microelectron. Eng. 195 (2018) 121–138.
[12] A. Chandrasekaran, M. Packirisamy, Experimental investigation of cavitation behavior in valveless micropumps, J. Micromech. Microeng. 22 (2012) 125019, http://dx.doi.org/10.1088/0960-1317/22/12/125019.
[13] M. Richter, R. Linnemann, P. Woias, Robust design of gas and liquid micropumps, Sens. Actuators A Phys. 68 (1998) 480–486.
[14] M. Herz, M. Richter, M. Wackerle, Method for manufacturing a bending transducer, a micro pump and a micro valve, micro pump and micro valve, Google Patents, 2016.
[15] K. Oh, C. Ahn, A review of microvalves, J. Micromech. Microeng. 16 (2006) 13–39.
[16] J.-Y. Qian, C.-W. Hou, X.-J. Li, Z.-J. Jin, Actuation mechanism of microvalves: a review, Micromachines 11 (2020) 172.
[17] S. Zaehringer, M. Menacher, P. Kirchner, N. Schwesinger (Eds.), Design of a Normally Closed Piezoelectric Micro Valve (2010).
[18] P.V. Ramanamurthy, R. Ahrens, S. Karmalkar, Piezoelectric Microvalve, 2007, pp. 0019–5596.
[19] Eui-Hyeok E.H. Yang, Choonsup Lee, Juergen Mueller (Eds.), Normally-Closed, Leak-Tight Piezoelectric Microvalve Under Ultra-High Upstream Pressure for Integrated Micropropulsion, IEEE, 2003.
[20] T. Rogge, Z. Rummler, W.K. Schomburg, Polymer micro valve with a hydraulic piezo-drive fabricated by the AMANDA process, Sens. Actuators A Phys. 110 (2004) 206–212.
[21] S. Chen, S. Lu, Y. Liu, J. Wang, X. Tian, G. Liu, Z. Yang, A normally-closed piezoelectric micro-valve with flexible stopper, AIP Adv. 6 (2016) 45112.
[22] C. Wald, Martin Richter, Low-Cost Stainless Steel Micro Pumps for miniaturized early fire detection systems, MikroSystemTechnik Kongress 2015; 26. - 28. October 2015 in Karlsruhe; proceedings, VDE-Verl., Berlin, 2015.
[23] A. Bussmann, L. Gruenerbel, Increasing piezo micro diaphragm pump performance by optimizing piezo actuation, smart systems integration, Conference Proceedings (2019) 1–4.
[24] R. Buchli, P. Boesiger, D. Meier, Heating effects of metallic implants by MRI examinations, Magn. Reson. Med. 7 (1988) 255–261.
[25] A. Holton, E. Walsh, A. Anayiotos, G. Pohost, R. Venugopalan, Comparative mri compatibility of 316l stainless steel alloy and nickel–titanium alloy stents: original article technical, J. Cardiovasc. Magn. Reson. 4 (2002) 423–430.
[26] A. Klocke, J. Kemper, D. Schulze, G. Adam, B. Kahl-Nieke, Magnetic field interactions of orthodontic wires during magnetic resonance imaging (MRI) at 1.5 Tesla, J. Orofacial Orthoped./Fortschritte der Kieferorthopädie 66 (2005) 279–287.
[27] D.M. Brunette, P. Tengvall, M. Textor, P. Thomsen, Titanium in Medicine: Material Science, Surface Science, Engineering, Biological Responses and Medical Applications, Springer Science & Business Media, 2012.
[28] A.T. Sidambe, Biocompatibility of advanced manufactured titanium implants—a review, Materials 7 (2014) 8168–8188, http://dx.doi.org/10.3390/ma7128168.
[29] A.M. Khorasani, M. Goldberg, E.H. Doeven, G. Littlefair, Titanium in biomedical applications—properties and fabrication: a review, J. Biomater. Tissue Eng. 5 (2015) 593–619, http://dx.doi.org/10.1166/jbt.2015.1361.
[30] G. Jiang, D.D. Zhou, Technology advances and challenges in hermetic packaging for implantable medical devices, in: D. Zhou, E. Greenbaum (Eds.), Implantable Neural Prostheses 2, Springer, New York, New York, NY, 2010, pp. 27–61.
[31] E. Blasco-Tamarit, A. Igual-Muñoz, J.G. Antón, D.M. García-García, Galvanic corrosion of titanium coupled to welded titanium in LiBr solutions at different temperatures, Corros. Sci. 51 (2009) 1095–1102, http://dx.doi.org/10.1016/j.corsci.2009.02.023.
[32] K. Nakahara, M. Yamamoto, Y. Okayama, K. Yoshimura, K. Fukagata, N. Miki, A peristaltic micropump using traveling waves on a polymer membrane, J. Micromech. Microeng. 23 (2013) 85024, http://dx.doi.org/10.1088/0960-1317/23/8/085024.
[33] R. Rapp, Schomburg, W.K. Schomburg, J. Schulz, W. Stark, LIGA micropump for gases and liquids, Sens. Actuators A Phys. 40 (1994) 57–61, http://dx.doi.org/10.1016/0924-4247(94)85030-5.
[34] G. Liu, C. Shen, Z. Yang, X. Cai, H. Zhang, A disposable piezoelectric micropump with high performance for closed-loop insulin therapy system, Sens. Actuators A Phys. 163 (2010) 291–296, http://dx.doi.org/10.1016/j.sna.2010.06.030.
[35] T. Guo, T. Meng, W. Li, J. Qin, Z. Tong, Q. Zhang, X. Li, UV-driven microvalve based on a micro–nano TiO2/SiO2 composite surface for microscale flow control, Nanotechnology 25 (2014) 125301.
[36] M. Herz, M. Richter, M. Wackerle, Method for manufacturing a bending transducer, a micro pump and a micro valve, micro pump and micro valve, Google Patents, 2016.
[37] C. Veiga, J.P. Davim, A.J.R. Loureiro, Properties and applications of titanium alloys: a brief review, Rev. Adv. Mater. Sci. (2012) 133–148.
[38] C. Durasiewicz, A. Bußmann, S. Kibler, C. Wald, Experimental Characterisation and Simulation of Piezoelectric Titanium Micropumps and Titanium Microvalves, Fordatis - Research Data Repository of Fraunhofer-Gesellschaft, 2019, pp. 2019, http://dx.doi.org/10.24406/fordatis/74.
[39] C. Leyens, M. Peters, J. Kumpfert, Titanium and Titanium Alloys: Fundamentals and Applications, Wiley & Sons, 2003.
[40] Z. Chen, U. Gandhi, J. Lee, R. Wagoner, Variation and consistency of Young's modulus in steel, J. Mater. Process. Technol. 227 (2016) 227–243, http://dx.doi.org/10.1016/j.jmatprotec.2015.08.024, January 2016, 227.
[41] M. Herz, D. Horsch, G. Wachutka, T.C. Lueth, M. Richter, Design of ideal circular bending actuators for high performance micropumps, Sens. Actuators A Phys. 163 (2010) 231–239.
[42] E. Chappel, S. Mefti, G.-L. Lettieri, S. Proennecke, C. Conan, High Precision Innovative Micropump for Artificial Pancreas, in: Microfluidics, BioMEMS, and Medical Microsystems XII, SPIE, San Francisco, California, United States, 2014, pp. 89761C.
[43] S. Ogden, L. Klintberg, G. Thornell, K. Hjort, R. Bodén, Review on miniaturized paraffin phase change actuators, valves, and pumps, Microfluid Nanofluid 17 (2014) 53–71, http://dx.doi.org/10.1007/s10404-013-1289-3.
[44] P.-H. Cazorla, O. Fuchs, M. Cochet, S. Maubert, G. Le Rhun, Y. Fouillet, E. Defay, A low voltage silicon micro-pump based on piezoelectric thin films, Sens. Actuators A Phys. 250 (2016) 35–39, http://dx.doi.org/10.1016/j.sna.2016.09.012.
[45] A.F. Doll, M. Wischke, A. Geipel, F. Goldschmidtboeing, O. Ruthmann, U.T. Hopt, H.-J. Schrag, P. Woias, A novel artificial sphincter prosthesis driven by a four-membrane silicon micropump, Sens. Actuators A Phys. 139 (2007) 203–209, http://dx.doi.org/10.1016/j.sna.2007.03.025.
[46] R. Zengerle, J. Ulrich, S. Kluge, M. Richter, A. Richter, A bidirectional silicon micropump, Sens. Actuators A Phys. 50 (1995) 81–86, http://dx.doi.org/10.1016/0924-4247(96)80088-4.

Biographies

Agnes Bußmann, M. Sc. received her Master of Science in Mechanical Engineering from TU Munich in 2017. During her research stay in France she investigated failure mechanisms of vascular prosthesis. She currently works as a development engineer at the Fraunhofer Research Institution for Microsystems and Solid State Technologies EMFT and pursues her doctorate in cooperation with the Institute of Engineering in Life Sciences of the Karlsruhe Institute of Technology. Her research focusses on piezoelectric micro diaphragm pumps and their biomedical application.

Claudia Durasiewicz, M. Sc. graduated at the Technical University of Berlin with a Master degree in Engineering Science specializing in fluid mechanics. During her studies she worked in the field of medical device development, e.g. studies of flow phenomena in an innovative VAD system. As a visiting scholar at the University of Arizona she investigated plasma-actuation of the flow around an airfoil on a nanosecond scale. She joined the department for Micro Dosing Systems at the Fraunhofer EMFT in October 2017. In her doctorate work she focuses on microscale process technologies for micropump and microvalve development.

Dr.-Ing. Sebastian Kibler studied Electrical Engineering and Information Technologies at the TU Munich and received his diploma in 2008. He joined the Fraunhofer EMFT Team of Micro Dosing Systems in 2008 to work in the field of system development of micro dosing systems. Within his work on feedback-controlled micro dosing for nanoliter oil lubrication, he finished his doctoral degree at the Bundeswehr University Munich in 2017. As head of the Systems and Implants group he focuses on the management of system and component development of micro fluidic actuators and dosing units for implantable medical applications.

Christian Wald, Dipl.-Wirtsch.-Ing. studied Industrial Engineering at the Karlsruher Institute for Technology KIT and got his diploma in 2010. He joined the Fraunhofer EMFT Team of Micro Dosing Systems in 2011 and worked in the field of medical devices (negative pressure wound therapy, infusion) and industrial applications (water analysis, vaporizer, gas- and smoke detection and fuel cells). Focus of his work are the metal micropump development and business development. In 2015 he became Deputy Quality Manager of the Fraunhofer EMFT and in 2018 Deputy Department Manager of the Micro Dosing Systems team.

Piezoceramic Mounting Process and Adapted Pretension for Improved Microvalve Functionality and Reliability

C. Durasiewicz[1], S. Güntner[1], Dr. S. Kibler[1]

[1]Fraunhofer EMFT Research Institution for Microsystems and Solid State Technologies, Hansastrasse 27d, Munich, Germany, claudia.patricia.durasiewicz@emft.fraunhofer.de

originally published in: Proceedings of MikroSystemTechnik Kongress 2021, Stuttgart-Ludwigsburg, 08.-10. Nov. 2021, ISBN 978-3-8007-5656-8, VDE e.V. (Hrsg.)

Abstract

Active microvalves enable opening and closing of a microfluidic path at any desired time, therefore, piezoelectric actuation is very well suited to ensure fast response times, energy efficient operation, and high forces for valve closing. In order to develop piezoelectric microvalves exhibiting high fluidic performance as well as long-term reliability, it is important to understand the influences of its key design features on microvalve leakage rates and piezoceramic stability and to use the gained insight for device optimization. Following our recent studies on our novel piezoelectric titanium microvalves with integrated O-ring soft sealing, we present an elaborated piezoceramic mounting process with an adaptation of the electro-mechanical pretension for optimized microvalve leakage performance. We verify the adaptability of the presented process by fabrication and comparative tests of three groups of microvalves with a variation of valve seat height and sealing material. Our optimized titanium microvalves show both material and sealing performance stability in a $1 \cdot 10^6$ actuation cycles fatigue test.

1 Introduction

Small, reliable, and energy efficient microvalves are an essential basis of flow path control in highly integrated microsystems [1–3]. Especially medical applications like lab-on-chip and implantable or wearable medical devices necessitate active flow path control with demanding device requirements. Not only small leakage rates in closed state are extremely important, but also, long-term reliability of the microvalve is indispensable. Our novel normally open (NO) titanium microvalve [4] is based on piezoelectric actuation

and comprises an O-ring soft sealing serving as a valve seat, ensuring low leakage rates in closed state. However, the soft sealing component also adds to the complexity of the device: Our first manufactured NO valves [4] showed a non-uniform preforming of their piezoceramic in topology measurements (Figure 1). During NO valve operation, material failure of the piezoceramics occurred. Insufficiently low manufacturing precision of the O-rings was identified as root cause of these failures.

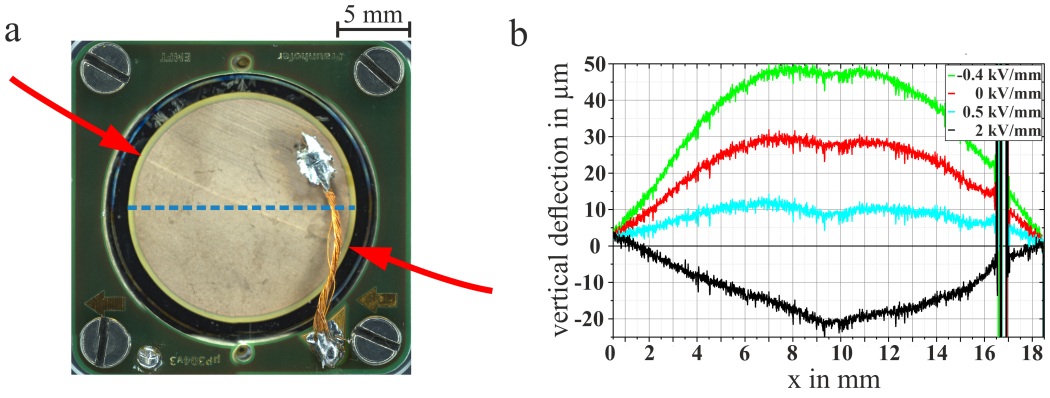

Figure 1: **a** Light microscope photograph of a microvalve from our previous studies[4]. Red arrows indicate the fracture across the piezoceramic due to excessive bending over the O-ring soft sealing. The blue dashed line indicates the measurement line for topology measurement. **b** Topology measurement across the piezoceramic with different voltages applied.

Therefore, we adapt our piezoceramic mounting procedure to ensure both high sealing performance and material stability of the NO microvalve. We present the transfer of an elaborated piezoceramic mounting process of our known stainless steel micropumps [5] to our piezoelectric titanium microvalves. We adapt the electro-mechanical pretension technique [6] to optimize closed state performance and assess material stability of the piezoelectric actuator in extensive fatigue testing.

2 Materials and Methods

The microvalve consists of a rigid titanium body with two fluid ports and a sealing notch, an O-ring soft sealing, and a titanium actuator foil joined to the body by laser welding (Figure 2). A 200 μm thick PZT piezoelectric disc actuator is glued on the titanium foil with a DC voltage and a compression force applied during glue curing, in order to achieve a defined pretension of the actuator diaphragm [6].

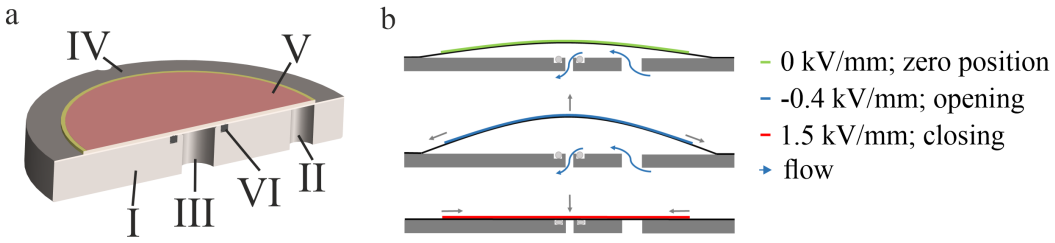

Figure 2: **a** Model of the normally open piezoelectric microvalve with an outer diameter of 20 mm and 2.6 mm height. It comprises of a rigid titanium body (I) with an inlet (II) and outlet (III) as well as an O-ring (VI) in a micromachined notch. The actuator diaphragm consists of a welded on titanium foil (IV) of 100 μm thickness and a glued on 200 μm thick PZT (V). **b** Working principle of the NO microvalve. In non-actuated state, fluid flows through the NO valve when a pressure gradient is present. Using the inverse piezoelectric effect, the valve's actuator diaphragm is actuated to either open further or to achieve tight closing of the valve.

In non-actuated state, the normally open (NO) microvalve allows fluid flow. Using the inverse piezoelectric effect, the valve opens further when a negative electric field is applied. Under a positive electric field, tight closing of the microvalve is achieved when the actuator diaphragm sits on the valve seat. The inserted O-ring protrudes over its notch, creating an elevated valve seat. The actuator diaphragm's zero position relative to the valve seat defines its open and closed state fluidic performance and is mainly controlled by the pretension voltage V_p applied during glue curing.

Profilometric characterization of the O-rings reveals that their measured chord size of $(495 \pm 33)\,\mu$m varies strongly around their nominal value of 500 μm. Large chord sizes lead to high valve seats, which therefore cause excessive bending of the piezoceramic during valve operation, if the actuator's zero position is not adjusted accordingly. In order to prevent piezoceramic material failure caused by the protruding O-ring, we introduce two countermeasures.

Firstly, we reduce the compression forces on the piezoceramics from 50 N to $\leq$ 5 N per microvalve. Secondly, we implement valve seat height measurements of each NO valve (Figure 3), which enable individual pretension voltage V_p adaption for optimized actuator diaphragm zero position. We introduce an empirical adaption factor of $c = 1.6\,\mathrm{V}/\mu\mathrm{m}$, which we use to calculate the pretension voltage V_p as a function of measured valve seat height h_{vs} : $V_p = c \cdot h_{vs}$.

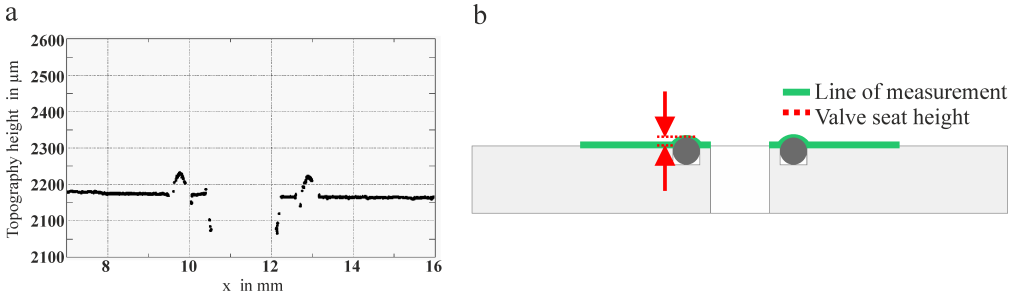

Figure 3: **a** White light profilometry data of valve seat height prior to welding. **b** Demonstration of line of measurement to determine valve seat height.

In order to verify the adaptability of the proposed manufacturing procedure, we assemble three groups of microvalve samples with a variation of valve seat height and sealing material: Similar to the previously built microvalves, the first group comprises a FKM O-ring with 500 μm nominal chord size. The second group is built with an EPDM O-ring of 600 μm nominal chord size, leading to higher valve seat height h_{vs}. A third group of microvalves without O-rings is assembled without electro-mechanical pretension of their bending actuator, as the valve seat height is zero.

The fabrication and test of the three microvalve variations allow for comparison of leakage rate performances as well as their sample-to-sample variation after assembly. Also, we evaluate material and sealing performance stability by subjecting the adapted microvalves to a $1 \cdot 10^6$ actuation cycles fatigue test.

For initial assessment of microvalve operation, field-dependent actuator stroke is determined using a white light profilometer (Fries Research and Technology) with a sensor range of 3 mm and maximal resolution of 30 nm. We evaluate the total actuator stroke of the microvalve under quasi-static voltage actuation from $-0.4\,\mathrm{kV/mm}$ to $2.0\,\mathrm{kV/mm}$ using a voltage amplifier (SVR1000-3, piezosystem jena GmbH).

Pressure-dependent fluidic performance in a pressure range up to 20 kPa is measured with distilled water at room temperature and using a pressure controller (Mensor CPC3000: range -50 kPa to 200 kPa, accuracy: ± 50 kPa). We conduct microvalve leakage rate measurements in closed state as well as open state flow rate measurements with Coriolis flow sensors (Bronkhorst mini Cori-Flow ML120V00: range $0.8\,\mu\mathrm{L/min}$ to $500\,\mu\mathrm{L/min}$, accuracy: $\pm 0.2\,\%$ and Bronkhorst mini Cori-Flow M14: range $0.5\,\mathrm{mL/min}$ to $167\,\mathrm{mL/min}$, accuracy: $\pm 0.2\,\%$, respectively). We operate the microvalves at sinusoidal actuation at 100 Hz between $-0.4\,\mathrm{kV/mm}$ to $2.0\,\mathrm{kV/mm}$ for extensive fatigue testing for a total of $1 \cdot 10^6$ actuation cycles with a 33500B Trueform Series waveform generator (Keysight).

3 Results and Discussion

An overall amount of 52 microvalve samples was characterized for actuator stroke and water leakage performance as an initial test after assembly (see Table 1).
The total actuator stroke of the 500 μm FKM microvalves is significantly higher compared to the other two types. A lower total actuator stroke found in NO microvalves without soft sealing component can be explained by the omitted electro-mechanical pretension of the bending actuator, leading to a low initial position of the actuator diaphragm. The difference between 500 μm FKM and 600 μm EPDM microvalves due to the pretension is unlikely, as both groups were assembled with valve seat height dependent pretension. As the O-rings of these two types are made out of different rubber materials, the difference in total actuator stroke can be caused by changed elasticity of the O-rings. Dedicated studies of the hyperelastic soft sealing components alone are needed to further investigate this observation.

Table 1: Overview of NO valve samples investigated in this study. Three NO valve groups with different valve seats were characterized regarding valve seat height, actuator stroke, and fluidic performance.

	500 μm **FKM**	600 μm **EPDM**	**Without soft sealing**
Sample size n	27	11	14
Valve seat height in μm	33.2 ± 16.1	107 ± 59	0
Actuator stroke in μm	59.1 ± 7.3	52.9 ± 6.5	50.7 ± 3.4
Max. water open flow at 20 kPa	11.7 ± 5.7	13.2 ± 5.6	5.2 ± 1.4
Water leakage at 20 kPa, 2 $^{kV}/_{mm}$, in $^{\mu L}/_{min}$	14.9 ± 13.7	7.5 ± 1.4	13.7 ± 17.2
Normalized water leakage at 20 kPa, 2 $^{kV}/_{mm}$, after fatigue testing	0.9 ± 0.3	1.1 ± 0.2	1.0 ± 0.9

Fluidic characterization of the NO valves includes both open and closed state water flow performance. In open state, the flow rate is well over 10 $^{mL}/_{min}$ for the 500 μm FKM and 600 μm EPDM microvalves, whereas for microvalves without soft sealing, the flow rate is only (5.2 ± 1.4) $^{mL}/_{min}$. This difference can also be explained by the omission of electro-mechanical pretension of the bending actuator for NO microvalves without

soft sealing, as the narrow fluid path through the valve chamber of the samples without pretension exhibits a high fluidic resistance.

Water leakage rates at an inlet pressure of 20 kPa and a constant electric field of 2.0 $^{\mathrm{kV}}/_{\mathrm{mm}}$ of all three NO microvalve types measured after assembly are shown in Figure 4. The titanium microvalves exhibit an overall average of $(13 \pm 13.4)\,{}^{\mu\mathrm{L}}/_{\mathrm{min}}$ water leakage rate. Comparatively low standard deviation of the measured leakage rates of 600 μm EPDM microvalves indicates that sample-to-sample variation is lowered compared to the other sealing types. Changed hyperelastic characteristics could cause such difference in leakage rates, as a higher deformation of the O-ring under the same piezoactuator force would lead to smaller leakage paths. The narrow distribution of leakage rates observed in NO valves without soft sealing reveals that the high standard deviation is caused by extreme outliers. This observation also indicates that the metal-on-metal contact interface between actuator foil and valve seat creates a large enough flow resistance to enable tight valve closing.

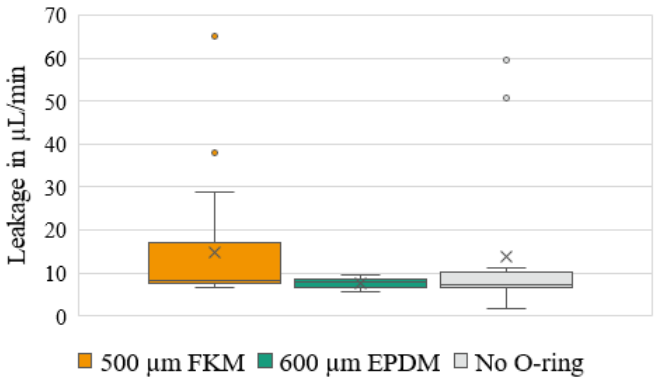

Figure 4: Boxplots of NO valve initial measurement of water leakage rates at 20 kPa inlet pressure and a constant electric field of 2 $^{\mathrm{kV}}/_{\mathrm{mm}}$.

We subjected $n = 5$ samples of each group to a $1 \cdot 10^6$ actuation cycles fatigue test, where piezoceramic material failure was not observed. Subsequent water leakage characterization was performed and normalized with the respective leakage rate measurement of each individual sample prior to fatigue testing to evaluate possible change in performance. Normalized leakage rates of the three tested groups are depicted in Figure 5.

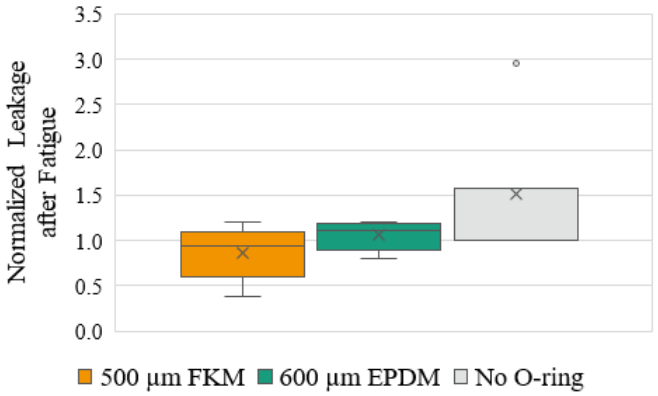

Figure 5: Boxplots of normalized water leakage after $1 \cdot 10^6$ actuation cycles fatigue test. NO valve water leakage is measured after fatigue test and normalized with initial measurement to show stability of fluidic performance over device lifetime. $n = 5$ for each group.

Good stability of closed state flow performance was found in all three tested groups. While leakage rates even decreased in 500 μm FKM microvalves (0.9 ± 0.3), they increased only slightly for 600 μm EPDM microvalves (1.1 ± 0.2). Due to outliers, a high standard deviation of 0.9 was found for microvalves without soft sealing, with a median of 1.0 normalized leakage rate. The observations indicate an overall good stability of both material and leakage characteristics, which are basis for reliable high performance microfluidic devices.

4 Conclusion

This comparative study of NO microvalves with different valve seat heights and materials aimed to evaluate the adaptability of our proposed piezoceramic mounting procedure and its impact on microvalve reliability.

We manufactured titanium based microvalves with different rubber O-rings or without soft sealing component and mounted the piezoceramic actuators with a specific voltage applied during glue curing depending on valve seat height, therefore accounting for different elevations of the protruding O-ring by specific electro-mechanical pretension of the piezoelectric bending actuator.

In initial measurements, low microvalve leakage rates in closed state was observed in all three groups. Differences in microvalve characteristics can be explained by possible change in hyperelastic behaviour of the used rubber O-rings, yet overall improvement of

leakage rates and sample-to-sample variation compared to previously studied microvalves proves adaptability of the implemented procedure.
A sample size of $n = 5$ microvalves of each group was subjected to a $1 \cdot 10^6$ actuation cycles fatigue test in order to investigate microvalve stability. We observed no piezoactuator failure in form of piezoceramic cracks or deformation. Subsequent leakage testing revealed high stability of the leakage performance independent of valve seat type. The stability observed in the extensive fatigue testing here lays the basis for further development of reliable microvalves.
Future studies will include characterization of hyperelastic soft sealing components as well as fatigue tests with larger sample sizes to further investigate influences leading to the differences found within the three groups of microvalves studied here. Additionally, future research will be conducted to improve open flow characteristics of NO valves without soft sealing components.

5 References

[1] J.-Y. Qian, C.-W. Hou, X.-J. Li, and Z.-J. Jin, "Actuation mechanism of microvalves: A review," *Micromachines*, vol. 11, no. 2, p. 172, 2020.

[2] M. Moreno, C. Aracil, and J. M. Quero, "High-integrated microvalve for lab-on-chip biomedical applications," in *2008 IEEE Biomedical Circuits and Systems Conference*, pp. 313–316, IEEE.

[3] K. W. Oh and C. H. Ahn, "A review of microvalves," *Journal of Micromechanics and Microengineering*, vol. 16, no. 5, pp. R13–R39, 2006.

[4] A. B. Bußmann, C. P. Durasiewicz, S. H. A. Kibler, and C. K. Wald, "Piezoelectric titanium based microfluidic pump and valves for implantable medical applications," *Sensors and Actuators A: Physical*, p. 112649, 2021.

[5] C. Wald, M. Richter, M. Holzer, and M. Weigl, "Concept of a novel stainless-steel micro pump for applications in medicine and biotechnology," *Mikrosystemtechnik Kongress 2013*, 2013.

[6] M. Herz, M. Richter, and M. Wackerle, "Method for manufacturing a bending transducer, a micro pump and a micro valve, micro pump and micro valve," U.S. Patent 9410641B2, 2016.

”Safety Valve”: A Metal-Based, Self-Securing Switchable Microvalve for Medical Applications

C. Durasiewicz[1], W. Hölzl[2] and G. Schrag[2]

[1]Fraunhofer EMFT Research Institution for Microsystems and Solid State Technologies, Hansastrasse 27d, Munich, Germany, claudia.patricia.durasiewicz@emft.fraunhofer.de

[2]Chair for Physics of Electrotechnology, Technical University of Munich, 80333 Munich, Germany

originally published in: Proceedings of MikroSystemTechnik Kongress 2021, Stuttgart-Ludwigsburg, 08.-10. Nov. 2021, ISBN 978-3-8007-5656-8, VDE e.V. (Hrsg.)

Abstract

Drug dosing systems require fail-safety in order to prevent patients' harm. We present a passive microvalve without external control or energy consumption designed to regulate the flow path of a microfluidic drug dosing system. The metal-based self-securing switchable microvalve for medical applications is experimentally characterized for water flow rates and fluidic resistance. Additionally, we characterize a microfluidic delivery system comprising a piezoelectric micropump in combination with the microvalve for delivered water flow rate and find a maximum of $(13.8 \pm 0.7)\,{}^{\mathrm{mL}}/_{\mathrm{min}}$, as well as fail-safe state leakage rates with an average of $(31.8 \pm 5)\,{}^{\mu\mathrm{L}}/_{\mathrm{min}}$. Among the manufactured and tested microvalves, several valves exhibit pressure-induced flow obstruction. Dedicated FEM simulations of the flow inside the microvalve show flow field-induced phenomena as reasons for this malfunctioning, which lays the basis for a deeper understanding of the functionality of the component.

1 Introduction

With increasing research towards wearable drug delivery systems incorporating drug reservoirs, micropumps, and microneedles [1, 2], the need for microfluidic safety components like self-securing microvalves [3] arises in order to prevent uncontrolled drug release. Fluidic systems with squeezable reservoirs bear the risk of uncontrolled fluid flow, e.g. in case of applied overpressure. Micropumps for drug delivery comprising pre-tensed flap valves or flexible diaphragm valves have been reported to successfully prevent free-flow up to 15 kPa [4] or 75 kPa [5], respectively, but these valves are not able to impede uncontrolled

drug transfer at pressures exceeding the valves' threshold pressure. We present a passive metal-based microvalve serving as a safety measure for microfluidic drug delivery systems without pressure limitation of free-flow prevention (see Figure 1).

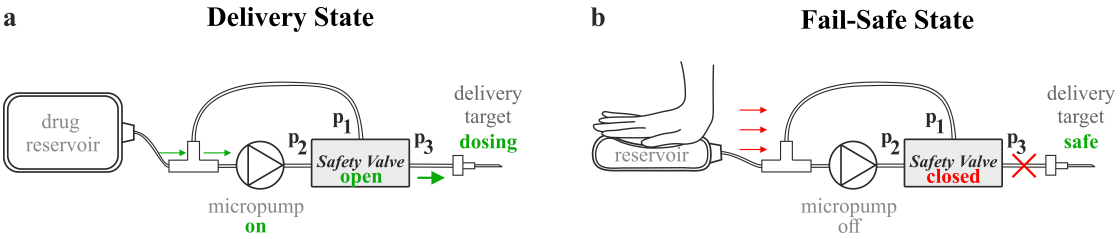

Figure 1: Schematics of a drug delivery system incorporating a drug reservoir, a micropump, a self-securing switchable microvalve ("safety valve"), and a microneedle. **a** Delivery state: the micropump generates a sufficiently large pressure $p_2 > p_1 + p_{spring}$ opening the microvalve to establish drug dosing from the reservoir into the delivery target. **b** In case of excessive external pressure applied to the reservoir during off-state of the pump, the fail-safe state of the microvalve restricts fluid flow due to $p_1 + p_{spring} > p_2$, preventing uncontrolled drug release.

2 Materials and Methods

The metal-based self-securing microvalve is designed to provide flow logic without external control or energy consumption due to its specific three fluid port design: Switching of the valve between fail-safe and delivery state is facilitated by the pressures present at the control port p_1 and the inlet port p_2 (see Figure 2). Uncontrolled drug release from the outlet port p_3 is prevented if $p_1 + p_{spring} > p_2$. We manufacture microvalves consisting of a rigid steel body with two fluid ports and a sealing notch, a FKM O-ring soft sealing, and a steel diaphragm foil joined to the body by laser welding (Figure 2b and c). The O-ring protrudes over its notch, creating an elevated valve seat. This leads to an initial deflection of the steel diaphragm, resulting in a specific spring load. Hence, fluid can flow through the valve once the pressure p_2 exceeds the pressure applied to the top of the diaphragm by a certain threshold $p_1 + p_{spring}$ with a design value of $p_{spring} = 15\,\mathrm{kPa}$.

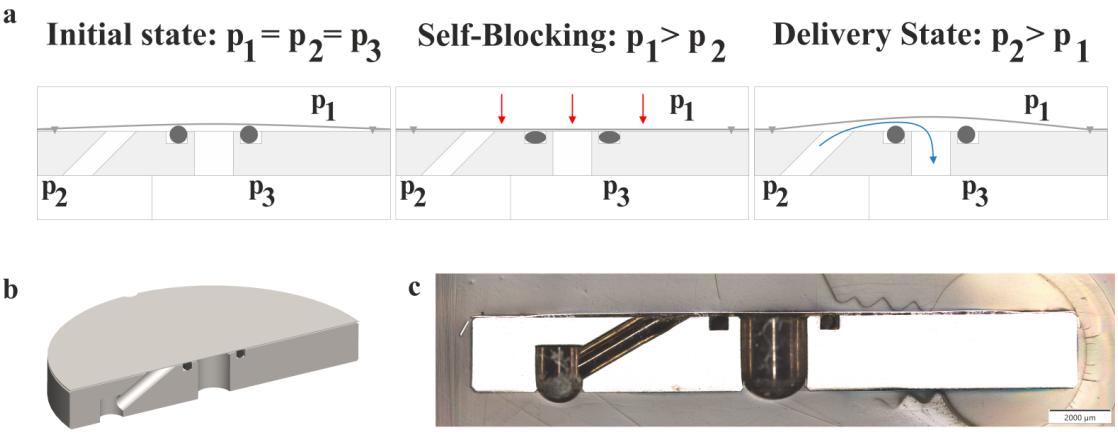

Figure 2: **a** Self-securing switchable microvalve states dependent on the relative pressures applied. The pre-tensed steel diaphragm exerts a spring force towards the soft sealing represented by the additional equivalent pressure p_{spring} acting on the steel diaphragm. **b** Model of the microvalve with an outer diameter of ∅20 mm and a height of 2.55 mm. **c** Cross-section of a stainless steel microvalve with an inserted O-ring sealing. The valve chamber is covered by a 50 μm thin welded on steel diaphragm.

Fluidic experiments are conducted at room temperature with distilled water, the flow rate are determined by Coriolis flow sensor (Bronkhorst MINI CORI-FLOW M14: range 0.5 $^{\mathrm{mL}}/_{\mathrm{min}}$ to 167 $^{\mathrm{mL}}/_{\mathrm{min}}$, accuracy: ±0.2 %). We characterize the pressure-dependent flow rate through the microvalves in a pressure range up to 60 kPa, controlled by a pressure controller (Mensor CPC3000: range −50 kPa to 200 kPa, accuracy: ±50 kPa). Additionally, we characterize the pressure drop over five malfunctioning microvalves. To this end, a differential pressure sensor (Bronkhorst EL-PRESS P-506C: range 0.0 kPa to 400 kPa, accuracy: ±2 kPa) is placed into the flow path in parallel to the microvalve.
In addition to the characterization of the microvalve component we combine our piezoelectric stainless steel micropump [6, 7] with the microvalve to create a microfluidic delivery system. We test the delivery system in delivery state as well as fail-safe state to find achievable water flow rates as well as leakage rates, respectively. Piezoelectric actuation of the micropump is facilitated with a sinusoidal voltage signal generated by a Keysight Trueform Series 33500B waveform generator and amplified to −80 V to 300 V using a piezo amplifier (SVR500-3, piezosystem jena GmbH).
In order to assess the reason for the performance loss of the malfunctioning microvalves, we carry out FEM simulations using the software package COMSOL Multiphysics, which are addressed in detail in Section 3.2.

3 Results and Discussion

In this section, the experimental data of the self-securing switchable microvalves as a single device as well as in combination with a piezoelectric micropump as part of a microfluidic delivery system is presented and FEM simulations are evaluated in order to assess the flow-induced effects leading to the malfunctioning of several microvalves.

3.1 Experimental Characterization

We determine the microvalve's pressure-dependent passive flow rate to evaluate its flow resistance as well as the pressure p_{spring}. In order to switch the microvalve to its delivery state, an underpressure of $p_1 = -15\,\mathrm{kPa}$ is applied, and a water flow is forced through the valve increasing the pressure p_2. By design, the microvalve is in delivery state for applied underpressure p_1. However, the results in Figure 3 show, that the water flow is still restricted for $p_2 \leq 5\,\mathrm{kPa}$. From this, it can be deduced that the spring load created by the initial deflection is equivalent to a pressure of $p_{spring} = 20\,\mathrm{kPa}$. The standard deviation of seven tested samples indicates large manufacturing tolerances.

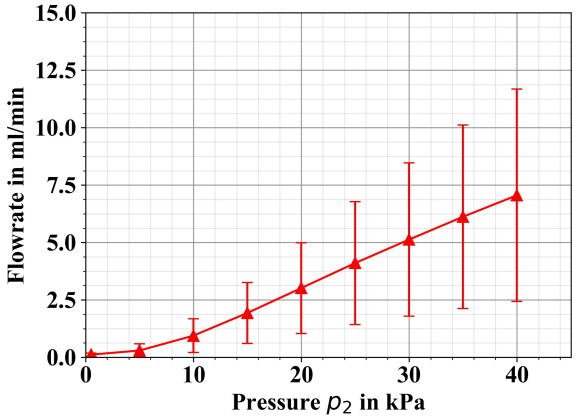

Figure 3: Flow rate in delivery state: an underpressure of $p_1 = -15\,\mathrm{kPa}$ is applied and the flow rate of seven microvalves is determined depending on the inlet pressure p_2.

Another group of $n = 5$ microvalves exhibits a restriction of water flow. For further investigation of this malfunctioning, the pressure p_2 at the microvalve inlet is increased up to 60 kPa while p_1 remains at atmospheric pressure, and the pressure drop $\Delta p = p_3 - p_2$ is measured (see Figure 4). The tested five microvalve samples show an increase in

pressure loss while p_2 increases, which implies that a fluidically induced effect causes partial blocking of the fluidic path compared to its nominal flow for the respective applied pressure. This effect is studied further by FEM simulation.

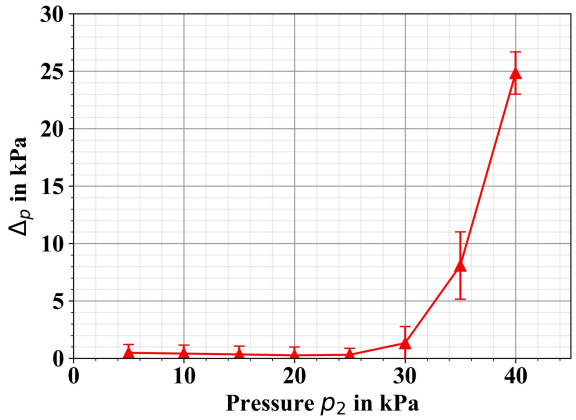

Figure 4: Pressure loss measured for $n = 5$ microvalves when the pressure p_2 is increased; the control pressure p_1 remained at atmospheric pressure: we observed a distinct loss in pressure, indicating a partial blocking of the valve.

The microfluidic delivery system is further tested to evaluate the fail-safe state leakage through the delivery system in case of excessive external pressure. To this end, the water pressure p_{inlet} at the pump inlet is increased up to 60 kPa and it is observed that the leakage rates stay on a low value of $(31.8 \pm 5)\,\mu\mathrm{L}/\mathrm{min}$ (see Figure 5).

The flow delivery by the whole system is characterized by combining the microvalves with the piezoelectrically actuated steel micropump and determining the frequency-dependent flow rate as well as the maximal flow rate of the micropump. The measured characteristic of seven different samples shows a typical linear frequency dependence of the flow rate for $f \leq 50\,\mathrm{Hz}$ (see Figure 6).

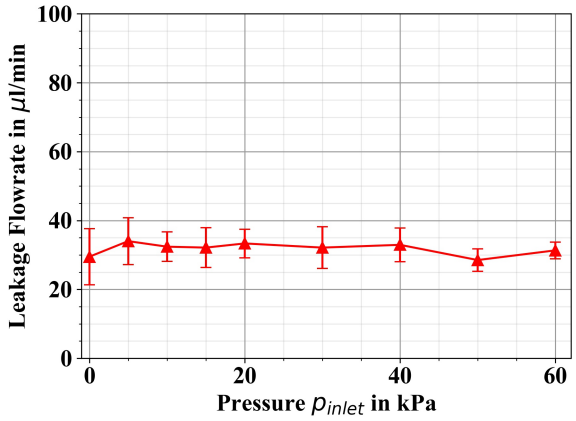

Figure 5: Fail-safe state leakage flow rate of a delivery system comprising a micropump and a self-securing switchable microvalve. Leakage rates of the delivery system tested with $n = 7$ different microvalves remain stable at a low value of $(31.8 \pm 5)\,{}^{\mu\mathrm{L}}/_{\mathrm{min}}$.

Due to inertial effects of the valves and the fluidic periphery, further increase of fluid flow is diminished, and the dependency at higher frequencies becomes non-linear. However, the linear regime for frequencies up to 50 Hz allows for a large enough variability in dosed flow rates and the maximal achievable average flow rate of $(13.8 \pm 0.7)\,{}^{\mathrm{mL}}/_{\mathrm{min}}$ shows that the microvalve does not impede the performance of the micropump with a view to the delivered flow.

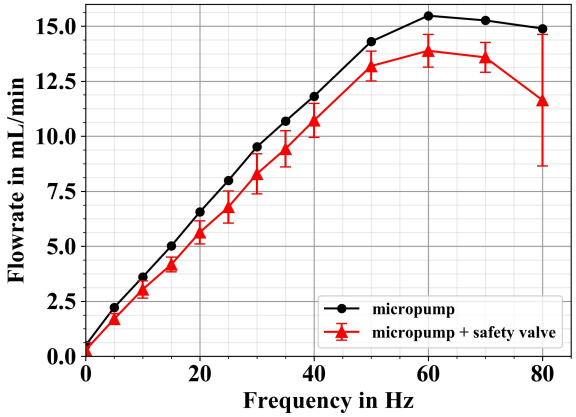

Figure 6: Frequency-dependent flow rate of the micropump and the whole system (micropump and valve) in delivery state averaged over seven different valves combined with the micropump, respectively. The flow increases linearly for $f \leq 50$ Hz reaching a maximum flow rate of $(13.8 \pm 0.7)\,{}^{\mathrm{mL}}/_{\mathrm{min}}$.

3.2 FEM Simulation

The numerical analysis requires solving a fully coupled fluid-structure-interaction problem with mechanical contact. Figure 7 shows a radial cross section of the initial deflection of the O-ring within the notch when the diaphragm is at rest. The black circle represents the undeformed ring, the grey areas on the left and the bottom represent the notch, and the grey area at the top is the diaphragm. The initial deflection of the O-ring creates a tensile stress inside the ring, pressing it against the inner wall of the notch. In vertical direction, the diaphragm pushes the ring into the notch. This seals the valve tightly. However, the O-ring becomes vertically unconstrained when the diaphragm moves upwards and loses contact. The O-ring, made of Viton, is modelled as a 2-parameter Mooney-Rivlin material, with parameters taken from Makino et al.[8]. The valve body is treated as a rigid body and the diaphragm as a linear elastic mechanical structure.
The white area around the ring in Figure 7 represents the fluidic domain. However, when the O-ring either establishes or loses contact with the structure or the diaphragm, the topology of the fluid domain changes. This is problematic for the method of finite elements. To remedy this, we added a small clearance around the ring. This will lead to a significant amount of leakage and, thus, overestimate the flow rate, but we deemed this error acceptable for the investigation of the experimentally observed and unexpected pressure drop in open state.

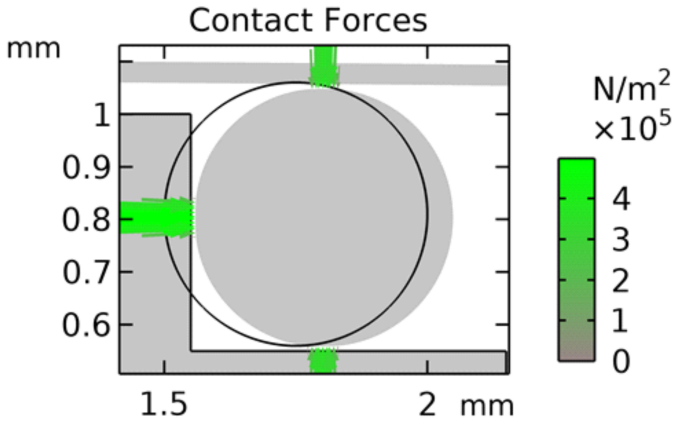

Figure 7: Radially deformed O-ring. The black circle depicts the undeformed ring. The contact area is highlighted green. Note the small clearance between the ring and the surrounding structure.

For the fluidic simulation, we exploited the mirror symmetry of the valve, neglected its

bottom half, and modelled the inflow as a fully developed flow at the skewed inlet. We solved for the stationary solution of a laminar flow of water at room temperature. Figure 8 shows the streamlines of the velocity field at an input pressure of 40 kPa. Figure 9 shows a detailed view of the regions around the O-ring.

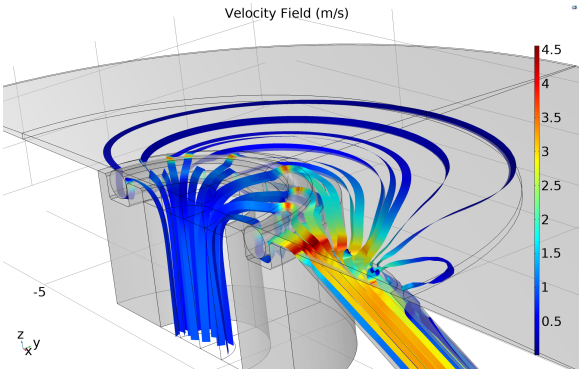

Figure 8: Streamlines of the velocity field at 40 kPa input pressure.

The simulations reveal that the ring is lifted from its default position by about 80 μm and obstructs the fluid flow between itself and the diaphragm. This lift is nearly uniform for the entire ring, with a little higher deflection near the inlet, c.f. Figure 9 (right).

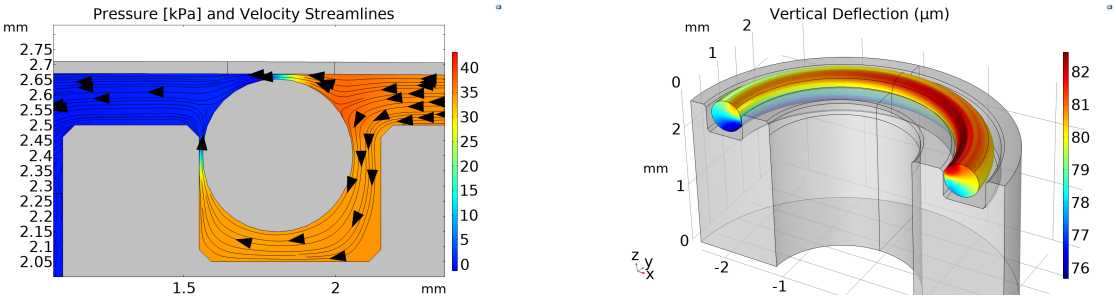

Figure 9: The lifted ring obstructs the fluid flow and creates a large pressure drop (left). The right shows the vertical deflection from the initial position at 40 kPa.

The load consists mostly of the static pressure within the fluid. The entire pressure drops across the small clearance between the ring and the valve diaphragm.
The simulation results explain the pressure drop very well. The effect of the O-ring leaving its default position could be observed for a wide range of input pressures. We conclude that a possible counter-measure of this malfunction is to use an O-ring which is larger than the notch, so it contacts the outer notch wall rather than the inner one.

In this case the fluid flow will push the ring down into the notch. However, this will require further research regarding the influences of the O-ring thickness on the leakage rate.

4 Conclusion

We presented a self-securing, switchable, passive microvalve without pressure limitation of its free-flow prevention mechanism as a potential safety component for drug delivery systems. In combination with a piezoelectric micropump, the microvalve exhibits good flow restriction in case of excessive external pressure, and allows for high flow rates as the micropump actively delivers fluid through the valve. FEM studies reveal that fluid structure interactions with the integrated soft sealing component occur in several tested microvalves, leading to device malfunctioning. This identifies the Viton O-ring lifted by flow-induced forces as the critical component. Future designs of self-securing microvalves with parylene coatings on the diaphragm or microvalves without soft sealing components will be studied in order to avoid these effects.

5 Acknowledgement

This work was partly funded by the Bavarian Ministry of Economic Affairs, Regional Development and Energy within the project "Sichere intelligente Systeme" (safe intelligent systems) as well as the Federal Ministry of Education and Research under project reference numbers 16FMD01K, 16FMD02, and 16FMD03.

6 References

[1] M. Amjadi, S. Sheykhansari, B. J. Nelson, and M. Sitti, “Recent advances in wearable transdermal delivery systems,” *Advanced Materials*, vol. 30, no. 7, p. 1704530, 2018.

[2] C. L. Stevenson, J. T. Santini, and R. Langer, “Reservoir-based drug delivery systems utilizing microtechnology,” *Advanced drug delivery reviews*, vol. 64, no. 14, pp. 1590–1602, 2012.

[3] M. Richter and J. Kruckow, “Pump arrangement comprising a safety valve,” U.S. Patent 20100290935A1, 2010.

[4] D. Maillefer, S. Gamper, B. Frehner, P. Balmer, H. van Lintel, and P. Renaud, “A high-performance silicon micropump for disposable drug delivery systems,” *Technical*

Digest. MEMS 2001. 14th IEEE International Conference on Micro Electro Mechanical Systems (Cat. No. 01CH37090), pp. 413–417, 2001.

[5] P. Pankhurst and Z. M. Abdollahi, "Evaluation of a novel portable micro-pump and infusion system for drug delivery," *IEEE Engineering in Medicine and Biology Society. Annual Conference*, vol. 2016, pp. 465–468, 2016.

[6] C. Wald, M. Richter, M. Holzer, and M. Weigl, "Concept of a novel stainless-steel micro pump for applications in medicine and biotechnology," *Mikrosystemtechnik Kongress 2013*, 2013.

[7] A. B. Bußmann, C. P. Durasiewicz, S. H. A. Kibler, and C. K. Wald, "Piezoelectric titanium based microfluidic pump and valves for implantable medical applications," *Sensors and Actuators A: Physical*, p. 112649, 2021.

[8] A. Makino, W. R. Hamburgen, and J. S. Fitch, "Fluoroelastomer pressure pad design for microelectronic applications," *CiteseerX*, 1993.

applied sciences

MDPI

Article

Piezoelectric Normally Open Microvalve with Multiple Valve Seat Trenches for Medical Applications

Claudia Patricia Durasiewicz [1,2,*], Sophia Thekla Güntner [1], Philipp Klaus Maier [1], Wolfgang Hölzl [2] and Gabriele Schrag [2]

[1] Fraunhofer EMFT Research Institution for Microsystems and Solid State Technologies, 80686 Munich, Germany; sophia.guentner@st.oth-regensburg.de (S.T.G.); philippm1997@gmx.de (P.K.M.)
[2] Chair of Physics of Electrotechnology, Technical University of Munich, 80333 Munich, Germany; wolfgang.hoelzl@tum.de (W.H.); schrag@tum.de (G.S.)
* Correspondence: claudia.patricia.durasiewicz@emft.fraunhofer.de; Tel.: +49-89-54759-497

Abstract: Microfluidic systems for medical applications necessitate reliable, wide flow range, and low leakage microvalves for flow path control. High design complexity of microvalves increases the risk of possible malfunction. We present a normally open microvalve based on energy-efficient piezoelectric actuation for high closing forces and micromachined valve seat trenches for reliable valve operation. A comprehensive investigation of influencing parameters is performed by extensive fluidic 3D finite element simulation, derivation of an analytical closed state leakage rate model, as well as fabrication and test of the microvalve. Additional valve seat coating and a high force actuator are introduced for further leakage reduction. The microvalve has a wide-open flow range as well as good sealing abilities in closed state. Extensive fatigue tests of 1×10^6 actuation cycles show that additional coating of the valve seat or increased actuator strength promote sealing performance stability. Analytical calculations of leakage are suitable to estimate experimentally obtained leakage rates and, along with computational fluidic dynamic (CFD) simulations, enable future microvalve design optimization. In conclusion, we demonstrate that the presented normally open microvalve is suitable for the design of safe and reliable microfluidic devices for medical applications.

Keywords: microvalve; piezoelectric; microfluidics; modeling; FEA; CFD; fatigue

Citation: Durasiewicz, C.P.; Güntner, S.T.; Maier, P.K.; Hölzl, W.; Schrag, G. Piezoelectric Normally Open Microvalve with Multiple Valve Seat Trenches for Medical Applications. *Appl. Sci.* **2021**, *11*, 9252. https://doi.org/10.3390/app11199252

Academic Editor: Eric Chappel

Received: 6 August 2021
Accepted: 30 September 2021
Published: 5 October 2021

1. Introduction

Microfluidic systems for lab-on-chip applications, implantable or wearable medical devices often necessitate active flow path control that is achieved by using microvalves [1,2]. While passive microvalves show diode-like fluid path opening at forward pressure and closing at backwards pressure [3] or serve as constant flow regulators [4], active microvalves based on piezoelectric [5,6], shape memory alloy [7,8], phase change [9,10], or other actuation mechanisms [3] allow for opening and closing of fluid paths in an arbitrary, hence flexible and dedicated manner. External control of active microvalves enables functionalities like controlled dosing of drugs [11,12], mixture of reagents [10,13], confinement of a high pressure fluid to other volumes [14,15], as well as handling of small fluid volumes in medical devices and implants [16–20]. Such active flow path control can be achieved by piezoelectrically actuated microvalves, which are either of normally open (NO) or normally closed type, defined by their function in a non-actuated state [3], and typically consist of a piezoactuator, a valve diaphragm, and a valve seat [2]. Key figures of a high-performance microvalve are low leakage in closed state, a high flow rate in an open state, low power consumption, high particle contamination tolerance, and high stability of performance over lifetime. Additionally, medical applications like wearable drug dosing devices or implants require hermetic sealing of the device, low risk of component failure, as well as biocompatibility of all wetted surfaces [21].

Most recently, we reported on the development of an NO microvalve for microfluidic implants [14], showing low leakage rates ((10.9 ± 28.1) µL/min) as well as high flow rates in open state ((27.5 ± 5.3) mL/min) at a water pressure of 20 kPa. Insufficiently low manufacturing precision of the integrated O-ring sealing led to large sample-to-sample variations and induced various failure mechanisms of the microfluidic device. Constant closing due to flow-induced lift of the O-ring resulted in obstruction of the flow path and, hence, in partial or full blockage of the valve.

In this work, we suggest and investigate different alternative sealing concepts in order to overcome such problems. To this end, we design a novel, metal-based microvalve for liquid applications using biocompatible materials to meet requirements for medical applications. We omit movable sealing components, therefore reducing the risk of device failure, and investigate features like sophisticated geometric design, coating of the valve seat, or a high force actuator to further reduce leakage rates. A comprehensive analysis of parameters governing the performance provides insight into the microvalve's characteristics and allows for optimization and future design adaptation.

2. Materials and Methods

In order to investigate and optimize the presented piezoelectric NO valve concept, we manufacture various variants and evaluate them with a view to the resulting leakage rate, the open flow rate, and their performance stability. The fabrication process, the design variants as well as the methods to theoretically and experimentally evaluate their performance are described in this section.

2.1. Microvalve Design, Operation, and Fabrication

The design of the active diaphragm microvalve is depicted in Figure 1. It consists of a metal valve body (I) with an inlet (II) and an outlet (III), as well as a structured valve seat (IV). A metal diaphragm (V) is spanned over the valve seat with a piezoelectric ceramic layer (VI) bonded on top to create a bending actuator. In the initial state, the microvalve is normally open, as the diaphragm is bent in upward direction due to stresses imprinted by the manufacturing process described later. In non-actuated state, the NO microvalve allows for fluid flow from the inlet to the outlet. Using the inverse piezoelectric effect, the valve opens further when a negative electric field is applied. Under a positive electric field, closing of the valve is achieved when the actuator diaphragm is pressed tightly onto the valve seat. In this closed state, a low leakage rate of the microvalve is crucial for medical applications and can be drastically reduced by optimizing its sealing properties. To this end, we discuss impact parameters on sealing properties and introduce selected measures for low leakage in closed state: a concentric trench design, a high force actuator diaphragm, and additional coating on the valve seat.

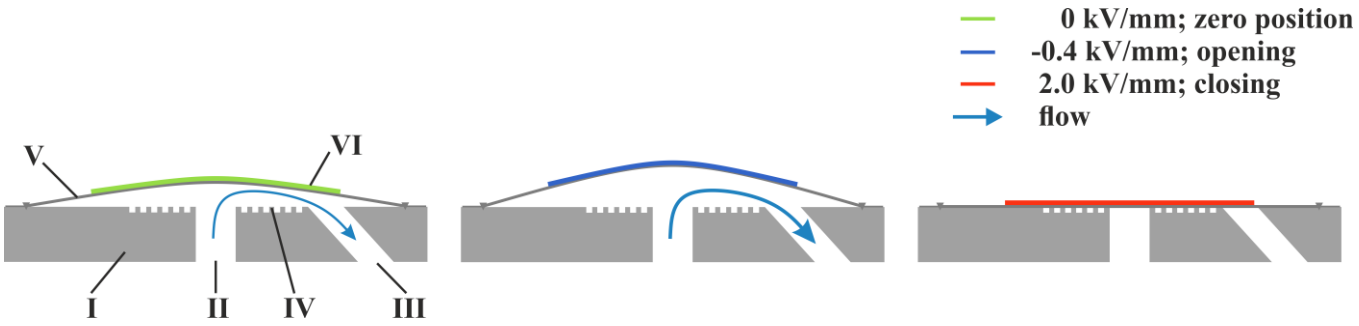

Figure 1. Working principle of the diaphragm-type piezoelectric NO valve. In non-actuated state, the valve is open and allows for fluid flow. By piezoelectric actuation, a negative electric field opens the valve further, resulting in reduced fluidic resistance, and a high positive field closes the fluid path by exerting a high contact pressure on the valve seat.

In principle, tight sealing of a diaphragm-type microvalve is achieved by high contact pressure exerted by the actuator pressing the diaphragm onto a valve seat designed for low leakage. Therefore, both the piezoelectric bending actuator and the geometric design of the valve seat can be adapted to achieve optimal performance. Analogously to microvalves presented in research for low leakage gas applications [22–24], a valve seat design for low leakage can be realized by a concentric trench design (see Figure 2). In comparison to a flat valve seat, this design exhibits multiple beneficial effects towards leakage reduction. Firstly, a reduction in the contact area of the valve diaphragm and valve seat increases the contact pressure at the interface. A second effect results from increased surface friction of the fluid over the increased valve seat surface, eventually causing lower leakage flow. Finally, the fluid flowing over the valve seat exerts shear stress relative to the confined, resting fluid in the trenches, leading to a cascade of pressure losses across each trench.

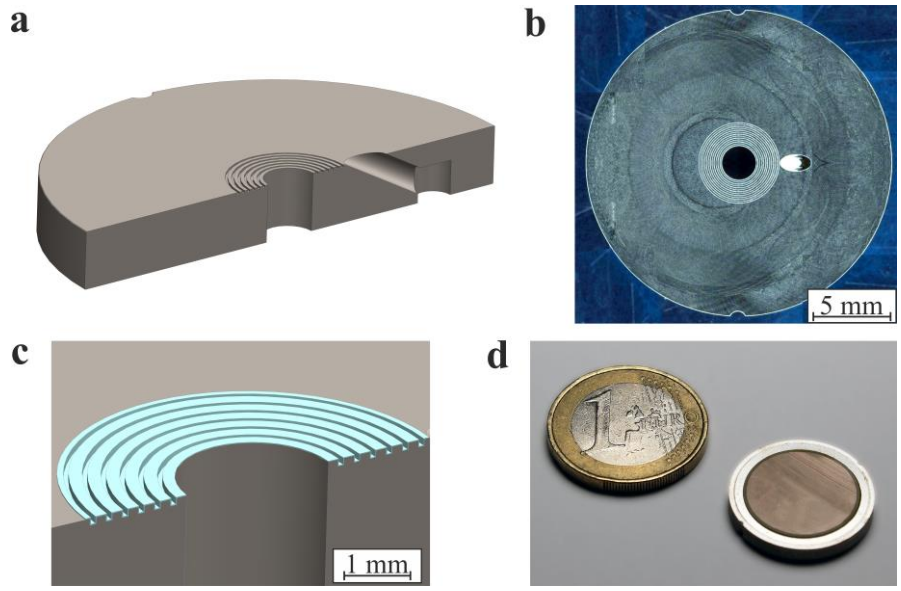

Figure 2. (**a**) Model of the NO valve body incorporating two fluid ports and micromachined trenches. (**b**) Light microscope picture of the micromachined valve steel body. (**c**) Model of the valve seat coated with Parylene-C. (**d**) Photograph of an assembled microvalve after laser welding and piezoelectric actuator bonding next to a Euro coin. The microvalve has a diameter of 20 mm and a height of 2.6 mm.

To further enhance sealing, the contact pressure on the valve seat exerted by the valve diaphragm can be increased with a piezoelectric actuator that exhibits higher forces. For piezoelectric bulk material, this can be achieved by increasing the thickness of the actuator, resulting in a higher force when actuated by the same electric field.

Another method of modifying the leakage of two surfaces in contact is to use coatings to enhance their surface properties with a view to increased sealing behavior. A good candidate is Parylene-C, a chemically inert, biocompatible polymer with beneficial mechanical properties frequently used in medical applications [25]. As the Young's modulus of Parylene-C is two orders of magnitude smaller than the Young's modulus of steel [26,27], the polymer's elasticity can be used to create a tight sealing in microvalves [22].

In order to evaluate the potential of each of the mentioned design measures and their impact on the performance of the microvalve, we design and manufacture them in different variants with respect to geometrical dimensions, structuring of the valve seat, and additional coating.

Figure 2a shows the basic design of the presented NO microvalve. A rigid metal body comprises two fluid ports and concentric trenches, creating the valve seat—both the width and depth of each trench amount to 100 µm. The diameter of the innermost trench is 2.5 mm, and all 6 trenches are evenly spaced concentrically with a distance of 150 µm from

each other. The NO microvalve is manufactured from stainless steel, which offers high resistance to plastic deformation, high machinability, and biocompatible properties [28].

Structuring of the baseplate (see Figure 2b), including valve seat trenches, is achieved by high precision milling (Kern Evo, Kern Microtechnik GmbH), resulting in valve seat trench depths of (101.8 ± 3) µm. A metal actuator foil, etched from a cold-rolled stainless steel sheet material, is joined to the valve body by laser welding using a fiber laser (1070 nm wavelength ytterbium fiber laser YLR-1000 SM, IPG Laser GmbH). We ensure hermetic sealing of the valve chamber and high strength of the weld seam by firm clamping of the foil onto the baseplate and an overflow of the welding area with shielding gas (Argon 4.6) at room temperature. During laser welding, the actuator foil experiences a temperature gradient from the welding fusion zone to zones not affected by heat, and after the molten steel solidifies, residual stresses remain in the actuator foil. These residual stresses ultimately result in an initial deflection of the actuator foil in an upwards direction and establish the NO state of the microvalve. After laser welding, the piezoelectric bending actuator is created by gluing a lead zirconate titanate (PZT) disc actuator onto the metal actuator diaphragm using a two-component epoxy glue (EPO-TEK 353ND).

We investigate three variants of the microvalve with micromachined trenches. A basic design comprises a 0.1 mm thick steel diaphragm as well as a 0.2 mm thick PZT actuator and is fabricated in a quantity of 10. In the coated design, the effect of a 15 µm Parylene-C coating on the valve seat (see Figure 2c) is investigated with another 10 manufactured valves with the same bending actuator as the basic design. In a third high force design, 5 microvalves without coating on the valve seat are fabricated with a 0.15 mm thick steel diaphragm and a 0.3 mm thick PZT actuator in order to increase the contact pressure exerted to the valve seat by the actuator. Table 1 provides an overview of all three manufactured design variants of the NO microvalve.

Table 1. Overview on fabricated NO microvalve variants.

Microvalve Design Variant	Number of Fabricated Valves	Valve Seat Coating	Piezoceramic Thickness	Metal Diaphragm Thickness
Basic design	n = 10	No coating	0.2 mm	0.1 mm
Coated design	n = 10	(15 ± 2.5) µm Parylene-C coating	0.2 mm	0.1 mm
High force design	n = 5	No coating	0.3 mm	0.15 mm

For realizing the coating of the valve seat, we use chemical vapor deposition of Parylene-C. To this end, the steel bodies are masked using a structured semiconductor wafer processing tape (Nitto SWT 10+R), limiting the coated surface to the trench area of the microvalve. Coating via Gorham route [29] is achieved in a plasma coating system (Plasma Parylene LC 300 RW, Plasma Parylene Systems GmbH). Under vacuum conditions, the substrates are pretreated with Silane A-174 for in-situ silanization from the gas phase at room temperature. Subsequently, 25 g of Parylene-C dimer is sublimed at 130 °C followed by pyrolysis into reactive monomers at 740 °C, and final polymerization takes place in the coating chamber at room temperature. A coating process duration of approximately 4 h results in a (15 ± 2.5) µm thickness of the coating layer. Removal of the mask is enabled by laser ablation using an infrared CO_2 laser (10.6 µm wavelength Speedy 360, TROTEC Laser GmbH), since mechanical stripping alone causes delamination of the coating. Finally, we proceed with the preparation of the coated steel bodies equivalently to the uncoated valves: we attach the steel actuator foil to the valve body by laser welding, followed by glue bonding of the PZT on top of the diaphragm (Figure 2d).

2.2. Parameter Studies of Valve Seat Design Using FEA

In order to investigate the impact of the geometrical dimensions of the circular trenches on the fluidic resistance of the valve seat and, hence, on the potential improvement with respect to its fluidic performance, we perform a finite element analysis (FEA). To this end,

we compare the fluid flow through an axisymmetric, annular channel with concentric trenches to the flow between two unstructured flat and parallel discs. The used simulation model is shown in Figure 3 and neglects the inlet and outlet tubes. Instead, we assume a radially symmetric outflow in the direction of the trench cavities leaving along the outer rim of the annular channel, which resembles the valve chamber. As an additional simplification, we assume a constant height along the channel. These assumptions overestimate the total flow rate compared to the real geometry. However, as we are interested in the relative changes of the fluidic resistance due to geometrical changes in the trench geometries and compared to the trenchless disc geometry, this is deemed as an acceptable error.

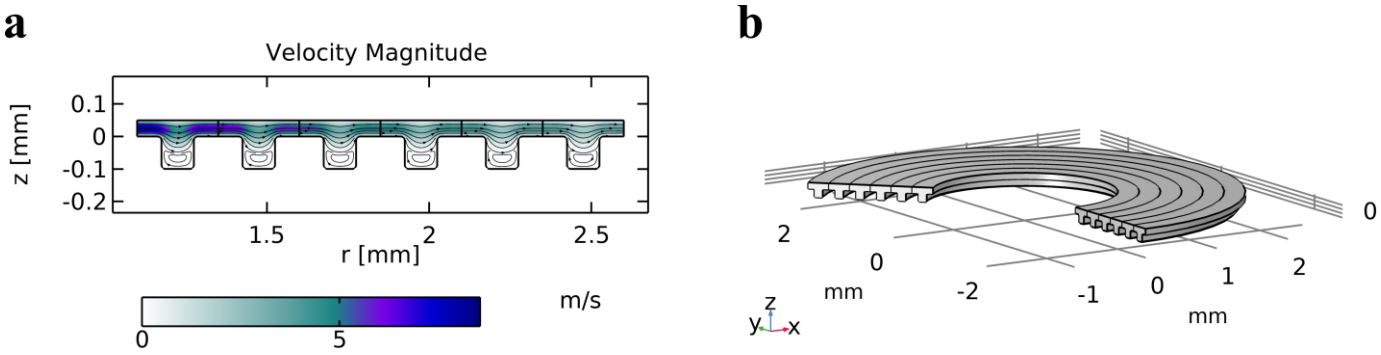

Figure 3. Simulation model used to evaluate the impact of concentric, ring-shaped trenches on the fluidic resistance of the valve seat. (**a**) Cross-sectional view of the two-dimensional simulation domain. (**b**) Section of the axisymmetric model. The arrows visualize the fluid flow from the inner to the outer boundary, as well as the vortices developing in the trench.

Figure 3a shows the two-dimensional simulation domain, which represents the cross-section of the partially depicted axisymmetric model of the right part of Figure 3b. The inlet is located at x = 0. The boundary at x = 2.7 mm is an open boundary. All other boundaries are defined as walls with a no-slip condition. For the inflow, the velocity field is specified to be fully developed at an average pressure level of 20 kPa, and we solve for a stationary and laminar flow of water at room temperature.

To study the different effects of the geometry on the fluidic resistance of this arrangement when the microvalve is open, we vary the height of the valve chamber, as well as the height and width of the concentric trenches, and determine the fluidic resistance, which is calculated as the ratio of the pressure drop Δp and the flow rate $\dot{q}$. We use the resistance of two parallel discs as a reference in order to evaluate and quantify the relative changes due to the geometric variation of the valve seat trenches. This resistance is calculated analytically to:

$$\frac{\Delta p}{\dot{q}} = \frac{6\mu}{\pi h^3} \ln \frac{r_1}{r_0}, \tag{1}$$

where r_0 is the inner radius, r_1 the outer radius, h the height of the valve chamber, and μ the viscosity of the fluid. A detailed derivation of this formula is given in Appendix A. The formula is valid for small Reynold's numbers and Newtonian fluids and does not account for the trench geometry. The reason for the latter is that the presence of trenches leads to the formation of vortices, whose size and vorticity depend non-linearly on the surrounding conditions such as the fluid velocities above and below these vortices, the wall distances, as well as the viscosity of the fluid. As the incorporation of these dependencies is challenging, we deem a comparison between a trench geometry and two parallel discs to be sufficient to evaluate the effects caused by the trenches.

The FEA is carried out with the software package COMSOL Multiphysics. In addition to the above-mentioned approximations, we replace the right angles at the trenches with small circular arcs. This is motivated by a better convergence behavior and a smaller numerical error due to the smoother boundary and, additionally, reflects the real micromachined

structure much better than a sharp right angle. In order to avoid significant changes in the results by introducing these radii, they are kept small enough.

Our FEA does not include the analysis of fluidic leakage of the microvalve in closed state. The leakage flow is caused by the imperfect contact between the diaphragm and the valve seat, which in turn is a result of the surface roughness of the solid bodies, as well as plastic deformations due to thermal stresses caused by laser welding. These specific values cannot be readily incorporated into an FEA. Moreover, when the diaphragm establishes or loses contact with the valve body, the topology of the fluidic domain between them changes, leading to node definition errors. A typical remedy to this problem is to introduce a small non-vanishing fluid domain between the diaphragm and the valve. As this adds artificial leakage to the overall results, such an approach would defeat the attempt to attain deeper and more sophisticated insights into the real fluidic leakage. Instead, we derive an analytical model to calculate the leakage rate in closed state, which is presented in the following section.

2.3. Analytical Modeling of Leakage Rates

In this section, an analytical model for the estimation of the leakage rates of the NO valves in closed state is presented. Leakage is the result of imperfect contact between the steel foil and the steel valve body due to surface roughness. In order to evaluate the leakage flow, we first determine the average separation between the steel diaphragm and the valve seat. This separation represents the height of the microchannel, determining the pressure-dependent flow rate. In order to solve this problem, we apply the approach of Persson [30], who studied the contact problem of two solids with surface roughness squeezed against each other. This leads to the average separation $u(p_{contact})$ between the steel diaphragm and the valve body as a function of the contact pressure $p_{contact}$:

$$u(p_{contact}) = \gamma\alpha^{-1}h_{rms}\log\left(\beta\epsilon q_0 h_{rms}\frac{E^*}{p_{contact}}\right) \tag{2}$$

where the constant γ is set to one, which means assuming perfectly elastic deformation, α and β are surface roughness constants, h_{rms} is the root mean square of the surface roughness, ϵ is a constant related to the power spectrum of the surface roughness $C(q)$ and the lower and upper cutoff wave vectors q_0 and q_1 of the surface, and E* the plane-strain modulus. The contact pressure $p_{contact}$ of the two bodies is equivalent to the maximum force exerted by the actuator diaphragm. The so-called blocking pressure p_{block} of the actuator is scaled by the ratio of valve diaphragm surface to the contact area to achieve the contact pressure and can be calculated according to [31]:

$$p_{\text{contact}} = \frac{A_{diaphragm}}{A_{\text{contact}}}\, p_{\text{block}} \tag{3}$$

Comprehensive derivations of Equations (2) and (3) are provided in Appendix B.

Applying Equation (2), we are now able to calculate the leakage flow rate depending on the pressure drop over the closed valve. To this end, an appropriate flow model of the leakage flow of water through microscale channels and openings must be developed. Since water can be considered as an incompressible fluid [32] and the Reynolds number is (as in almost all microfluidic applications) much smaller than 1 [33], the flow is modeled as a simple laminar Poiseuille flow driven by the pressure difference Δp between the inlet and the outlet of the valve. The channel geometry is determined by the design of the sealing and the average surface separation due to surface roughness. The average separation height is on the order of some micrometers, whereas the sealing dimensions are 2–3 orders of magnitude higher. Therefore, the leakage channel is assumed to be a rectangular slit, whose width w is much larger than its height $h = u(p)$, so that the side walls of the channel can be neglected, and the geometry can be regarded as a channel between two infinite

plates [34]. Applying no-slip boundary conditions $v(z = 0) = v(z = h) = 0$, the velocity profile and resulting flow rate are given by:

$$v_x(z) = \frac{\Delta p}{2\mu L}((h - z)z), \tag{4}$$

$$Q = \int_0^w dy \int_0^h dz\, v_x = \frac{h^3 w}{12\mu}\frac{\Delta p}{L}, \tag{5}$$

where μ is the viscosity of water.

The above-described geometrical simplification leads to a worst-case scenario estimation of the leakage rate; therefore, it is expected that the analytical model overestimates the observable leakage rate and constitutes an upper limit for the evaluation of the manufacturing-induced imperfections of the valve and the hereof resulting potential issues in its reliability in the medical application.

2.4. Experimental Characterization

The mechanical and fluidic characteristics of the NO valve are extensively tested in order to assess its performance and to estimate its reliability in the field. Additionally, the measurements are used to extract parameters necessary for model calibration, theoretical design studies, and analytical calculations of the leakage rates.

The operation of the diaphragm microvalve is fundamentally defined by the piezoelectrically driven diaphragm movement. Free actuator movement is allowed in open state of the microvalve, whereas further actuator movement is restricted when the actuator sits down on the valve seat in closed state. The mechanical stroke of the actuator diaphragm is measured optically using a white light profilometer (Fries Research and Technology; sensor range of 3 mm, maximal resolution of 30 nm) with a quasi-static voltage actuation (amplifier SVR 500-3, piezosystem jena GmbH) ranging from -0.4 kV/mm to 2.0 kV/mm to detect field-dependent open and closed state. Repetitive measurements using this setup reveal a measurement accuracy of the total actuator stroke of 2 µm. Additionally, the profilometer is used for surface inspection of the microvalve steel diaphragms in order to determine the fractal dimension as well as the maximum and minimum wave vectors q_0 and q_1 of the surface, respectively, serving as input parameters for analytical leakage modeling (see Section 2.3).

Subsequently, all manufactured valves are characterized with a view to the fluidic performance using deionized water at room temperature. The instruments used for these investigations are Coriflow sensors of different ranges (Bronkhorst MINI CORI-FLOW M14: range 0.5 mL/min to 167 mL/min, accuracy: $\pm$0.2% and ML120V00: range 0.8 µL/min to 500 µL/min, accuracy: $\pm$0.2%) as well as a pressure controller (Mensor CPC3000; range -50 kPa to 200 kPa, accuracy: $\pm$50 Pa).

Applying this measurement setup, the assembled microvalves undergo different fluidic tests. As an initial characterization, we measure their pressure-dependent NO flow rate, their quasi-static opening and closing flow characteristics, and the closed state leakage rate. NO flow rates are evaluated without electrical actuation of the piezoceramic and increasing water pressure at the inlet of the microvalve up to 100 kPa. Quasi-static opening and closing characterization of the microvalve at an inlet pressure of 20 kPa is achieved by sinusoidal actuation of the piezoceramic at a frequency of f = 0.01 Hz and electric fields between -0.4 kV/mm and 2.0 kV/mm. For evaluations of the pressure-dependent leakage rate, the valve's inlet pressure is increased from 0 kPa to 20 kPa, while the piezoceramic is subjected to a constant electric field of 2.0 kV/mm.

Finally, a fatigue test of the microvalves is performed with 5 microvalves of each design variant. The valves are operated at a constant fluidic pressure load of 20 kPa, a sinusoidal electric signal of 100 Hz, and an electric field of -0.4 kV/mm to 2.0 kV/mm for 1×10^6 actuation cycles. After this long-term excitation, the above-described fluidic

characterization methods are repeated in order to evaluate the fatigue of the microvalves, e.g., in terms of increased leakage rates or piezoceramic material failure.

3. Results and Discussion

The variants of the NO microvalve without additional and moving sealing components listed in Table 1 are designed, manufactured, and investigated applying the methods described in Section 2. At first, the optimal geometric dimensions of the microstructured valve seat are investigated in an FEA parameter study in order to estimate the impact of the concentric trenches on the fluidic resistance and, hence, on the open state flow rates. Applying the analytical model of Section 2.3., the pressure-dependent leakage rates of the different valve geometries are calculated and compared to measurements, and finally, the performance and long-term operation of all variants are evaluated experimentally.

3.1. Parameter Study: Impact of Microstructured Valve Seat

The impact of the trenches on the flow field is an essential element of the working principle of the NO microvalve. We perform a detailed FEA parameter study in order to evaluate the fluidic resistance of the valve comprising the valve seat trenches for varying channel height, trench width, and trench depth. Figure 4 provides an overview of the dependencies of the fluidic resistance on the varied geometric parameters.

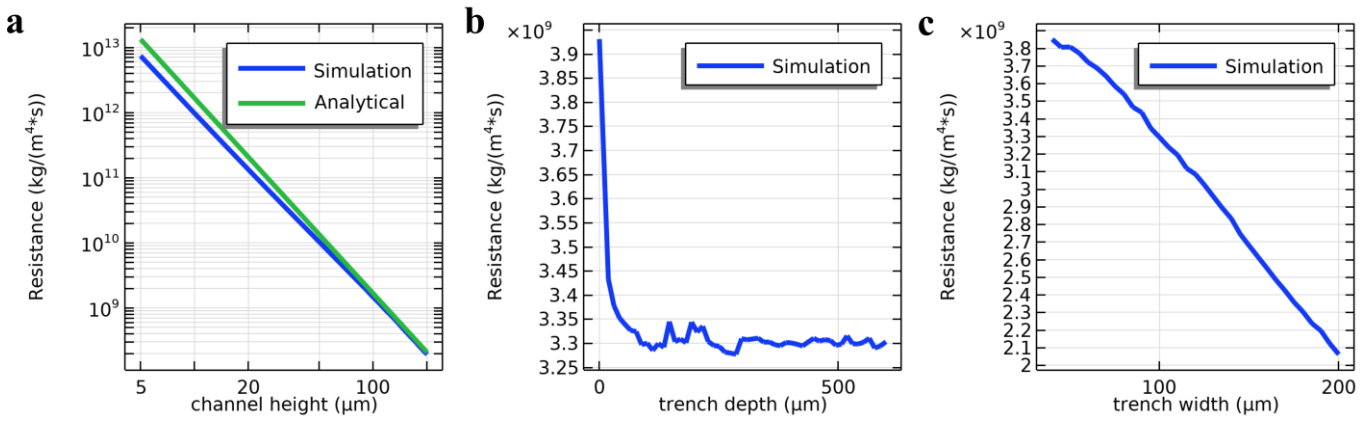

Figure 4. (**a**) Fluidic resistance as a function of the height of the channel above the trenches. (**b**) Fluidic resistance depending on the depth of the trenches; the analytically calculated resistance at zero depth amounts to 3.9×10^9 kg/m^{4}s. (**c**) Fluidic resistance for varying width of the trenches. Again, the resistance at zero width amounts to 3.9×10^9 kg/m^{4}s.

The dependency of the fluidic resistance on the channel height is presented in Figure 4a, which we obtain by varying the channel height from 5 µm to 200 µm, while other geometric parameters are set to the corresponding values of the manufactured design. For larger channel heights, the resistance converges against the analytically calculated resistance given in Equation (1). As shown in Figure 5, vortices develop inside the trenches, but their impact on the fluidic resistance becomes less relevant as the channel height increases.

The channel height itself is not a static design parameter of the valve but ultimately varies with the actuation of the piezoceramic actuator as well as with the inlet pressure depending on the elastic constants of the actuator diaphragm; hence, the simulations provide insight into the influences of the trenches in the microvalve's open state. The results indicate that this sealing concept is suitable for functional open state flow through the valve, as this trench design does not impede open state flow by an eventually increased fluidic resistance.

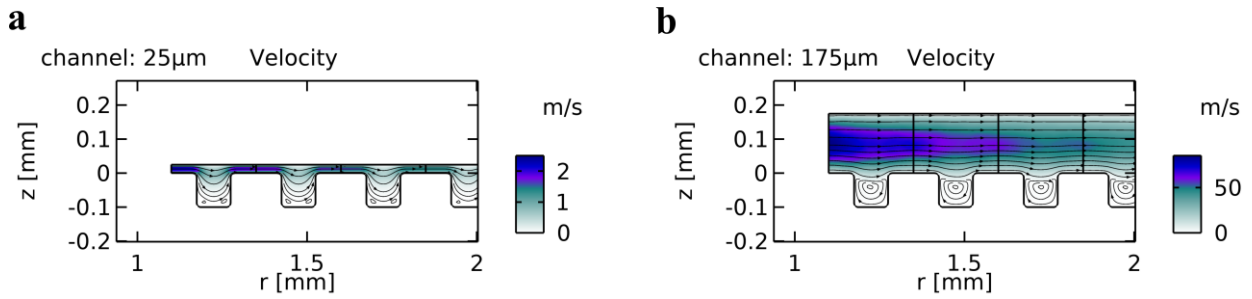

Figure 5. (**a**) Velocity field of the flow for a channel height of 25 µm. (**b**) Velocity field of the flow for a channel height of 175 µm. Vortices develop inside the trenches, having impact on the fluidic resistance; however, this impact decreases with increasing channel height.

Figure 4b shows the dependency of the fluidic resistance on the depth of the trenches at a channel height of 75 µm. The width of the individual trench is 100 µm. It reveals that the width of 100 µm limits the size of the arising vortices contributing to the resistance. Figure 6a shows the typical flow for shallow trenches with a larger width than depth. In this case, small vortices arise only in the trench corners, and the flow is mostly uniform. Increasing the depth, the fluidic resistance decreases until a depth of the trenches of about 150 µm (c.f. Figure 4b). For this specific trench geometry, the first vortices are now fully developed. Increasing the depth even further leads to more vortices; however, these also affect each other and exert a shear-stress-based resistance towards the neighboring vortices, as can be seen in Figure 6b. The vortices become weaker the deeper they are located in the trench. Due to this, the resistance does not change much for larger trench depths and saturates at an about 20% lower value than the analytically calculated value for a channel between two parallel discs without trenches.

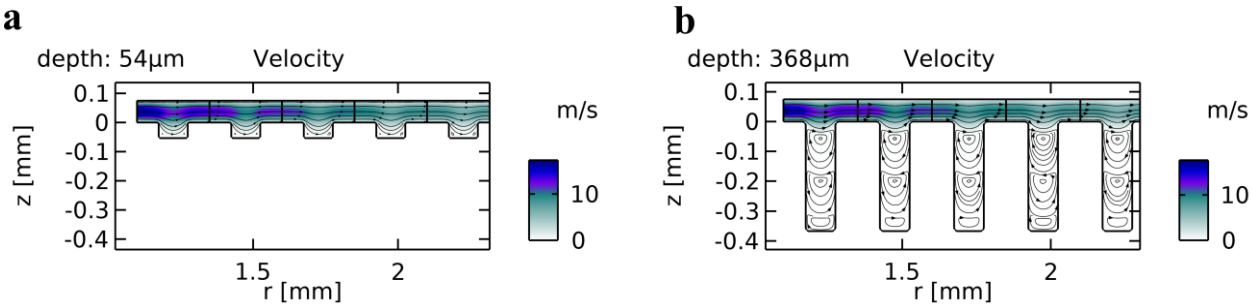

Figure 6. (**a**) Flow field for a trench depth of 54 µm. (**b**) Flow field for a trench depth of 368 µm. Several induced vortices interact with each other, causing shear stress towards themselves, rendering deeper vortices irrelevant for the main leakage flow. The diameter of the vortices depends on the width of the trenches, which here amounts to 100 µm.

The oscillating behavior of the fluidic resistance in Figure 4b can be explained by the discrete nature of the vortices, as fractional vortices cannot exist. In the beginning, the resistance becomes smaller with deeper trenches, as the fluid experiences less friction with the walls and is less confined. Once the depth reaches the same value as the trench width, the first vortex is formed, causing an increase in resistance. Increasing the depth further leads to a smaller resistance at first until the next vortex establishes. However, the more vortices are created inside the trench, the less they contribute to the overall resistance, as they interact more and more with each other than with the main flow field.

Finally, the effect of the trench width on the fluidic resistance is depicted in Figure 4c. The resistance decreases with the increasing width of the trenches as the individual fluid domains in those trenches become less restricted by the trench walls, ultimately leading to lower pressure losses due to the exerted shear stress. Figure 7a shows the flow field for a trench width of 100 µm and Figure 7b for 180 µm wide trenches and a trench depth of

100 µm. Only very small vortices arise in the corners with a negligible contribution to the fluidic resistance. The results suggest that for a smaller width of the individual trenches, the formation of large vortices causes higher fluidic resistance of the valve.

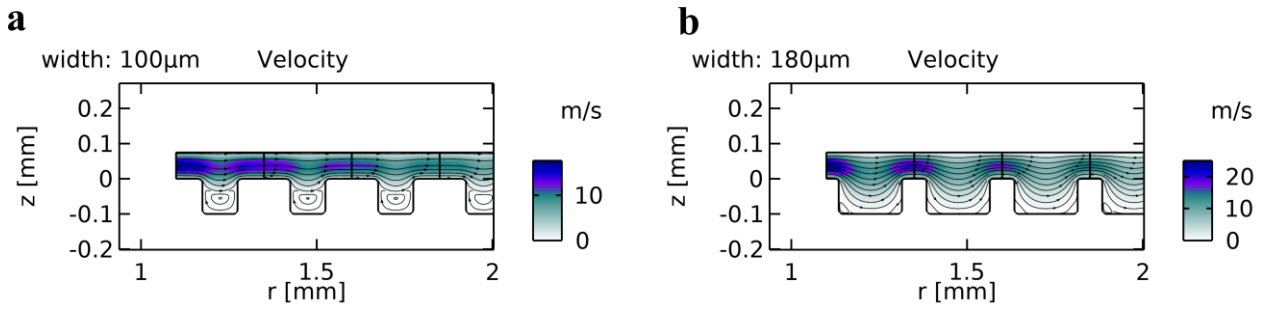

Figure 7. (**a**) Flow field for a width of the trenches of 100 µm. (**b**) Flow field for a width of the trenches of 180 µm, where no vortex generation is observed.

In conclusion, the FEA parameter study of the channel regions with integrated trenches of different geometrical dimensions shows a distinct and systematic impact on the fluidic resistance and, hence, on the open state flow behavior of the microvalves. The so-obtained deep understanding of their influence by flow-induced vortex generation enables to optimally design trenches with respect to width and depth of the individual trenches in order to create an appropriate flow resistance.

3.2. Modeling of Leakage Rate

Figure 8 depicts the pressure-dependent leakage rates in closed state of the introduced microvalve designs based on the analytical leakage model derived in Section 2.3. The depicted standard deviation is a result of the calculated propagation of manufacturing tolerances and uncertainties in material properties.

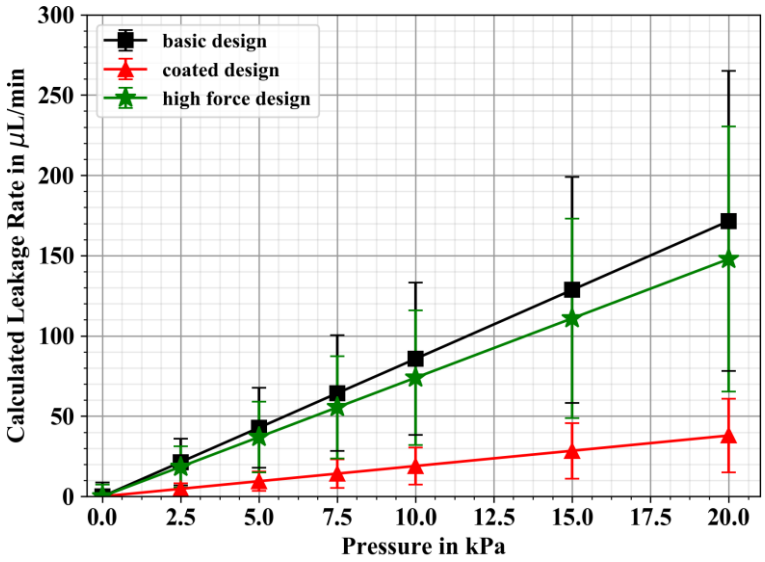

Figure 8. Analytically modelled pressure-dependent leakage rates for the three microvalve variants. Error bars show standard deviations based on calculated propagation of uncertainty of manufacturing and material tolerances.

The analytically calculated leakage rates show a clear linear dependency on the inlet pressure. The highest leakage of (171.5 ± 93.4) µL/min at 20 kPa is expected for the basic design. The high force design shows no significant change in leakage, where increased contact pressure of the valve diaphragm results only in a slightly reduced leakage of

(147.9 ± 82.6) µL/min at the same fluidic pressure applied. All microvalve design variants exhibit large standard deviations of about 60% due to high manufacturing tolerances of the steel actuator foils, propagating to high relative uncertainty in the calculated leakage rates. Coated microvalves show significantly reduced absolute values of leakage rates. The effective Young's modulus resulting from the Parylene-C-steel interface leads to a lower value of the average surface separation (see Equation (2)) and, consequently, leakage is expected to be as low as (37.9 ± 23) µL/min for an inlet pressure of 20 kPa, and, hence, is much lower than for the two other design variants. The theoretically determined leakage rates are compared to measured values of fabricated microvalves of the three designs; results are presented in Section 3.3.

3.3. Experimental Characterization

We investigate the characteristics and fluidic performance of the presented NO valve design variants (see Table 1). Out of the 5 manufactured high force design microvalves, one is excluded from the study due to insufficient glue bonding of the piezoceramic. The experimentally obtained actuator stroke, the open flow rates, and the results of the leakage measurements of all 24 tested microvalves are summarized in Table 2. Additionally, the calculated leakage rates based on the derived analytical models are provided for comparison.

Table 2. Overview of the experimental results for the three studied design variants of the NO microvalve.

Microvalve Design Variant	Tested Valves	Actuator Stroke, in µm	Max. Open Flow at 20 kPa, in mL/min	NO Flow at 100 kPa, in mL/min	Measured Leakage at 20 kPa, in µL/min	Calculated Leakage at 20 kPa, in µL/min
Basic design	10	56.4 ± 4.7	30.1 ± 3.4	122 ± 9	24.8 ± 9.6	171.5 ± 93.4
Coated design	10	51.6 ± 6.7	29.7 ± 4.5	119.1 ± 8.4	25.1 ± 7.9	37.9 ± 23
High force design	4	55.9 ± 2.6	24.9 ± 1.8	83.6 ± 4.8	19.8 ± 4.9	147.9 ± 82.6

Figure 9a depicts an exemplary measurement of the microvalve actuator stroke. The change in slope at approximately 1 kV/mm shows the actuator touch down on the valve seat. For electric fields <1 kV/mm, open state actuator movement of more than 50 µm in total is achieved, and the occurrence of piezoelectric hysteresis becomes apparent. Closed state starts at electric fields beyond 1 kV/mm, where further downwards displacement is blocked, and the contact pressure of the valve diaphragm and the valve seat increases. Comparison of the three variants of the microvalve design reveals no significant difference in total actuator stroke (Table 2). The slight difference in the stroke of the coated microvalves could be explained by the reduced distance of the valve diaphragm to the valve seat by the added coating.

Figure 9b shows an exemplary measurement of the field-dependent flow rates with discernible open and closed states. Due to the influence of piezoelectric hysteresis of the actuator, closed state of the microvalve is achieved at approximately 1.6 kV/mm for increasing fields, whereas for decreasing fields, the microvalve remains closed until a field of approximately 0.6 kV/mm. Active opening of the valve is facilitated by further upwards movement of the diaphragm at negative fields, where maximal open flow rates are achieved. For microvalves with a 0.2 mm thick piezoelectric actuator, similar maximal open flow rates of (30.1 ± 3.4) mL/min (basic design) and (29.7 ± 4.5) mL/min (coated design) are measured. In contrast, the microvalves with a 0.3 mm thick piezoactuator show lower maximal open flow rates of (24.9 ± 1.8) mL/min, most likely due to increased stiffness of the valve diaphragm: The fluidic pressure acting on the valve diaphragm displaces it further upwards for the less stiff actuators with a 0.2 mm thick piezoceramic, enabling even higher flow rates due to the increased height of the valve chamber. The increased stiffness of the valve diaphragm for 0.3 mm piezoactuator valves impedes additional displacement of the diaphragm induced by fluid pressure, resulting in a lower maximum open flow.

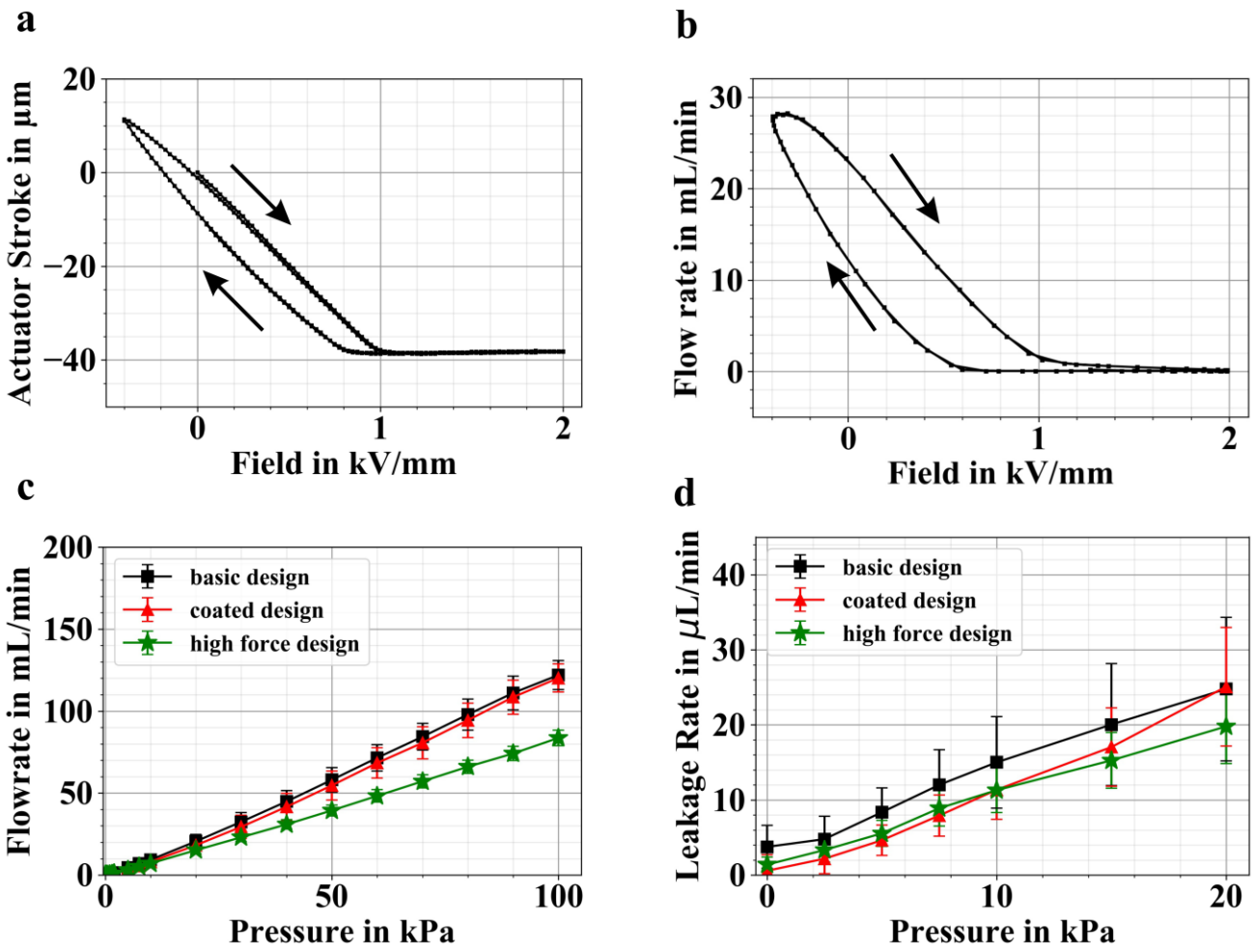

Figure 9. (**a**) Typical stroke measurement of the NO valve. At an applied field of approximately 1 kV/mm, the actuator diaphragm sits on the valve seat, and downwards movement is inhibited. (**b**) Typical flow characteristic of an NO valve at an inlet pressure of 20 kPa showing complete blockage of the fluidic path at approximately 1.6 kV/mm and a maximum open flow of 27 mL/min. (**c**) Average pressure-dependent flow rate in non-actuated state with an applied inlet pressure of up to 100 kPa. Error bars depict standard deviations. (**d**) Average pressure-dependent leakage with up to 20 kPa inlet pressure. Error bars depict standard deviations.

Another important parameter of microvalves as fundamental components of microfluidic systems is their fluidic resistance in open state, which ideally should not impede the fluid flow. In order to investigate this parameter, we measure the flow rates through the NO valve in non-actuated state. As the inlet pressure increases, flow rates in NO state increase linearly for all microvalve designs, as shown in Figure 9c. Same as for active opening, a difference of the flow rate in NO state is observed when comparing the 0.2 mm piezoactuator valve variants ((122 ± 9) mL/min for the basic design and (119.1 ± 8.4) mL/min with coating) to the high force design ((83.6 ± 4.8) mL/min). Again, this difference can be explained by the dissimilar stiffnesses of the valve diaphragms and the effect of the fluid pressure influencing the height of the valve chamber.

Microvalve leakage is presented in Figure 9d. The pressure-dependent leakage characteristic of NO valves of the basic design seem to exhibit the highest of all measured leakage behaviors; however, the differences are not statistically significant (Table 2).

While microvalves of the high force actuator variant exhibit the lowest leakage rates at the lowest standard deviations, better statistics are needed to assess the significance of the observed differences in order to evaluate the effect of an increased contact pressure. Since experimental leakage rates of the coated microvalves do not differ from the basic design, beneficial sealing properties as a result of the Parylene-C coating cannot be derived to this

date. However, the comparison of the measured leakage rates to former investigations of NO valves with soft sealing components [14] reveals that the microvalve variants presented here achieve similar leakage rates with significantly lower standard deviations. Therefore, the micromachined trenches are proven suitable for the fabrication of a microvalve with increased reliability with a view to sample-to-sample variation of the exhibited leakage rate due to higher manufacturing precision of the valve seat compared to microvalves comprising an O-ring soft sealing.

Comparison of the modeled values (see Figure 8) to experimentally collected data shows an overall overestimation of expected leakage rates, which, as already mentioned, constitutes an upper limit of the theoretically expected values. While leakages of both microvalve variants without coatings are overestimated approximately by a factor of 4 and 7 (high force design and basic design, respectively), the analytically calculated leakage rates of the coated microvalves differ from experimental data only by a factor of 1.5. Future work on analytical modeling of microvalve leakage rates should consequently involve a thorough investigation of contact pressure calculation accompanied by experimental investigation of the achieved forces of piezoceramics bonded to metal diaphragms.

3.4. Fatigue Test

A reliable and safe microfluidic device design is required in medical applications in order to minimize the risk of device failure. Hence, the stability of the microvalves' performance is investigated by subjecting them to fatigue testing as described in Section 2.4.

Immediately after fatigue testing, we inspect the microvalve's piezoceramic actuator optically and by measurement of its electric capacitance in order to detect critical failure in the form of cracks. Valves with piezoceramic actuator failure are excluded from subsequent fluidic characterization. The changes in maximum open flow, NO flow, and leakage after fatigue testing compared to observed performances after manufacturing are summarized in Table 3.

Table 3. Results of 1×10^6 actuation fatigue test. Listed as piezoceramic actuator failures are observed material failures of the PZT in form of cracks. Change in fluidic performance is given for valves with functional piezoceramic actuator.

Microvalve Design Variants	Fatigue Tested Valves	Piezoceramic Actuator Failures	Change of Max. Open Flow, 20 kPa	Change of NO Flow, 100 kPa	Change of Leakage, 20 kPa
Basic design	5	3	$(-6 \pm 3)\%$	$(8 \pm 4)\%$	$(123 \pm 62)\%$
Coated design	5	2	$(-2 \pm 2)\%$	$(0 \pm 11)\%$	$(3 \pm 13)\%$
High force design	4	0	$(6 \pm 4)\%$	$(18 \pm 8)\%$	$(14 \pm 15)\%$

None of the 4 high force design valves show failure of the piezoceramic actuator, but a total of 5 out of the 10 tested microvalves with a 0.2 mm thick piezoceramic actuator experience material cracking of the piezoceramic (three basic design valves and two coated valves). To confirm increased robustness of the actuator with increased actuator thickness, further investigations with an increased number of samples are needed and are planned for future work.

Characterization of the active open flow rate shows only small changes (Table 3). The average change of NO flow rates at 100 kPa is zero for microvalves with coating, and is increased slightly for the basic design; for the high force design valves, the flow rates increases notably. Microvalves with coating exhibit the lowest change in leakage after fatigue testing, whereas an increase of 14% of leakage rates is observed for high force design valves, and a strong increase of 123% is found for valves of the basic design.

Though standard deviations of the measured changes in leakage rates are high, a tendency of the stability of the tested designs can be deduced. Both design adaptions of the basic design, the coated as well as the high force design, show lower increase in leakage rates after the fatigue tests. The valve seat coated with Parylene-C seems to favor a good seal of the valve diaphragm to the seat even after fatigue. Comparing valves of the high force design to those of the basic design, the stiffer actuator capable of higher compression

forces appears to exhibit higher robustness against fatigue testing regarding piezoceramic actuator failure as well as an increase in leakage rate. A larger number of samples for testing would be necessary for future studies to increase the statistical relevance of the results and further substantiate these findings.

4. Conclusions

This work provides a detailed investigation of NO microvalve development for medical applications, where many intricate requirements in flow performance, biocompatibility, hermetic sealing, and device reliability call for sophisticated solutions. We introduce a piezoelectric microvalve with multiple trenches serving as a valve seat and omit any movable soft sealing components in the valve chamber as an important step towards the reliable operation of the microfluidic device.

As alternatives for a soft sealing valve seat, we discuss different measures for optimized fluidic performance of the microvalve in closed state, provide insight into important influencing parameters of leakage rates, and propose three design variants of NO valves for fabrication and experimental characterization. Moreover, we derive an analytical model of the leakage rates and perform a dedicated FEA parameter study of the geometric dimensions of the trench design, enabling further NO valve optimization with a view to sealing performance as well as fluidic resistance.

The fabricated and tested microvalve variants with concentric trenches exhibit good leakage rates in closed state as low as (19.8 ± 4.9) µL/min. This is comparable to former investigations of NO valves with soft sealing components but with better controllability of geometric parameters, hence, a low sample-to-sample variation, which is substantiated by small standard deviations of the measured leakage. We show that flow rates in open state are as high as (30.1 ± 3.4) mL/min. Therefore, the presented sealing concept does not impede fluid flow, and malfunctions of the microvalve in open state are successfully avoided by the omittance of any additional movable components in the valve chamber. Fatigue testing of the microvalves reveals beneficial effects of Parylene-C coating or increased piezoelectric actuator force on leakage rate stability and indicates increased piezoceramic material stability with increased thickness.

Due to its simplistic design, energy-efficient piezoelectric actuation, and beneficial material properties, the microvalve with multiple valve seat trenches lays a valuable basis for microfluidic medical device development. The comprehensive investigation of microvalve design provided in this work enables well-founded further development of the microfluidic device. Potential future work on the development of microvalves for medical applications may include optimization of the piezoceramic disk actuator design for increased contact pressure, extended fatigue testing, as well as fluidic characterizations at human body temperature.

Author Contributions: Conceptualization, C.P.D. and G.S.; methodology, C.P.D.; software, W.H., P.K.M. and C.P.D.; validation, C.P.D., S.T.G., P.K.M., W.H. and G.S.; formal analysis, C.P.D. and W.H.; investigation, C.P.D. and S.T.G.; resources, C.P.D., S.T.G. and W.H.; data curation, C.P.D., S.T.G. and W.H.; writing—original draft preparation, C.P.D., P.K.M. and W.H.; writing—review and editing, C.P.D. and G.S.; visualization, C.P.D. and W.H.; supervision, G.S.; project administration, C.P.D. All authors have read and agreed to the published version of the manuscript.

Funding: This research was funded by the Bavarian Ministry of Economic Affairs, Regional Development and Energy, within the Bavarian funding program for research and development "Electronic Systems" under the grant number ESB071/002.

Data Availability Statement: The experimental, analytical modeling, and simulation data that support the findings of this study are available in Fordatis—ResearchData Repository of Fraunhofer-Gesellschaft with the identifier (https://fordatis.fraunhofer.de/handle/fordatis/218 (accessed on 4 August 2021)).

Acknowledgments: The authors would like to thank Christian Wald for funding acquisition as well as supervision of the research activity and Nivedha Surendran for assisting in our laboratory work. We are also thankful to Franz Selbmann from Fraunhofer ENAS for providing the Parylene-C deposition process parameters and topology data.

Conflicts of Interest: The authors declare no conflict of interest. The funders had no role in the design of the study; in the collection, analyses, or interpretation of data; in the writing of the manuscript, or in the decision to publish the results.

Appendix A. Derivation of the Fluidic Resistance of a Stationary and Laminar Flow between Two Parallel Discs

Appendix A.1. Governing Equations

Given two parallel discs with an inner radius r_0, an outer radius r_1 and a vertical distance h. We assume that the flow between these two plates is stationary and laminar. Additionally, we assume an incompressible, Newtonian fluid. Then the Navier–Stokes equations, representing conservation of momentum, are given as:

$$\rho\left(\vec{v}\cdot\nabla\right)\vec{v} = -\nabla p + \mu\Delta\vec{v} \tag{A1}$$

and the continuity equation, representing conservation of mass, is given as:

$$\nabla\cdot\vec{v} = 0. \tag{A2}$$

Here, $\rho = \text{const.}$ is the density and $\mu = \text{const.}$ is the viscosity of the fluid. The vector field $\vec{v}$ is the velocity field and p the pressure. In cylindrical coordinates, the continuity equation for the velocity field $\vec{v}(r,\varphi,z)$ is given by:

$$\frac{\partial v_r}{\partial r} + \frac{v_r}{r} + \frac{1}{r}\frac{\partial v_\varphi}{\partial\varphi} + \frac{\partial v_z}{\partial z} = 0. \tag{A3}$$

Due to the cylindrical symmetry, we assume that there is neither flow in azimuthal direction (swirl flow) nor in vertical direction resulting in $v_\varphi = v_z = 0$. Additionally, also all derivatives with respect to φ are zero. This results in the problem-adapted continuity equation:

$$\frac{\partial v_r}{\partial r} + \frac{v_r}{r} = 0. \tag{A4}$$

The Navier–Stokes equation for the radial velocity component then becomes:

$$\rho\cdot v_r\frac{\partial v_r}{\partial r} = -\frac{\partial p}{\partial r} + \mu\left(\frac{\partial^2 v_r}{\partial r^2} + \frac{1}{r}\frac{\partial v_r}{\partial r} - \frac{v_r}{r^2} + \frac{\partial^2 v_r}{\partial z^2}\right), \tag{A5}$$

and the remaining two equations become:

$$\frac{\partial p}{\partial\varphi} = \frac{\partial p}{\partial z} = 0. \tag{A6}$$

Thus, the pressure varies only with the radius.

Differentiating the continuity Equation (A4) with respect to r and substituting it into the Navier–Stokes equation yields:

$$\rho\cdot v_r\frac{\partial v_r}{\partial r} = -\frac{\partial p}{\partial r} + \mu\frac{\partial^2 v_r}{\partial z^2}. \tag{A7}$$

Appendix A.2. Dimensionless Formulation

We can rewrite the above equation in a non-dimensional formulation, using characteristic values of the single entities. This enables a better quantitative and qualitative

comparison between different geometrical variants. The radial velocity is then given as $v_r = v_c \cdot v_r^*$, the radius as $r = r_0 \cdot r^*$, the pressure as $p = p_0 \cdot p^*$ and the z-coordinate becomes $z = h \cdot z^*$, where v_c denotes a characteristic value for the velocity, r_0 and h denote the geometry parameters and p_0 is the input pressure.

The dimensionless equation is then given by:

$$\frac{\rho v_c h}{\mu} \cdot v_r^* \frac{\partial v_r^*}{\partial r^*} = -\frac{p_0 h}{v_c \mu} \cdot \frac{\partial p^*}{\partial r^*} + \frac{r_0}{h} \cdot \frac{\partial^2 v_r^*}{\partial z^{*2}}. \tag{A8}$$

We can identify the term $\frac{\rho v_c h}{\mu}$ as Reynold's number of the flow. Additionally defining $\alpha := \frac{p_0 h}{v_c \mu}$ and $\beta := \frac{r_0}{h}$ dropping the asterisk, we finally arrive at:

$$\mathrm{Re} \cdot v_r \frac{\partial v_r}{\partial r} = -\alpha \frac{\partial p}{\partial r} + \beta \frac{\partial^2 v_r}{\partial z^2}. \tag{A9}$$

Doing the same for the continuity equation and dropping the asterisks results in the same equation again, but then for dimensionless entities.

Appendix A.3. Derivation of the Non-Linear Differential Equation for the Radial Velocity

The continuity equation can be separated according to:

$$\frac{\mathrm{d}v_r}{v_r} = -\frac{\mathrm{d}r}{r}. \tag{A10}$$

Solving this differential equation leads to $v_r = \frac{C(z)}{r}$, where the function $C(z)$ depends only on z. Inserting this equation into the Navier–Stokes equation yields:

$$\mathrm{Re} \cdot \frac{C(z)}{r} \cdot \left(-\frac{C(z)}{r^2} \right) = -\alpha \frac{\partial p}{\partial r} + \beta \frac{C''(z)}{r} \tag{A11}$$

or respectively:

$$\beta \frac{C''}{r} + \mathrm{Re} \cdot \frac{C^2}{r^3} = \alpha \frac{\partial p}{\partial r}. \tag{A12}$$

Integrating this equation with respect to r within the interval $\left[1, \frac{r_1}{r_0}\right]$, i.e., the entire disc, we obtain the following non-linear equation for the radial component of the velocity:

$$\beta \ln \frac{r_1}{r_0} \cdot C'' + \left(\frac{1}{2} - \frac{r_0^2}{2 r_1^2} \right) \mathrm{Re} \cdot C^2 = -\alpha \cdot (p_0 - p_1). \tag{A13}$$

Appendix A.4. Linearization of the Differential Equation and Solution

In the microvalve under consideration, the radii are much larger than the vertical gap between the discs. Furthermore, we expect the flow to be rather creeping than turbulent. For example, a setting with $r_0 = 1.1$ mm, $r_1 = 2.6$ mm, $h = 25$ µm and $p_0 = 10$ kPa, leads to a maximum Reynold's number of about $\mathrm{Re} = 0.32$ in our simulations. The factor in front of the non-linear term then becomes about 0.13, while at the same time $\alpha \approx 295$ and $\beta = 44$. Thus, we can neglect the non-linear term, and we obtain:

$$C''(z) = -\frac{\gamma}{\ln \frac{r_1}{r_0}} \Delta p, \tag{A14}$$

where the dimensionless constant $\gamma = \frac{p_0 h^2}{\mu v_c r_0}$. For high Reynold's numbers, this simplification would not be appropriate, as then the turbulent flow contributes significantly to the fluidic resistance.

Equation (A14) can be integrated twice over the height of the channel between the discs to obtain a polynomial of second order with two constants of integration. These constants are determined by applying no-slip boundary conditions at the discs. The coordinate system is oriented in such a way that the discs are symmetrically placed above, and below the xy-plane, i.e., they are located at $z = \pm\frac{1}{2}$ in our dimension-less formulation. We then obtain:

$$C(z) = \frac{\gamma}{8 \ln \frac{r_1}{r_0}} \Delta p \cdot \left(1 - 4z^2\right) \tag{A15}$$

and further for the dimension-less velocity (added asterisks to clearly distinguish between entities with and without dimensions):

$$v_r^*(r^*, z^*) = \frac{p_0 h^2}{8 \mu v_c r_0} \frac{1}{\ln \frac{r_1}{r_0}} \frac{\Delta p^* \cdot \left(1 - 4z^{*2}\right)}{r^*}, \tag{A16}$$

and finally for the radial velocity:

$$v_r(r, z) = \frac{1}{8 \mu \ln \frac{r_1}{r_0}} \frac{\Delta p}{r} \left(h^2 - 4z^2\right). \tag{A17}$$

Appendix A.5. Calculation of the Flowrate and the Fluidic Resistance

The pressure-driven flow rate $\dot{q}$ between the two discs is obtained by integrating the radial velocity over the cylindrical surface with the height being the gap and the perimeter $r \cdot \mathrm{d}\varphi$. Exploiting the mirror symmetry around $z = 0$ leads to:

$$\dot{q}(r) = 2 \int_{z=0}^{\frac{h}{2}} \int_{\varphi=0}^{2\pi} v_r(r, z) r \, \mathrm{d}\varphi \, \mathrm{d}z. \tag{A18}$$

This yields:

$$\dot{q} = \frac{\pi h^3}{6 \mu \ln \frac{r_1}{r_0}} \Delta p. \tag{A19}$$

Finally, the resistance for a radial, stationary, laminar flow between two parallel discs is given by:

$$\frac{\Delta p}{\dot{q}} = \frac{6 \mu \ln \frac{r_1}{r_0}}{\pi h^3}. \tag{A20}$$

Appendix B. Derivation of the Model of the Leakage Rates

Appendix B.1. Persson's Theory of Contact Mechanics—Derivation of the Average Separation Height $u(p)$ of Two Contact Surfaces

Consider the frictionless contact between two elastic solids with surface profiles $h_1(x)$ and $h_2(x)$. The elastic contact problem of these solids is equivalent to the contact between a rigid solid (substrate) with surface profile $h(x) = h_1(x) + h_2(x)$ being in contact with an elastic solid (block) with a flat surface, whose Young's modulus E and Poisson ratio ν are given by [35]:

$$\frac{1 - \nu^2}{E} = \frac{1 - \nu_1^2}{E_1} + \frac{1 - \nu_2^2}{E_2}, \tag{A21}$$

where E_1, E_2 and ν_1, ν_2 are the Young's moduli and the Poisson ratios of the two solids, respectively. For the valves without Parylene coating, the effective Young's modulus for the steel-steel contact is of the same order of magnitude as the Young's modulus of stainless steel. For the valves with Parylene coating, the effective Young's modulus is significantly decreased since the Young's modulus of parylene is much smaller than the Young's modulus of steel [26,27].

The contact between the two surfaces depends on the pressure that squeezes them together. When the applied contact pressure p is increased, the average surface separation

u is decreased, so the pressure p is again a function of u: $p = p(u)$. In order to setup an equation, we consider the energy balance $U_{el}(u)$ stored in the deformed surface in the contact region and the mechanical work performed by the applied external pressure $p_{contact}$ [30]:

$$\int_u^\infty du' A_0 p(u') = U_{\mathrm{el}}(u) \tag{A22}$$

or equivalently:

$$p(u) = -\frac{1}{A_0}\frac{dU_{\mathrm{el}}}{du}, \tag{A23}$$

where A_0 is the nominal contact area. For small pressures, it can be assumed that the elastic energy is linearly proportional to the load, i.e., $U_{\mathrm{el}}(u) = u_0 A_0 p(u)$ [30]. The characteristic length u_0 depends on the surface roughness but not on the contact pressure [30]. Thus, Equation (A23) can be simplified to:

$$p(u) = -u_0\frac{dp}{du} \tag{A24}$$

Or:

$$p(u) = p_c e^{-u/u_0}, \tag{A25}$$

which is in good agreement with experimental data [30]. Many surfaces of interest are self-affine fractals for $q_0 < q < q_1$, where q_0 and q_1 are the lower and upper cutoff wave vectors. If a self-affine surface is magnified in a direction perpendicular to it, then the surface 'looks the same', i.e., the statistical properties of the surface are invariant under scale transformation. The surface roughness of a self-affine fractal can be described by a fractal geometry D_f with $2 < D_f < 3$, whereby a value of 2 corresponds to a perfectly smooth surface and the limiting case of $D_f = 3$ is equivalent to a three-dimensional body. For most surfaces, the fractal dimension is smaller than 2.3 [36]. Persson also derived expressions for p_c and u_0 for a self-affine fractal surface [30]. The final simplified expressions for the contact pressure $p(u)$ and the average surface separation $u(p)$ are given by:

$$p(u) = \beta\epsilon q_0 h_{rms} E^* e^{-\alpha u/\gamma h_{rms}} \tag{A26}$$

And:

$$u(p) = \gamma\alpha^{-1} h_{rms} \log\left(\beta\epsilon q_0 h_{rms}\frac{E^*}{p}\right). \tag{A27}$$

In the equations above, q_0 is the upper cutoff wavevector in the fractal analysis, h_{rms} is the root-mean-square value of the surface roughness, $E^* = E/\left(1-\nu^2\right)$ and $\epsilon = 0.7493$ [30]. The constant $\gamma < 1$ (but of order unity) takes into account that the contact is not perfect, and the elastic energy stored in the contact region is less than the average elastic energy [30]. For simplification, it is set to $\gamma = 1$ in the following calculations. α and β are factors in the context of the theory of contact mechanics and are functions of the fractal dimension and the ratio q_1/q_0. In the case of $D_f < 2.3$, both constants are nearly independent of the ratio q_1/q_0 and are approximately given by $\alpha \approx 1$ and $\beta \approx 0.5$ [30]. According to the Equation (A27), the average surface separation and, hence, the leakage path in the valves with parylene coating will be decreased since the value of E^* is much smaller, and the leakage rates are expected to be smaller than for the valves without Parylene.

Appendix B.2. Calculation of Contact Pressure $p_{contact}$

In a non-actuated state, the valve is open, and the fluid can pass through. Applying a positive voltage to the piezoceramic causes a deflection of the actuator towards the valve seat, whereas a negative voltage actively opens the valve and decreases its fluidic resistance. The stroke volume, which is the volume displaced by the piezoelectric actuator, depends

approximately linearly on the electrical excitation and the applied pressure difference at the diaphragm [31]:

$$V(p, E_z) = C_E \cdot (E_z - E_0) + C_p \cdot (p - p_0). \tag{A28}$$

Here, $E_z - E_0$ is the electric field applied to the piezoceramic with $E_0 = 0$, p_0 is the atmospheric pressure and C_E and C_p are the volumetrical-electrical coupling coefficient and the fluidic capacitance, respectively. In [31], both coefficients are calculated for a circular piezoceramic with radius R_1, which is bonded to a circular diaphragm with radius R_2 clamped at $r = R_2$. The expressions depend on the thicknesses of the piezoceramic and the diaphragm, their elastic moduli, the Poisson ratios of the piezoceramic and the diaphragm, and the piezoelectric coefficient d_{31}, that quantifies the stretching of the piezoceramic in the x_1-direction for an electric field applied in the x_3-direction.

To ensure blocking of the fluid, the force of the actuator must be larger than the force exerted to the diaphragm by the pressure of the fluid. The threshold pressure that is necessary to close the channel is called the blocking pressure. It depends on the properties of the piezoceramic material and the difference ΔU between the maximal actuation voltage and the minimum actuation voltage. The blocking pressure is defined as the pressure, where the stroke volume is zero and can be derived according to [31]:

$$p_{\text{block}} = -\frac{C_E^*}{C_p}(U_+ - U_-) + p_0. \tag{A29}$$

In the equation above, $C_E^* = C_E / d_P$ with d_P is the thickness of the piezoceramic layer, and U_+ and U_- are the electric voltages corresponding to the minimal and maximal position of the diaphragm. The contact pressure derived from contact mechanics is related to the blocking pressure. Since the blocking pressure is defined as the actuator force on the diaphragm, but the contact area is smaller than its total surface, the contact pressure is given by the blocking pressure multiplied by the ratio of these two areas. Therefore, the expression for the contact pressure is given by:

$$p_{\text{contact}} = \frac{A_{diaphragm}}{A_{\text{contact}}} p_{\text{block}} \tag{A30}$$

with $A_{diaphragm} / A_{\text{contact}} \approx 1.06$. This expression can be inserted into Equation (5) to calculate the average surface separation, which is the key parameter for estimating leakage flow rates in metal seals.

References

1. Moreno, M.; Aracil, C.; Quero, J.M. High-integrated microvalve for lab-on-chip biomedical applications. In *2008 IEEE Biomedical Circuits and Systems Conference, Baltimore, MD, USA, 20–22 November 2008*; IEEE: New York, NY, USA, 2009; pp. 313–316. ISBN 1424428785.
2. Qian, J.-Y.; Hou, C.-W.; Li, X.-J.; Jin, Z.-J. Actuation Mechanism of Microvalves: A Review. *Micromachines* **2020**, *11*, 172. [CrossRef] [PubMed]
3. Oh, K.; Ahn, C. A Review of Microvalves. *J. Micromech. Microeng.* **2006**, *16*, 13–39. [CrossRef]
4. Chappel, E. A Review of Passive Constant Flow Regulators for Microfluidic Applications. *Appl. Sci.* **2020**, *10*, 8858. [CrossRef]
5. Fazal, I.; Elwenspoek, M.C. Design and analysis of a high pressure piezoelectric actuated microvalve. *J. Micromech. Microeng.* **2007**, *17*, 2366–2379. [CrossRef]
6. Park, J.M.; Taylor, R.P.; Evans, A.T.; Brosten, T.R.; Nellis, G.F.; Klein, S.A.; Feller, J.R.; Salerno, L.; Gianchandani, Y.B. A piezoelectric microvalve for cryogenic applications. *J. Micromech. Microeng.* **2008**, *18*, 15023. [CrossRef]
7. Megnin, C.; Barth, J.; Kohl, M. A bistable SMA microvalve for 3/2-way control. *Sens. Actuators A Phys.* **2012**, *188*, 285–291. [CrossRef]
8. Kohl, M.; Dittmann, D.; Quandt, E.; Winzek, B. Thin film shape memory microvalves with adjustable operation temperature. *Sens. Actuators A Phys.* **2000**, *83*, 214–219. [CrossRef]
9. Kolari, K.; Havia, T.; Stuns, I.; Hjort, K. Flow restrictor silicon membrane microvalve actuated by optically controlled paraffin phase transition. *J. Micromech. Microeng.* **2014**, *24*, 84003. [CrossRef]
10. Yang, B.; Lin, Q. A latchable microvalve using phase change of paraffin wax. *Sens. Actuators A Phys.* **2007**, *134*, 194–200. [CrossRef]

11. Nafea, M.; Nawabjan, A.; Mohamed Ali, M.S. A wirelessly-controlled piezoelectric microvalve for regulated drug delivery. *Sens. Actuators A Phys.* **2018**, *279*, 191–203. [CrossRef]
12. Evans, A.T.; Park, J.M.; Chiravuri, S.; Gianchandani, Y.B. A low power, microvalve regulated architecture for drug delivery systems. *Biomed. Microdevices* **2010**, *12*, 159–168. [CrossRef]
13. Im, S.B.; Uddin, M.J.; Jin, G.J.; Shim, J.S. A disposable on-chip microvalve and pump for programmable microfluidics. *Lab Chip* **2018**, *18*, 1310–1319. [CrossRef]
14. Bußmann, A.B.; Durasiewicz, C.P.; Kibler, S.H.A.; Wald, C.K. Piezoelectric titanium based microfluidic pump and valves for implantable medical applications. *Sens. Actuators A Phys.* **2021**, *323*, 112649. [CrossRef]
15. Cheng, C.-H.; Chao, C.; Cheung, Y.-N.; Xiao, L.; Yang, M.; Leung, W. A transcutaneous controlled magnetic microvalve based on iron-powder filled PDMS for implantable drug delivery systems. In *2008 3rd IEEE International Conference on Nano/Micro Engineered and Molecular Systems, Sanya, China, 6–9 January 2008*; IEEE: New York, NY, USA, 2008; Volume 012008, pp. 1160–1163. ISBN 978-1-4244-1907-4.
16. Titano, J.J.; Fischman, A.M.; Cherian, A.; Tully, M.; Stein, L.L.; Jacobs, L.; Rubin, R.A.; Bosley, M.; Citron, S.; Joelson, D.W.; et al. End-hole Versus Microvalve Infusion Catheters in Patients Undergoing Drug-Eluting Microspheres-TACE for Solitary Hepatocellular Carcinoma Tumors: A Retrospective Analysis. *Cardiovasc. Interv. Radiol.* **2019**, *42*, 560–568. [CrossRef] [PubMed]
17. Oh, J.; Kim, G.; Kralick, F.; Noh, H. Design and Fabrication of a PDMS/Parylene Microvalve for the Treatment of Hydrocephalus. *J. Microelectromech. Syst.* **2011**, *20*, 811–818. [CrossRef]
18. Galanopoulos, S.; Chatzidai, N.; Melissinaki, V.; Selimis, A.; Schizas, C.; Farsari, M.; Karalekas, D. Design, Fabrication and Computational Characterization of a 3D Micro-Valve Built by Multi-Photon Polymerization. *Micromachines* **2014**, *5*, 505–514. [CrossRef]
19. Schizas, C.; Melissinaki, V.; Gaidukeviciute, A.; Reinhardt, C.; Ohrt, C.; Dedoussis, V.; Chichkov, B.N.; Fotakis, C.; Farsari, M.; Karalekas, D. On the design and fabrication by two-photon polymerization of a readily assembled micro-valve. *Int. J. Adv. Manuf. Technol.* **2010**, *48*, 435–441. [CrossRef]
20. Chen, P.-J.; Rodger, D.C.; Humayun, M.S.; Tai, Y.-C. Floating-disk parylene microvalve for self-regulating biomedical flow controls. In *2008 IEEE 21st International Conference on Micro Electro Mechanical Systems, Tucson, AZ, USA, 13–17 January 2008*; IEEE: New York, NY, USA, 2008; Volume 012008, pp. 575–578. ISBN 978-1-4244-1792-6.
21. European Parliament and of the Council. Regulation (EU) 2017/745 of the European Parliament and of the Council of 5 April 2017 on Medical Devices, Amending Directive 2001/83/EC, Regulation (EC) No 178/2002 and Regulation (EC) No 1223/2009 and repealing Council Directives 90/385/EEC and 93/42/EEC. Available online: http://data.europa.eu/eli/reg/2017/745/oj (accessed on 4 August 2021).
22. Lv, J.; Jiang, Y.; Zhang, D.; Zhao, Y.; Sun, X. Characterization on the fatigue performance of a piezoelectric microvalve with a microfabricated silicon valve seat. *J. Micromech. Microeng.* **2014**, *24*, 015013. [CrossRef]
23. Yang, E.-H.; Lee, C.; Mueller, J.; George, T. Leak-Tight Piezoelectric Microvalve for High-Pressure Gas Micropropulsion. *J. Microelectromech. Syst.* **2004**, *13*, 799–807. [CrossRef]
24. Zhang, D.; Lv, J.; Jiang, Y.; Chen, H.; Fu, J. A piezoelectric microvalve with a flexure-hinged driving frame and microfabricated silicon sealing pair. *Mechatronics* **2014**, *24*, 511–518. [CrossRef]
25. Cieślik, M.; Kot, M.; Reczyński, W.; Engvall, K.; Rakowski, W.; Kotarba, A. Parylene coatings on stainless steel 316L surface for medical applications—Mechanical and protective properties. *Mater. Sci. Eng. C Mater. Biol. Appl.* **2012**, *32*, 31–35. [CrossRef]
26. Chen, Z.; Gandhi, U.; Lee, J.; Wagoner, R.H. Variation and consistency of Young's modulus in steel. *J. Mater. Process. Technol.* **2016**, *227*, 227–243. [CrossRef]
27. Harder, T.A.; Yao, T.-J.; He, Q.; Shih, C.-Y.; Tai, Y.-C. Residual Stress in Thin-Film Parylene-C. Technical Digest. MEMS 2002 IEEE International Conference. In Proceedings of the Fifteenth IEEE International Conference on Micro Electro Mechanical Systems (Cat. No.02CH37266), Las Vegas, NV, USA, 24 January 2003; pp. 435–438. [CrossRef]
28. Geanta, V.; Voiculescu, I.; Stefanoiu, R.; Rusu, E.R. Stainless Steels with Biocompatible Properties for Medical Devices. *Key Eng. Mater.* **2013**, *583*, 9–15. [CrossRef]
29. Fortin, J.B.; Lu, T.-M. Deposition Kinetics for Polymerization via the Gorham Route. In *Chemical Vapor Deposition Polymerization: The Growth and Properties of Parylene Thin Films*; Fortin, J.B., Lu, T.-M., Eds.; Springer US: Boston, MA, USA, 2004; pp. 41–55. ISBN 978-1-4757-3901-5.
30. Persson, B.N.J. Relation between interfacial separation and load: A general theory of contact mechanics. *Phys. Rev. Lett.* **2007**, *99*, 125502. [CrossRef] [PubMed]
31. Herz, M.; Horsch, D.; Wachutka, G.; Lueth, T.C.; Richter, M. Design of ideal circular bending actuators for high performance micropumps. *Sens. Actuators A Phys.* **2010**, *163*, 231–239. [CrossRef]
32. Gad-el-Hak, M. *The MEMS Handbook*; CRC Press: Boca Raton, FL, USA, 2002; ISBN 9780849300776.
33. Squires, T.M.; Quake, S.R. Microfluidics: Fluid physics at the nanoliter scale. *Rev. Mod. Phys.* **2005**, *77*, 977–1026. [CrossRef]
34. Bruus, H. *Theoretical Microfluidics*; Oxford University Press: Oxford, UK, 2008.
35. Yang, C.; Persson, B.N.J. Contact mechanics: Contact area and interfacial separation from small contact to full contact. *J. Phys. Condens. Matter* **2008**, *20*, 215214. [CrossRef]
36. Persson, B.N.J. On the Fractal Dimension of Rough Surfaces. *Tribol. Lett.* **2014**, *54*, 99–106. [CrossRef]